Progress in Materials Science 110 (2020) 100634

Contents lists available at ScienceDirect

Progress in Materials Science

journal homepage: www.elsevier.com/locate/pmatsci

The materials science of skin: Analysis, characterization, and modeling

Andrei Pissarenko[a], Marc A. Meyers[a,b,c,*]

[a] Mechanical and Aerospace Engineering Department, University of California, San Diego, USA
[b] Materials Science and Engineering Program, University of California, San Diego, USA
[c] Nanoengineering Department, University of California, San Diego, USA

ARTICLE INFO

Keywords:
Skin
Dermis
Collagen
Constitutive models
Synthetic skin

ABSTRACT

Skin is the outermost layer of the body and acts as a primary protective barrier against external agents such as heat, light, infection, and injury. Additionally, skin regulates the temperature of the body and the exchange of fluids. Skin contains a vast network of nerves, glands, and vessels that enable sensing of heat, touch, pressure and pain, and is also a crucial interface that regulates our body temperature and stores water and lipids to maintain a healthy metabolism. In order to fulfill such a broad range of functions throughout life, skin must be able to withstand and recover from significant deformation as well as mitigate tear propagation that can occur during growth, movement, and injuries affecting its integrity. Hence, characterizing the mechanical behavior of skin and understanding the underlying mechanisms of deformation at different spatial scales is essential in a large spectrum of applications such as surgery, cosmetics, forensics, biomimetics and engineering of protective gear or artificial grafts, among others.

The present review draws a comprehensive list of experimental techniques that have been developed over the years to test skin's nonlinear elastic, viscoelastic, and dissipative properties. To identify parameters affecting its behavior, a significant number of models have been developed, some of which are detailed here; they range from macroscopic constitutive laws to structurally-based formulations, involving nonlinear, dynamic, or damage-inducing processes. The principal structural elements within the dermis, and especially the arrangement and orientation of the collagen fibrils and fibers, are presented; their incorporation into the constitutive models is discussed. Future challenges and perspectives in implementing more accurate structural models are highlighted. Major efforts at developing and using synthetic skin are described.

1. Introduction

1.1. Functions and structure of skin

For most vertebrates, skin is the outermost layer of the body and acts as a first protective barrier against external agents such as heat, light, infection, and injury. It is also an important interface with our environment, hosting a myriad of sensors, glands, channels, and pores that enables organisms to feel touch, heat, pain, regulate their body temperature and hygrometry [1].

Its structure can be decomposed into three main regions, and it described by the schematic in Fig. 1.1. The epidermis (50 μm–150 μm in thickness [2-4] for humans) is the external layer of the skin, and mainly fulfills the function of a barrier and

* Corresponding author.
E-mail address: mameyers@ucsd.edu (M.A. Meyers).

https://doi.org/10.1016/j.pmatsci.2019.100634
Received 24 May 2019; Received in revised form 18 October 2019; Accepted 9 December 2019
Available online 16 December 2019

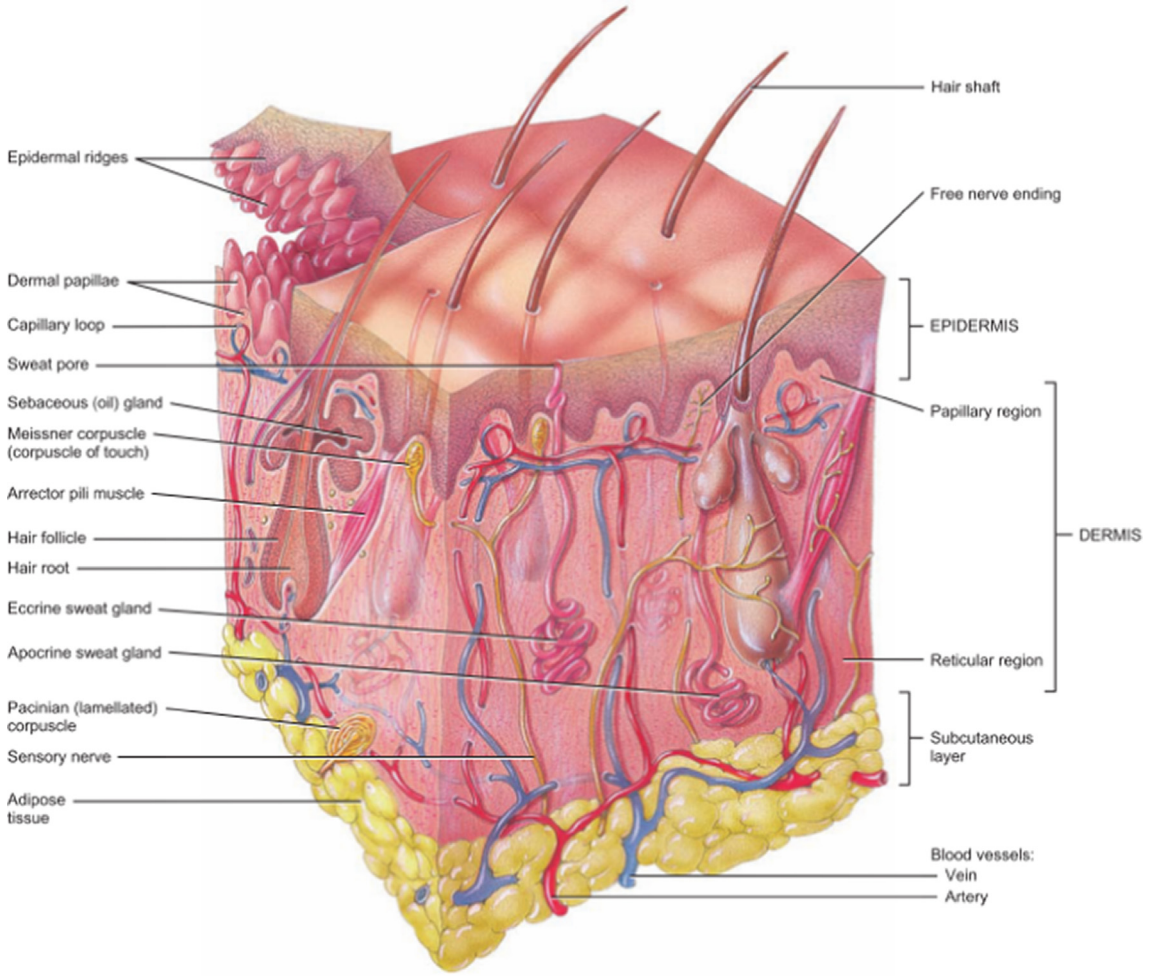

Fig. 1.1. Rendering of the cross-section of mammal skin, showing the diversity of functional elements and structures present in the different layers. Dimensions and density vary among species, individuals, and genders. Note that proportions between different components is not maintained for the sake of clarity. Reprinted from [1].

exchange interface with the exterior [5]. Constant renewal and growth occurs in its sublayers where stem cells in the inner stratum basale differentiate into keratinocytes, which then migrate outwards and eventually decay as corneocytes, forming the stratum corneum, a tough keratinized layer [1,6]. The dermis (150 μm–4 mm in thickness for humans [7,8]) supports the epidermis by providing it with nutrients and structural support via the papillary dermis, where wavy ridges facilitate exchanges. The reticular dermis comprises a variety of sensors, glands, and vessels, and accounts for most of the skin's mechanical properties in tension via a layered and dense arrangement of wavy collagen fibers (~60–80% of dry tissue weight), transverse straight elastin fibers (~1–4% of dry tissue weight), all embedded in a proteoglycan matrix commonly referred to as the ground substance [7-9]. The hypodermis (or subcutaneous layer) is the innermost layer of skin and is mostly composed of adipose tissue, in which adipocytes form clumps called lobules, surrounded by a fibrocollagenous network. Its main functions are to provide thermal insulation, store energy, and absorb shocks [7,8]. Its loose connective tissue structure also enables it to minimize friction with neighboring muscle tissue. Its thickness varies greatly depending on the region of the body and the subject.

Thus, skin can be considered a layered composite material [10], where, from a mechanical viewpoint, each layer fulfills a certain function: the hard keratinized surface of the epidermis enhances toughness, the dermis provides load-bearing [9] properties, the hypodermis provides shock absorption. In the case of tensile behavior, the dermis is the main contributing layer, and understanding the structural arrangement of its constitutive elements is a key factor towards describing the response of skin. Fig. 1.2 shows the different structural levels of collagen fibers, exemplified here for rabbit skin. Starting with polypeptide chains formed in a triple-helix arrangement, tropocollagen molecules have a length of ~300 nm and a diameter of ~1.5 nm. These macromolecules arrange themselves into collagen fibrils, characterized by a d-period of 67 nm, which is the defining structure of collagen. The fibrils have diameters of ~50–300 nm and are organized into fibers with parallel fibrils, forming bundles with diameters ranging ~2–7 μm. At this organizational level the complexity of the arrangement is less well understood. Many models of skin tend to neglect out-of-plane components of the collagen network, suggesting a layered disposition, as in the work on rabbit skin of Sherman et al. [11]. On the

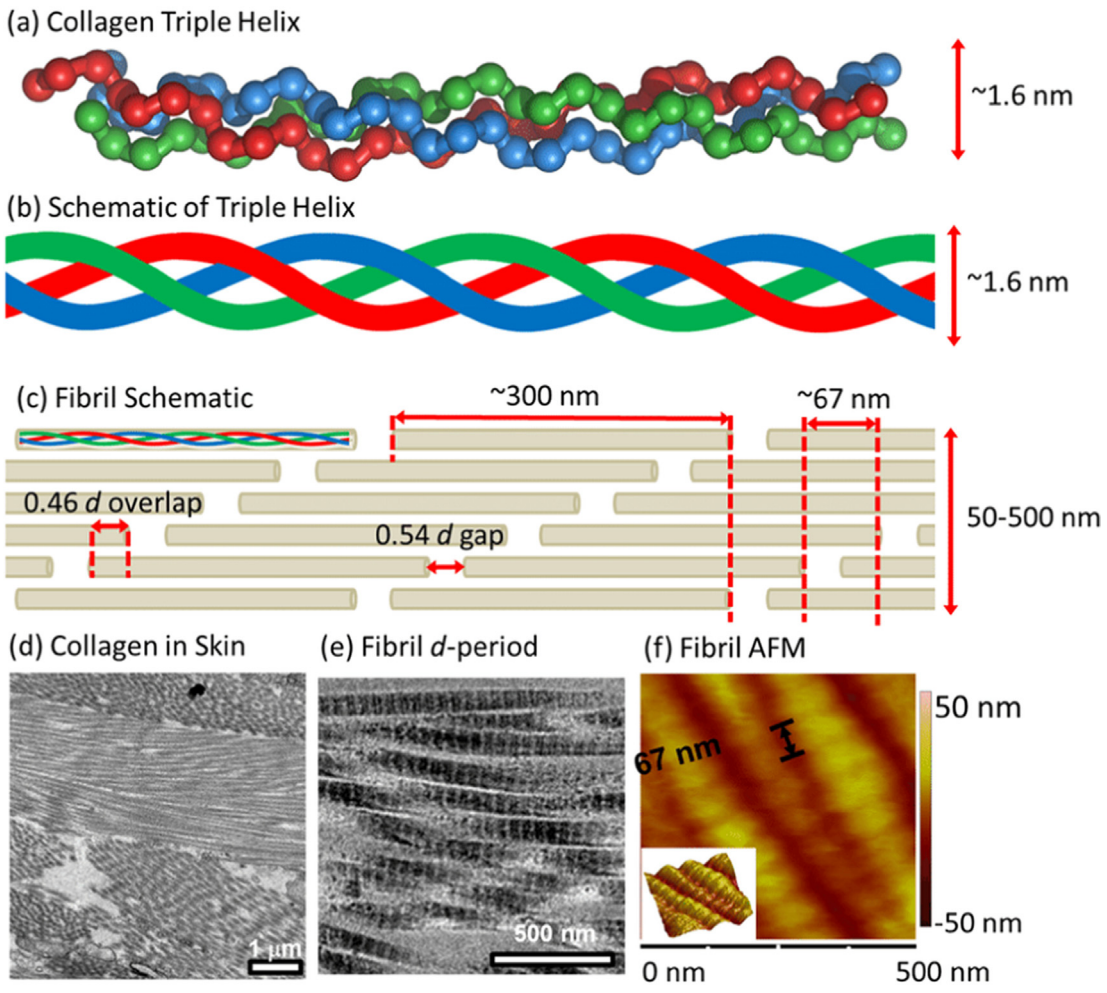

Fig. 1.2. The full hierarchy of collagen in the dermis. (a,b) Tropocollagen chains form right handed triple helices. (c) Tropocollagen molecules form a quarter-staggered arrangement, with a characteristic d-period of 67 nm. This footprint of collagen fibrils makes them easily recognizable under Atomic Force Microscopy (AFM) (f) or Transmission Electron Microscopy (TEM) (e). (d) TEM of rabbit skin also shows collagen fibrils bundled together into fibers, with a circular/elliptical cross section and a high fibril density. Reprinted from [108].

other hand, transmission electron microscopy imaging of pig skin (Pissarenko et al. [12]) shows a three-dimensional organization of the collagen lattice, with preferred orientations (Fig. 1.3). Similarly, Jor et al. [13] reported that collagen fibers in pig skin form a dense three-dimensional network with average angles of ± 45° with the surface of the skin (Fig. 1.4). It is also likely that arrangements vary from species to species.

In Fig. 1.5, the structural arrangement of collagen fibers and collagen fibril size distributions in skin is compared with two other collagenous tissues: tendon and pelican pouch. On one hand, fibers in tendon form larger scale fascicles, and are highly aligned along the principal axis of the tissue, as the scanning electron micrograph Fig. 1.5a and the optical micrograph Fig. 1.5b show [14,15]. Fibril diameter, as seen in the transmission electron micrograph of the cross-section of a human tendon Fig. 1.5c [16], follows a bimodal distribution with an even repartition. The waviness and interweaving of collagen fibers in the dermis of pig skin is illustrated again in Fig. 1.5d–e. The cross-section of a collagen fiber in the dermis shows a more consistent distribution of collagen fibril diameters [12]. On the other hand, pelican pouch is an example of a soft tissue with a high level of collagen fiber curvature, as presented Fig. 1.5g–i, which considerably enhances the extensibility of the material, up to 400% (unpublished data). The bimodal distribution parameters of collagen fibril diameters for five types of tendon in humans [16], pig skin [12], and pelican pouch are reported in Table 1.1. The bimodal fit corresponds to the following distribution function:

$$f(x) = \frac{A_S}{\sqrt{2\pi\sigma_S^2}}\exp\left(-\frac{(x-\mu_S)^2}{2\sigma_S^2}\right) + \frac{A_L}{\sqrt{2\pi\sigma_L^2}}\exp\left(-\frac{(x-\mu_L)^2}{2\sigma_L^2}\right) \tag{1.1}$$

With parameters A_S and A_L, the peaks of the small and larger diameter distributions, respectively, μ_S and μ_L the corresponding means, and σ_S and σ_L the standard deviations. The bimodal ratio $R = A_L/A_S$ can also be introduced. It gives information on the

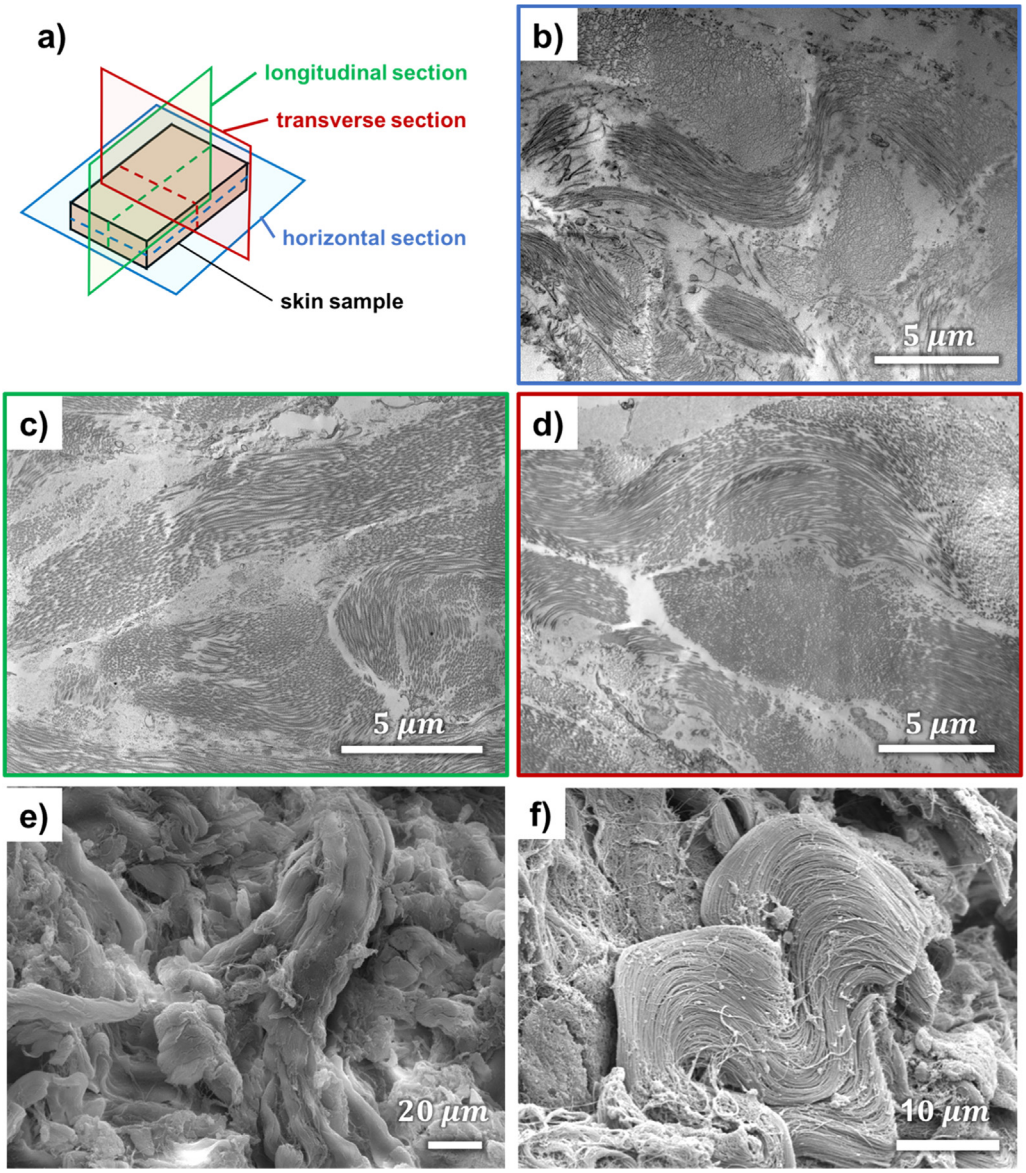

Fig. 1.3. Visualization of the three-dimensional arrangement of collagen fibers in the dermis of pig skin. (a) Schematic representation of the different observation planes for Transmission Electron Microscopy (TEM). TEM of slices in the (b) horizontal, (c) longitudinal, and (d) transverse planes showing a complex three-dimensional arrangement of collagen fibers, formed by bundles of fibrils. (e-f) Scanning Electron Micrographs (SEM) of pig skin samples, showing crimped collagen fibers aligned in various directions.

repartition between small and larger fibrils. For tendons, it varies between 0.82 and 3.34, hence the proportion is either even or in favor of larger diameters, which can go up to 125 nm for the mean value. Collagen fibrils in the pelican pouch have a significantly larger diameter, with 102 nm for μ_S and 171 nm for μ_L. Mean values μ_S and μ_L are often 50–70 nm apart and vary considerably across tissues. Skin falls in the middle, however large diameters are much rarer (16%) than smaller fibrils, with also narrower standard deviations, indicating more consistency in fibril size, as shown Fig. 1.5f. Skin is therefore a tissue with relatively curved collagen fibers, which contribute to its nonlinear elasticity, formed by bundles of collagen fibrils with a quite consistent diameter.

The organization of elastin in the dermis of skin is reported more rarely, mainly because of its low volume fraction in skin. It appears as straight fibrils, transversely connecting collagen fibers [17,18], as seen in the confocal image of pig skin, on Fig. 1.6. As pointed out by Pittet et al. [18], the volume fraction of elastin decreases with age. Elastin fibers in older tissues become thicker and more fragmented, and show a greater affinity for calcium, affecting their ability to withstand large deformations [1].

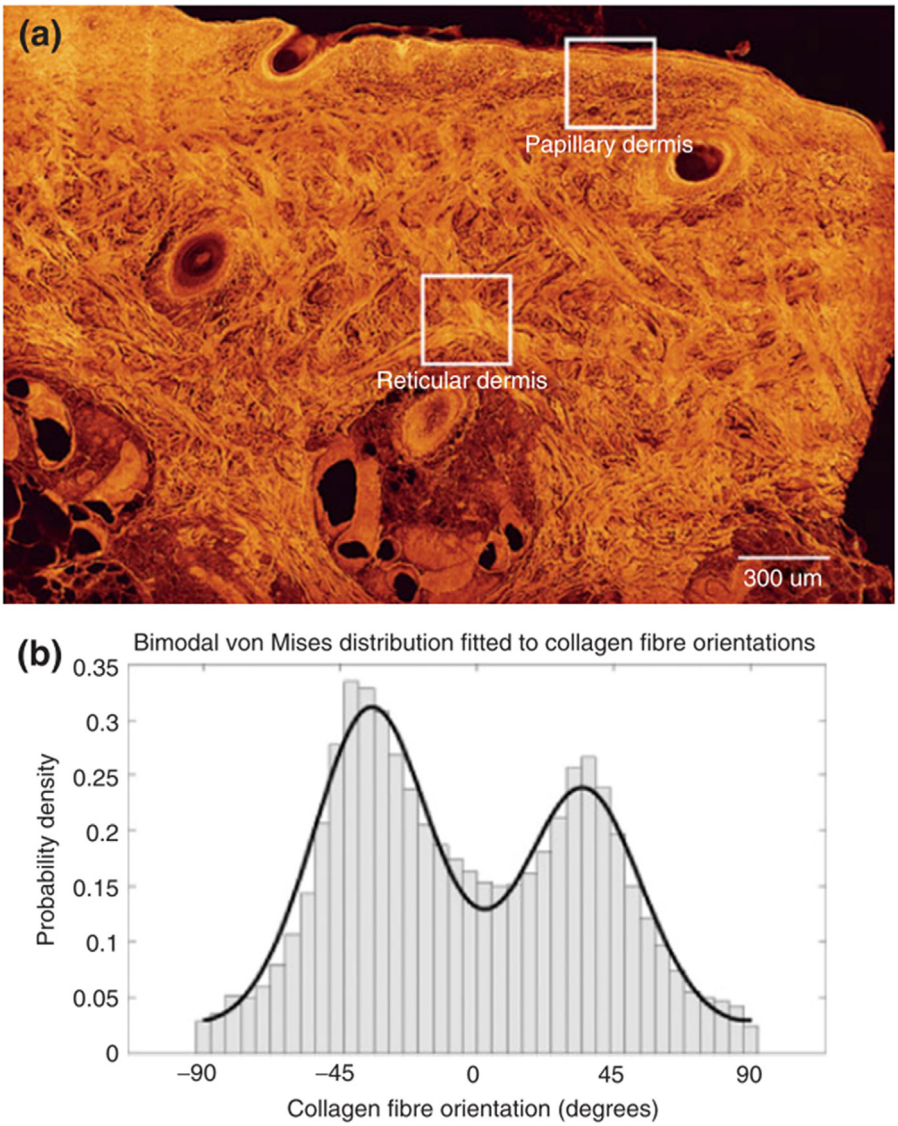

Fig. 1.4. (a) Cross-sectional view of a pig skin sample using Confocal Microscopy, (b) A bi-modal analysis shows that the collagenous network in this plane seems to be organized in a lattice arrangement, with preferred angles ± 45°. From Jor et al. [13].

1.2. On the relevance of studying skin

Throughout life, skin must be able to withstand significant deformations, shocks, and mitigate propagation of tears that can occur during growth, movement, or injuries. Therefore, understanding the mechanisms of deformation at different spatial levels can be essential in areas ranging from cosmetics, surgery, forensics, armor design, and to biomimetic skin grafts, where our expanding knowledge can be extensively applied to improve current methods.

A classic example is the Pfannenstiel-Kerr incision [19], a C-section surgical procedure, performed in the transverse direction (perpendicular to the spine). It results in a reduction of the incised area and minimizes bleeding, and consequently in a decrease of the mortality rate of both mothers and their newborns, as well as in reduced scar tissue formation. Such improvements were partially made possible by the earlier discovery of Langer lines. First observed by anatomist and surgeon Guillaume Dupuytren in 1831, they were further characterized by Dr. Karl Langer in 1861 [11,20,21]. Both observed that by stabbing a cadaver using a stylet with circular cross-section in different locations of the body, the wound would stretch in one preferred direction and become elliptical, showing for the first time pre-existing axes of tension, and therefore defining skin's anisotropy and ability to adapt to loads; thus, the Langer lines. Said lines were later mapped for the human body by Cox [22] (see Fig. 1.7), but can also be encountered in other species [23,24].

The reduction of scar tissue formation is a vastly studied topic in plastic surgery and has known great improvements over recent years, thanks to an accrued knowledge of skin's mechanobiology [25]. New techniques involve stress-relieving implants or bandages

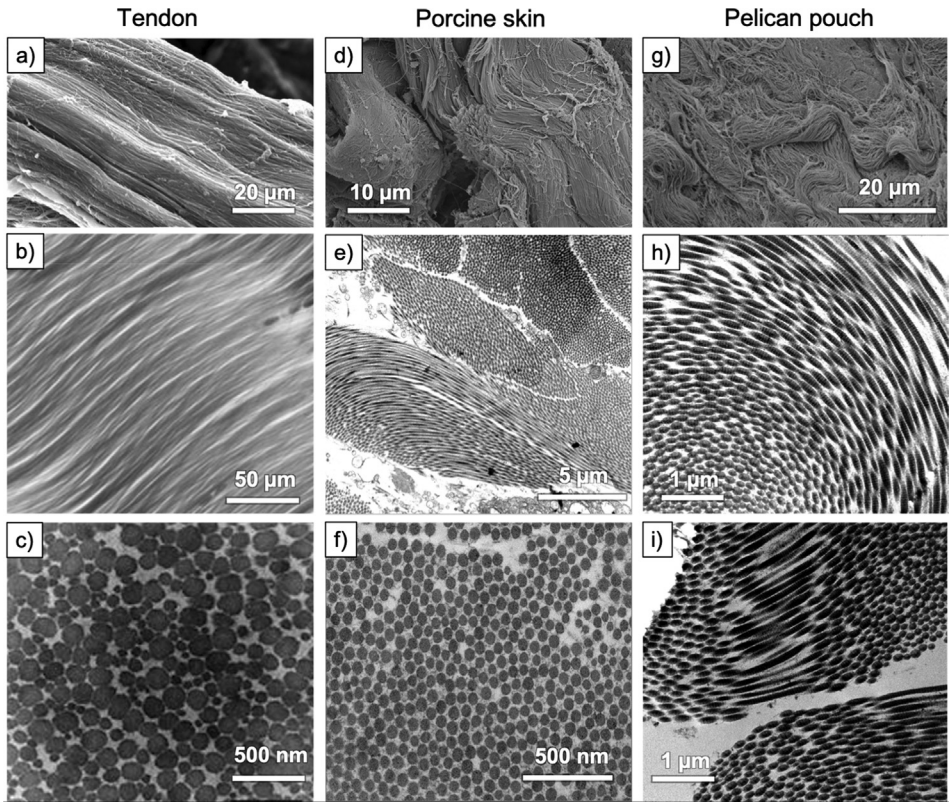

Fig. 1.5. (a) Scanning electron micrograph (SEM) of human tendon [14] and (b) optical micrograph [15] of rat tendon in the longitudinal direction, showing a consistent alignment of fibrils. (c) Transmission electron micrograph (TEM) of a cross-section of a collagen fiber from human patellar tendon, showing a significant variation of collagen fibril diameter [16]. (d) SEM and (e) TEM of porcine dermis in the longitudinal section, showing highly curved collagen fibers going in and out of plane. (f) TEM of a cross-section of a collagen fiber in the dermis. The fibril diameter distribution is more consistent [12]. (g) SEM and (h) TEM of the pelican pouch skin in the longitudinal direction and (i) in the transverse direction. Collagen fibers show a much higher degree of curvature, as well as a bimodal distribution of fibril diameters (unpublished data).

Table 1.1
Distribution parameters of collagen fibril diameters reported for human tendon (patellar, quadriceps, semitendinosus, ITB, ACL) [16], pig dermis [12], and pelican pouch (unpublished data). A bimodal distribution is assumed. Parameter R corresponds to the bimodal ratio, i.e. the ratio between the amplitudes of the large diameter peak A_L and the smaller diameter peak A_S.

Tissue		μ_1 (nm)	σ_1 (nm)	μ_2 (nm)	σ_2 (nm)	R
Tendon	Patellar	52.25	17.64	110.6	32.77	0.82
	Quadriceps	58.73	17.31	114.2	18.45	0.77
	Semitendinosus	75.16	34.44	124.6	23.01	1.32
	ITB	59.74	7.97	70.2	21.84	1.22
	ACL	61.08	13.2	66.94	25.88	0.87
Pig dermis		77.11	8.31	115.5	6.88	0.16
Pelican pouch		102.07	22.28	170.62	23.18	0.46

that condition the mechanical environment of the healing region [26-28]; some of these solutions are presented in Fig. 1.8. Recently, synthetic skin grafts have also been a flourishing area of research [29-32], where significant progress can be correlated with advances in tissue engineering and additive manufacturing.

Wearable devices are also a developing industry, aiming to improve self-monitoring of health indicators, varying from sports activities to the auto-regulation of chronic diseases [33,34]. Such advances have required the development of models of skin mechanics, either based on phenomenological observations or physical descriptions of the tissue. An important step of this process is characterizing the deformation mechanisms at different length scales such as macroscopic tensile tests, or microscopic observations. First, the present review draws a non-exhaustive summary of the experimental techniques that have been implemented to characterize the behavior of skin under different types of loading, at a macroscopic scale. Tensile properties and testing (direct and indirect) are mainly emphasized because it is the most important and frequent type of load that skin experiences. Compressive loading of skin is less frequently studied, and is mainly relevant to cases following impact or blast injury. Second, associated models

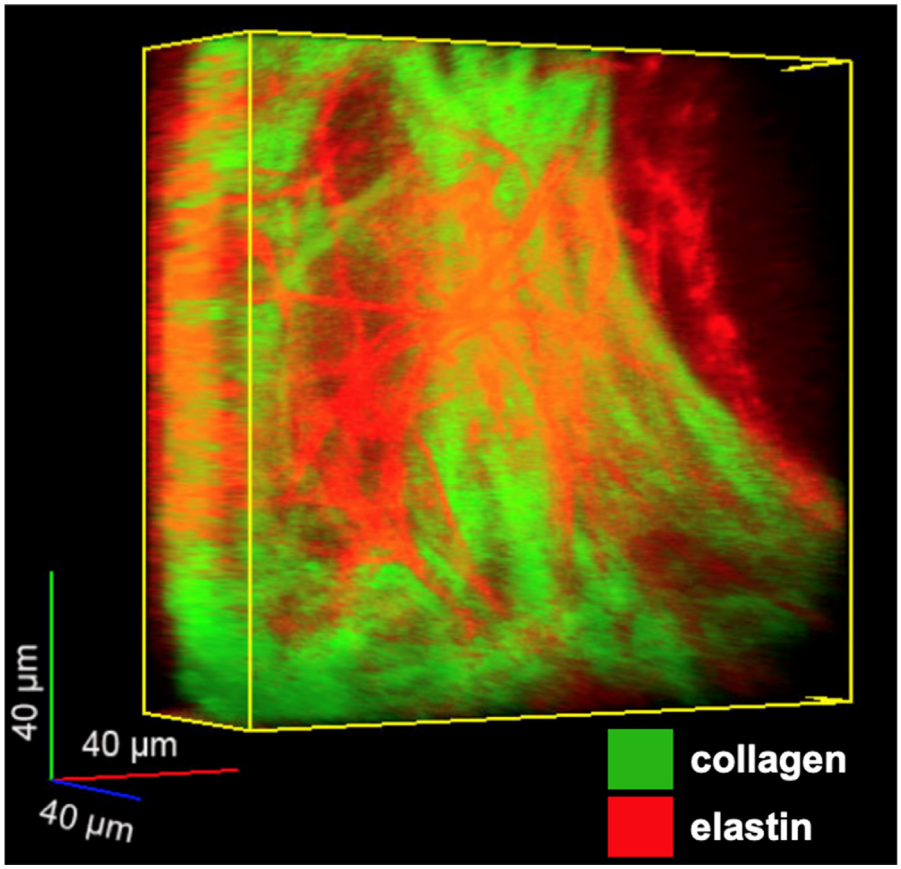

Fig. 1.6. Multiphoton tomography of young human skin, showing collagen fibers in fluorescent green, and elastin in red. Elastin fibers are straight and thin, and interconnect collagen fibers transversely. From Pittet et al. [18]. (For interpretation of the references to color in this figure legend, the reader is referred to the web version of this article.)

that have been developed based on these observations are discussed, outlining their strengths and limitations. A better understanding of the deformation mechanisms can be gained by taking a closer look at the microstructure of skin. Although a valuable amount of work has been done on the properties of the epidermis, and more particularly the *stratum corneum*, our review is limited to the microstructure of the dermis, considered to account mostly for skin's mechanical behavior, especially at large strains. The current knowledge of the hierarchical arrangement of the forming components of skin constitutes a basis for physical models of skin mechanics, which use nano and microstructural features to describe the macroscale behavior.

2. Experimental characterization of skin mechanics

Skin is an anisotropic, nonlinear, viscoelastic, tissue and subject-specific material, which consequently yields highly variable experimental results. Rodrigues [35] reported that measured values of the Young's modulus of human skin with *in vivo* tests can differ by four orders of magnitude. One main cause of variability is the lack of test standardization. Moreover, the Young's modulus is a measure of linear elasticity, which is not appropriate for a nonlinear material like skin. Studies in the literature generally report a local measurement of the slope of a given portion of the stress-strain curve, which we will refer to as tangent modulus in this review.

Methods can vary by sample and setup size, sample attachment or gripping, the region that is tested, or whether the sample is preconditioned. Preconditioning was first introduced by Fung [36] and corresponds to a cyclic load applied at low strains until the tissue response becomes reproducible. This potentially reduces inter-sample variations due to relative orientation or pre-stress. Applied deformations cover continuous stretching, cyclic loading, relaxation, and creep, and are used as methods to characterize skin's nonlinear elasticity, viscoelasticity, and dissipative behavior.

Experimental testing of mammal skin can be categorized into two distinct methods: *in vivo* and *ex vivo* setups, where the sample is either tested directly on the subject, or excised from it prior to testing, respectively. Among tested species we can find mice [37], rats [38,39], rabbits [11,40,41], swine/pigs (for the similarity of their skin with humans) [10,25,42-50], humans [45,51-81], cattle [82], and rhinoceros [83]. For obvious ethical restrictions, non-invasive *in vivo* testing is usually favored, especially for the characterization of human skin, yet *ex vivo* data on humans can also be found in the literature (where skin is excised from cadavers or surgical flaps), and provides more rigorous results in simple kinematics and geometries. These methods are discussed in the following section.

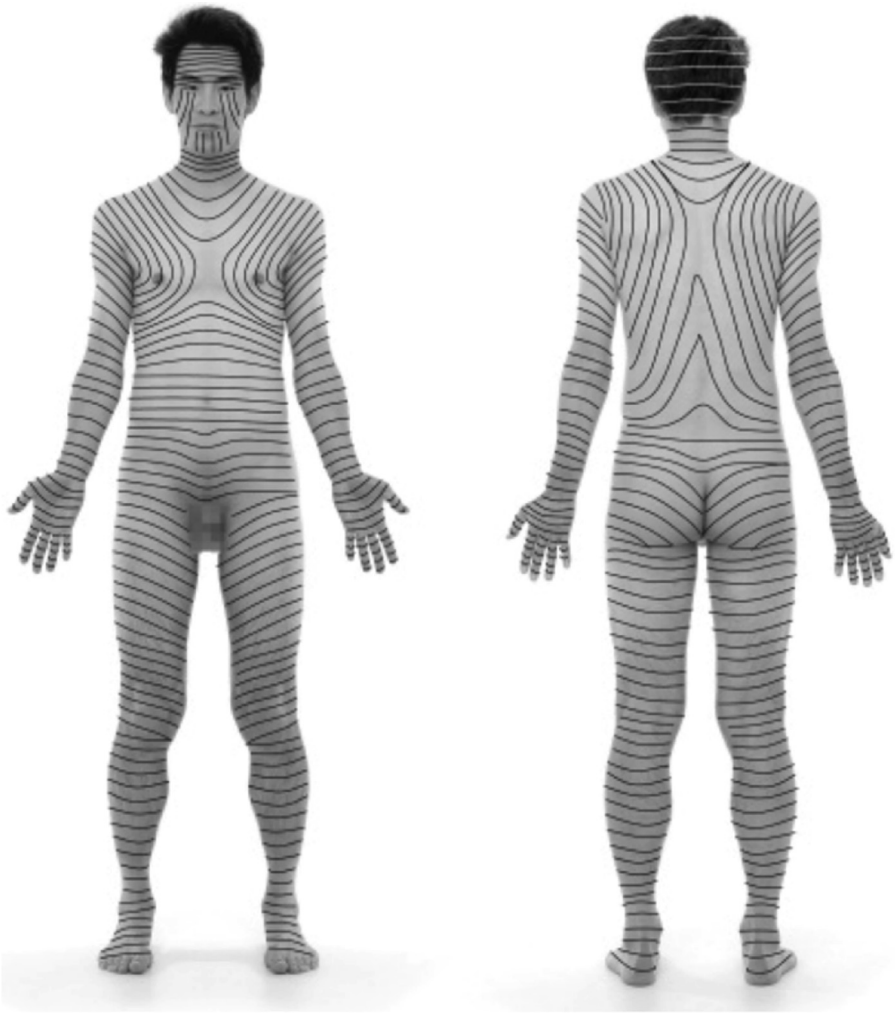

Fig. 1.7. Langer lines indicating the direction of alignment of the collagen fibers. From Meyers and Chen [20].

2.1. In vivo testing of skin

One main advantage of *in vivo* experiments is that they are non-destructive, which ensures repeatability of tests and accessibility of samples with fewer ethical restrictions. Another important aspect is that skin *in vivo* is in its natural configuration, undergoing tensile loads dictated by its environment (along the Langer lines) and interfaces with other organs in the body. However, this is limited by the fact that damage and failure cannot be observed, which reduces the span of the obtained stress-strain curves. Also, sample accessibility is restricted, such that only methods contacting skin superficially can be applied.

2.1.1. Extensometry

Classically, the principle of extensometry is to apply a relative displacement (either positive or negative) between two or more pads that are fixed on the surface of the tested material and to measure the resulting force (Fig. 2.1a). Mechanical properties of skin *in vivo* have been tested in uniaxial [84-86] and multiaxial geometry (Fig. 2.1b) [58]. Improvements of such systems also include the addition of circumferential shield guards [45], which minimize the effects of peripheral forces from the skin surrounding the tested region, or coupling with optical [58] or ultrasonic [87] tools to increase the accuracy of the measured deformation.

Tests can be run at low strain rates, and the obtained force-displacement curves can be used to compare variations due to changes in tested location or orientation. Because gauge dimensions in the *in vivo* configuration are difficult to estimate, quantitative assessment of the mechanical properties is often limited to linear or areal parameters [45,84], unless image-based strain calculation methods [58], or numerical simulations [45] are implemented.

Another extension of this method is the recent use of triaxial force-sensitive micro-robots. Flynn et al. [65,72] developed a protocol where a robotic probe is glued to the skin and applies a set of pre-defined deformations; a three-dimensional arrangement of force transducers allows for measurement of the reaction force. The tested region is isolated using a guard ring. They used this method to apply a range of in-plane and out-of-plane cyclic displacements in order to observe orientation-related variations in

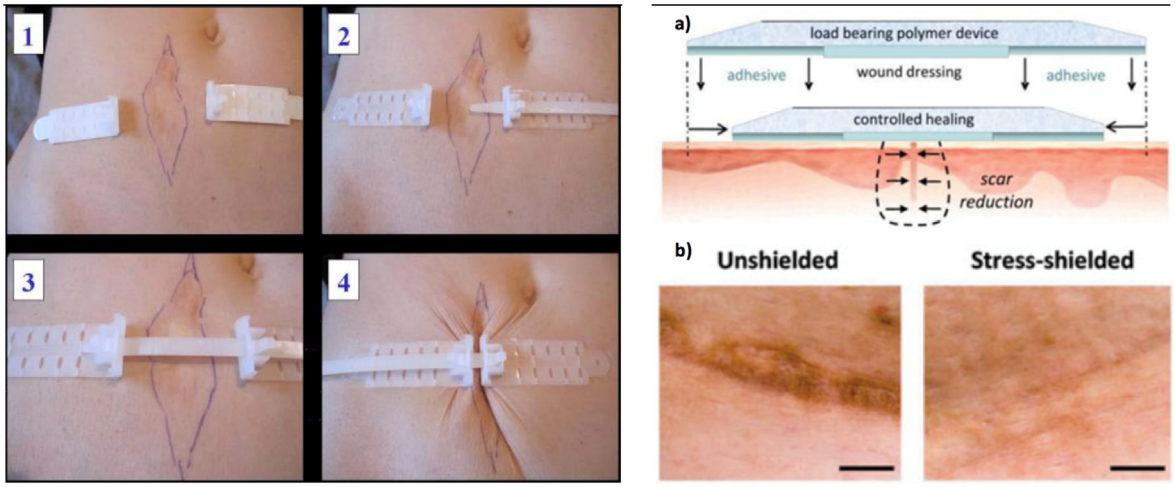

Fig. 1.8. Examples of recent technologies to minimize scar tissue formation by locally relieving stress in the healing region. Left: TopClosure device (http://www.topclosure.com), where the healing scar is transversely closed by a pair of glued (or stapled) plates tied by a strap. Right: (a) Schematic illustration of the Stress-shielding device developed by G. Gurtner et al. [27,28]. The bandage-like taunt is placed after removal of sutures and applies a uniform compression on the wound. (b) Comparison of unshielded and shielded wound healing on swine skin; the scar is much less apparent in the stress-shielded cut.

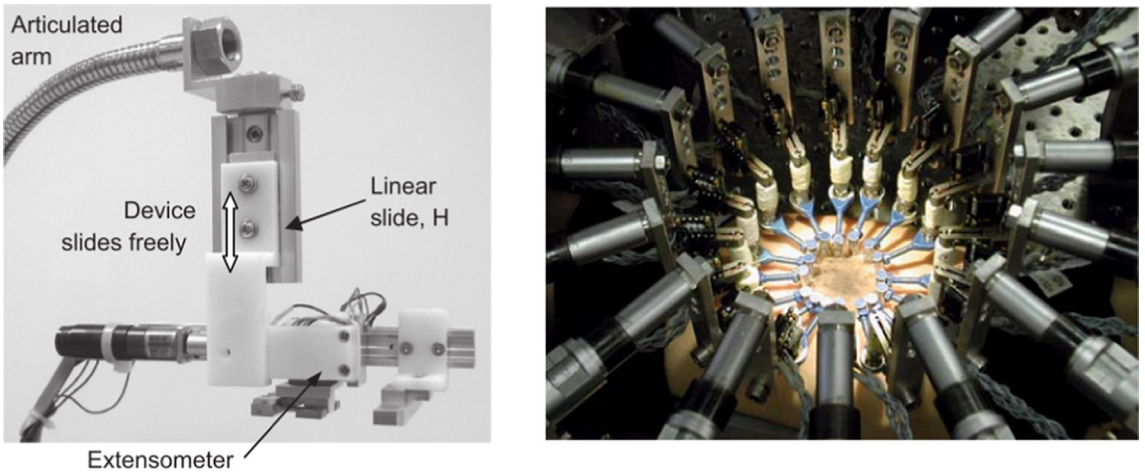

Fig. 2.1. Left: Uniaxial shield pad extensometer developed by Lim et al. [45]. Right: Multiaxial extensometer setup used by Kvistedal et al. [58].

dissipated viscoelastic energy, for various locations of the forearm [65], and the face [72]. Out-of-plane deformations can be also assimilated to an extension of the indentation method (see Section 2.1.4).

2.1.2. Torsion

Typical torsion (or shear inducing) devices consist of a friction head placed in contact with the surface of the skin and set in rotation by an actuator [57,88-90]. An example of a commercially available device, the Frictiometer®, is presented Fig. 2.2a. A normal pressure and/or an adhesive can be applied to optimize friction, and a guard ring can be used to isolate the tested region [53,60]. By applying a certain torque (or angular displacement), the skin is set in rotation in the area between the friction head (disk) and the external ring (if present). The torque-angular displacement curve thus obtained can be used to qualitatively observe the skin's viscoelastic response and compare age, gender, location, and moisture-related variations in skin's elasticity. However, because torsion tests are not conducted along one specific alignment, they cannot be used to assess anisotropy. Quantitative estimation of an elastic modulus, E, can be done using equations that have been derived for unshielded mechanical tests by Vlasblom [91] and later applied by Sanders [89]:

$$E = \frac{2M(1+\nu)}{4eR_1^2\theta} \tag{2.1}$$

and by Leveque et al. for shielded tests [60]:

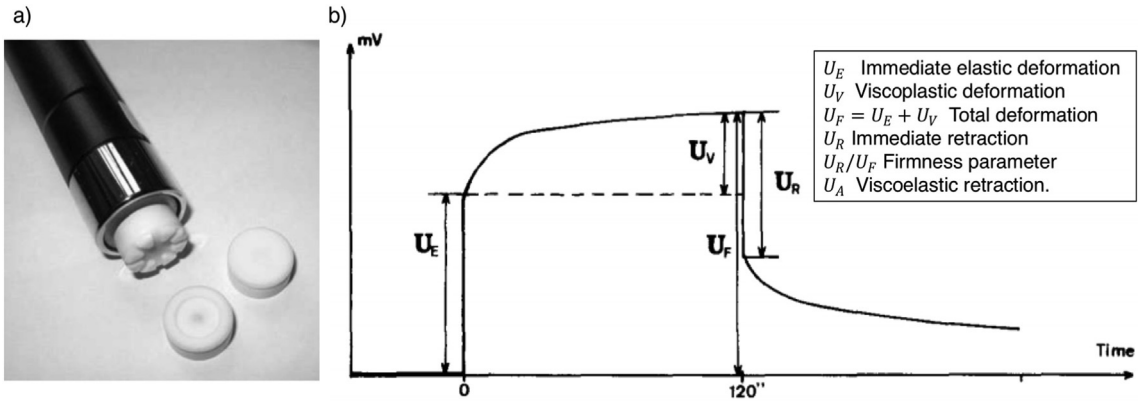

Fig. 2.2. (a) Photograph of the Frictiometer® FR 700 (Courage-Khazaka, Köln, Germany), a clinically used torsion probe. (b) Typical deformation curve of a skin sample after torque application (t = 0) and torque removal (t = 120 s) with a shielded torsion device, developed by Leveque et al. [60]. The angular displacement is linearly proportional to the measured voltage.

$$E = \frac{M}{2\pi \cdot 0.4 e R_1 R_2 \theta} \tag{2.2}$$

where M is the applied moment, e the estimated skin thickness, R_1 the disk radius, R_2 the guard ring radius (for shielded tests), and θ the angular rotation at R_1. In Leveque's equation, the Poisson ratio ν is estimated to be equal to 0.25. It is important to note that the above equations correspond to linear approximations of the mechanical response of skin and therefore do not fully describe its nonlinear elastic behavior.

The torsion method is a rather easy and quick technique that is not too restrictive in terms of accessibility, and has, as a result, been widely used in the context of clinical dermatology [92]. Direct measurements of the angular rotation over time (for an imposed value of the applied torque), i.e. creep tests, tend to be preferred. Specific viscoelastic parameters are used to monitor skin's response, and were initially introduced by Boyer et al. [63]:

– U_E the immediate elastic deformation,
– U_V the viscoplastic deformation,
– $U_F = U_E + U_V$ the total deformation,
– U_R the immediate retraction,
– U_R/U_F the firmness parameter,
– U_A the viscoelastic retraction.

Fig. 2.2b shows a typical deformation vs. time curve from a torsion test, where the aforementioned parameters are indicated.

2.1.3. Suction

First introduced by by Grahame and Holt in 1969 [93] for experiments *in vivo*, the suction method consists of applying a negative pressure through a cylindrical or hemispherical cup mounted on the tested region, resulting in an upwards deformation of a dome of skin. The height of the raised dome is compared with the suction pressure, and a stress-strain curve can be obtained using Tregear's equation [94] for deforming hemispherical domes:

$$\sigma = \frac{pR^2}{4xe}\left(1 + \frac{x^2}{R^2}\right) \tag{2.3}$$

$$\epsilon = \frac{2x^2}{3R^2\left(1 + \frac{2x^2}{R^2}\right)} \tag{2.4}$$

where σ and ϵ are respectively the engineering stress and the engineering strain, p is the applied pressure, R the radius of the suction cup, e the estimated skin thickness and x the height of the deformed dome. The modulus of elasticity is then obtained by isolating the slope of a portion of the stress-strain curve [93]. The aperture of the suction cup has a non-negligible influence on the calculated parameters, as with a smaller diameter, only more superficial layers of the skin will deform [5].

In the same way as torsion tests, suction tests are simple to implement, and a broad range of regions can be tested. Clinical studies have shown that suction tests provide reliable indicators for skin aging [77,92,93], which explains its continuous development and use, such as the Cutometer® (Courage-Khazaka, Köln, Germany), or the DermaLab® (Cortex Technology, Hadsund, Denmark), presented in Fig. 2.3. It is currently the most used non-invasive *in vivo* experimental technique in clinical dermatology [77,92,95-97], and, as in torsion tests, the parameters U_E, U_V, U_F, U_R, U_R/U_F from creep tests are favored to assess age, gender, or treatment-related changes.

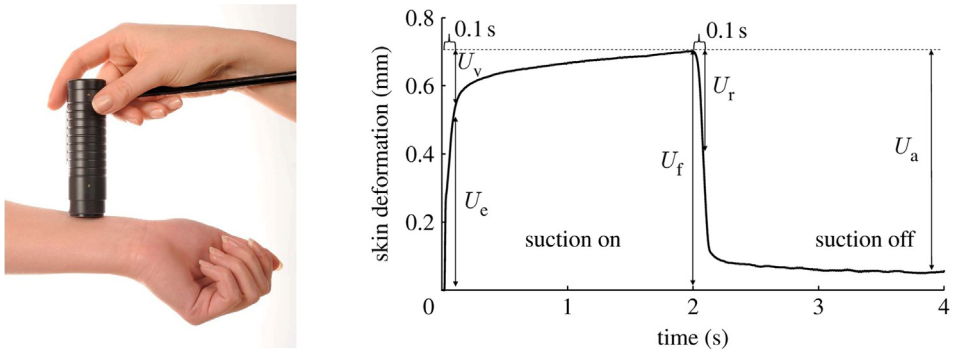

Fig. 2.3. Left: Photograph of the Cutometer®, a clinically used suction device (http://www.courage-khazaka.de/index.php/en/products/scientific/140-cutometer). Right: Typical deformation curve from a suction test, obtained with the Cutometer® and reported by Gerhardt et al. [103]. Viscoelastic parameters are indicated on the graph.

2.1.4. Indentation method

It can be considered that indentation is historically the first method to directly test dermal elasticity, with Schade's adaptation of the eye tonometer for skin, in 1912 [98]. It was subsequently refined in other studies [99,100]. Current setups are also adaptations of mechanical nanoindenters which are being widely used in the characterization of biological materials (see Fig. 2.4).

In this technique, a rigid indenter applies a controlled displacement δ at a given location on the subject's skin, and the normal force F_N is recorded. Controlling the applied force and recording the penetration depth is also feasible. From the obtained data, the indentation modulus E*, can be determined [52]:

$$E^* = \frac{\sqrt{\pi/A}}{2}\frac{dF_N}{d\delta}\bigg|_{F_N=F_{max}} \tag{2.5}$$

where A is the projected contact area and F_{max} is the force at unloading. Elasticity parameters can be found via the following approximation:

$$E_{skin} = E^*(1-\nu_{skin}^2) \tag{2.6}$$

where E_{skin} is the uniaxial elasticity modulus of skin, and ν_{skin} the Poisson ratio.

The indentation method is non-invasive and does not require any shielding of the tested area. However, depending on the penetration depth, the indenter size and geometry, other regions under the skin can affect the results [52,70]. Anisotropy of the tissue cannot be resolved with such techniques. Moreover, stress-strain curves are difficult to obtain because the geometry of the deforming region is hard to define. It was shown that pre-stress in the tissue affects the measured response as well [101].

Other less common *in vivo* experimental methods for skin testing include vibration/friction [62,102,103], and ballistometric [104,105] tests, to mention a few.

While *in vivo* methods have limitations (sample accessibility, limited deformation), they can also be useful non-invasive and non-destructive tools in a clinical context to monitor changes in mechanical properties of a patient's skin due to causes such as aging, wound healing, or radiation therapy. The obtained results and reported parameters vary widely, mainly due to lack of test standardization [35,92]. Depending on the parameters of the experimental setup, e.g. suction cup diameter, or indenter shape and diameter, different layers of the skin and sometimes subcutaneous organs contribute to the deformation, which complicates obtaining

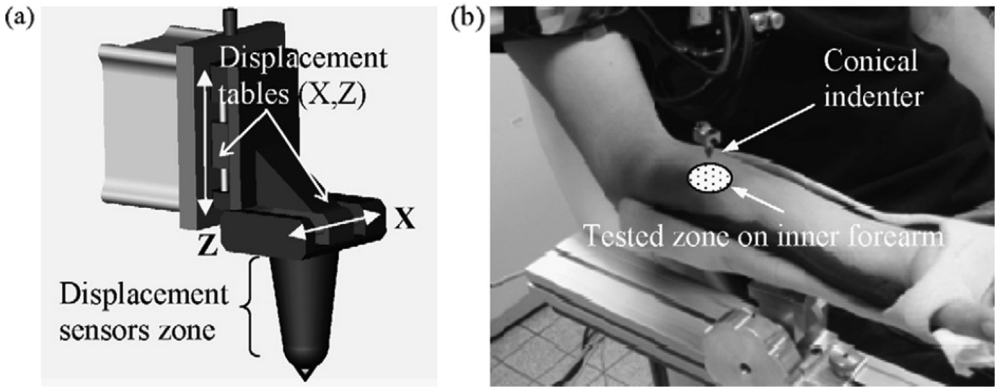

Fig. 2.4. (a) Schematic representation of the indentation device developed by Pailler-Mattei et al. [52]. (b) Positioning of the system of a subject's arm.

consistent experimental results. The high inter-subject variability accentuates this problem.

2.2. Ex vivo testing of skin

Although presenting some ethical restrictions, excising skin from a subject, either *post-mortem* or after surgery, gives researchers more freedom in terms of experimental techniques. More particularly, standardized mechanical testing methods become feasible, which usually improves the consistency and reliability of results. The deformation range can be extended to larger strains, which enable the characterization of additional mechanical processes such as irreversible deformations, damage, and tissue failure. When applying such techniques, one main obstacle to accurate measurements is commonly related to the fact that at high strains and high strain rates, the layer of fat covering the hypodermis lubricates the interface with the grips and contributes to additional slipping. Thus, specific gripping systems need to be designed to alleviate this problem. These designs are rarely communicated, and their performance is seldom quantified. Due to preexisting tension in skin, samples shrink differently after excision, implying that calculation of strains and stresses need to be addressed carefully when comparing *in vivo* and *ex vivo* results.

Most techniques described for *in vivo* experiments in the previous section have also been applied *ex vivo* (also reported as *in vitro* experiments). For example, Jee and Komvopoulos [106] reported data for the reduced elastic modulus of porcine skin from *in vitro* nano/microindentation methods, with a major emphasis on breed type variations. A more considerable amount of work has been conducted with tensile tests, as described in the following sections.

2.2.1. Uniaxial tensile testing

It is not surprising that uniaxial tensile testing protocols were also implemented for skin, as it is perhaps the most common mechanical test. Uniaxial testing machines are easily accessible, and the skin's anisotropy can be quantified by varying the direction of tension. One of the first reported uniaxial experiments on excised skin was conducted by Ridge et al. in 1966 [107], where deformation along and across the Langer lines of human cadavers was compared, showing skin's anisotropy. Since then, with the development of mechanical testing machines, a very broad range of experimental studies have focused on the influence of sample orientation and location [25,38,41,46,54,56], hydration [40,108], and strain rate [47], to mention some examples. Samples are preferably cut in a dumbbell shape, to maximize stress uniformity in the gauge region. Recently, Yang et al. [40] also performed tensile tests to observe the remarkable tear resistance of skin, using skin samples excised from rabbits (see Fig. 2.5). Unlike most materials, skin mitigates the propagation of a pre-cut crack by blunting.

2.2.2. Biaxial tensile testing

Lanir and Fung [109] described in 1974 a biaxial testing setup, with the purpose of further characterizing the three-dimensional behavior of skin. The setup is shown in Fig. 2.6. In their design, a small rectangular piece of the tissue is connected to a force-distributing platform at each side via a set of stapled silk threads. The displacements are controlled in both directions, and sample deformations are recorded on camera. The setup was used to perform tensile and relaxation tests on rabbit skin, after biaxial

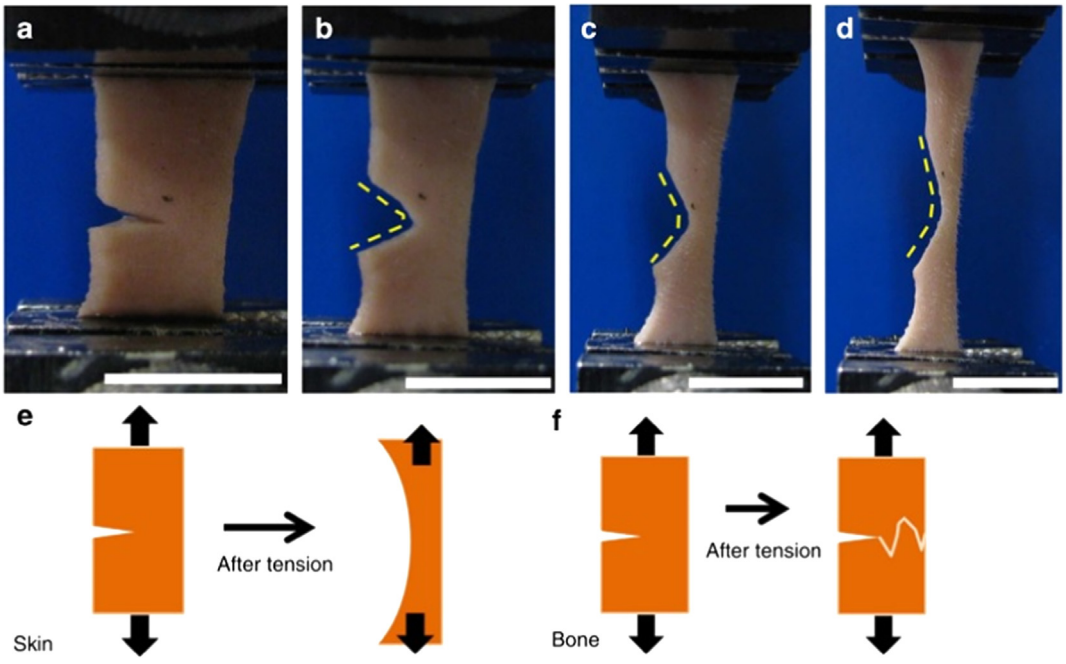

Fig. 2.5. Tear resistance of rabbit skin in comparison to bone materials. From Yang et al. [40].

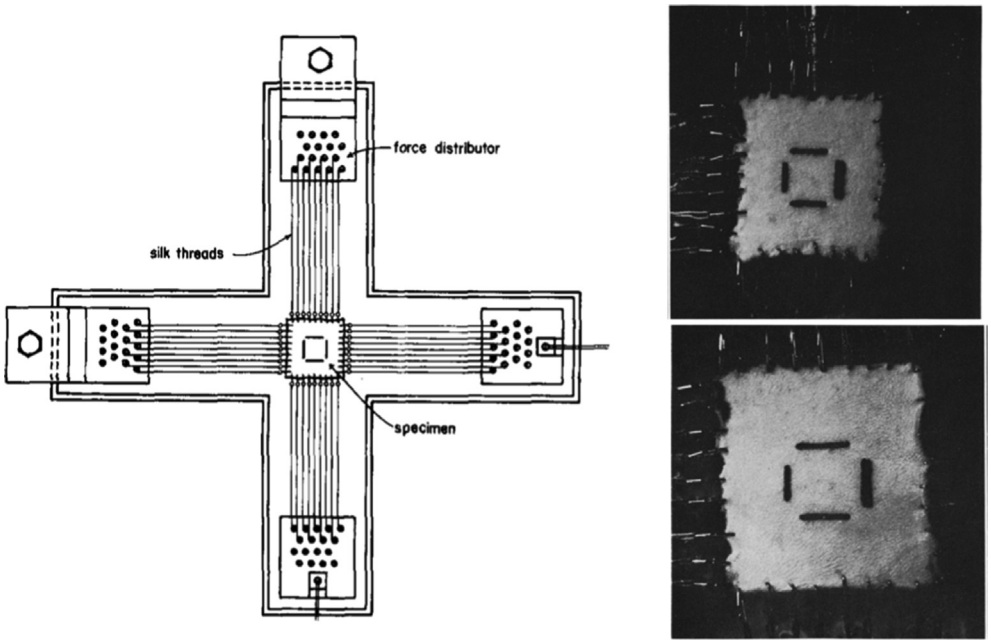

Fig. 2.6. Biaxial stretching setup by Lanir and Fung [109]. Left: Schematic illustration of the setup, with specimen hooking and force distribution. Right: Photographs of undeformed (top) and biaxially stretched (bottom) rabbit skin sample. Marked lines are used to indicate that there was no rotation during stretching.

preconditioning, in the uniaxial (no load in one direction) and the biaxial directions (with one dimension kept constant), for different strain rates and controlled temperatures [41]. Their results are still being used for the construction of phenomenological and microstructural time-dependent models [110,111]. Schneider et al. [112] later used the same setup for the *ex vivo* characterization of human skin.

Biaxial testing produces loading that is closer to the *in vivo* conditions of skin, and provides additional insight into the mechanical parameters of the tissue. While it is possible to fully resolve the mechanical properties of an incompressible isotropic material, it does not suffice to fully determine the constitutive equations an anisotropic material like skin, as pointed out by Holzapfel and Ogden [113]. For a full experimental characterization, more general methods, combining different testing and measurement techniques, are recommended [114].

2.2.3. Bulge tests

Bulge tests (also sometimes referred to as diaphragm or inflation tests) were first introduced by Dick in 1951 [115], for measuring the deformation of human skin. As pointed out by Grahame and Holt [93], the principle is analogous to the suction method, because it consists of creating a difference in pressure between the inner side of the tissue and the outer side. In this case, it is effectuated by injecting a fluid (water [115], or porcine saline buffer (PBS) [61]) into a pressurization chamber, on top of which a circular portion of sample is clamped. With applied fluid pressure, the sample inflates and the external surface forms a bulge. By approximating the deformed bulge to a hemispherical cap, the stretches can be measured by estimating the changes in arc length [116], or by tracking markers on the surface of the tissue [61,117]. The stresses can be computed from the applied fluid pressure using thin-shell theory [61,116], or inverse finite-element analysis [118,119], depending on the assumptions on the deformation state. Assuming that the deforming tissue behaves like a thin membrane and that the radial stress is small compared to the in-plane stresses, a biaxial stress state is also reached in the material [116]. An additional interest of the method is that the injected fluid in the chamber can be also used to hydrate the sample, or control its temperature to physiological levels.

Another challenging venture is the measurement of tensile properties of skin under dynamic loads, to characterize the strain rate sensitivity of the tissue and to study extreme loading conditions. Examples using Split Hopkinson Tensile Bar designs can be encountered [42], but their performance is limited by sample slipping and impedance mismatch. Shergold et al. [44] performed dynamic tests on pig skin in a compression Hopkinson bar using disk-shaped specimens with a thickness of ~2.3 mm and a diameter of 7 mm. With such a low thickness to diameter aspect ratio, friction at the contact surfaces is likely to create pressure differentials (the pressure in the center being higher thanin the periphery) and cause barreling, which is rarely taken into consideration in the experimental protocol. Moreover, dynamic compression is more representative of particular cases such as the response of skin to blast and impact.

2.3. Image/ultrasound based measurement techniques

A considerable obstacle to reliable and accurate measurements of the deformation of skin can come from the mismatch between the estimated deformation and the true deformation, partly due to sample slipping. Estimation of stresses can be complicated in the case of *in vivo* experiments due to the difficulty to resolve between deforming layers of the subject's body.

To address this issue, some researchers have coupled their experimental setups with image or ultrasound-based measurement techniques. These techniques can be used to quantify the error between the applied displacement and the average local displacements in the structure. But it can as well be a useful tool to observe localization of strains and tissue anisotropy, via two-dimensional mapping of strains. Moreover, ultrasound (or also OCT [5,120,121]) measurements can yield valuable out of plane visualization, which allows one to distinguish the different layers being deformed, or heterogeneities that can be indicators of health-related problems. A notable example is the application of elastography, i.e. a mechanical testing device coupled to an imaging apparatus, to detect anomalies such as infections or skin cancer [120,122]. By measuring the degree of distortion under an applied load, local tissue stiffness can be qualitatively observed. Coutts et al. [87] describes an elastograph based on a uniaxial extensometer paired with an ultrasound probe, to distinguish deforming skin from the subcutaneous layer *in vivo* (Fig. 2.7). The same concept has been used for suction devices [77], as a tool to measure simultaneously the bulge height and the deforming layers.

A very common use of imaging techniques to quantify superficial deformation of skin is Digital Image Correlation (DIC). DIC consists of tracking specific markers, speckled randomly on the surface of the sample, during an applied deformation. The recorded sequence of images is then processed and the local displacements are identified by cross-correlation, allowing for the calculation of strains. In addition, three-dimensional deformation can be determined by using a set of two cameras (Stereoscopic Image Correlation). In the context of skin's characterization, it is a very useful tool to observe the anisotropy of a sample, localization or uniformity of stresses, and the coherence between the imposed and real deformations. Fig. 2.8 shows how DIC can be implemented to compare the macroscopic deformation, measured with a displacement sensor (DS), and the local strains via DIC, to account for sample slipping or localized deformations. By coupling a bulge tests with three-dimensional DIC (Fig. 2.9), Tonge et al. [61] succesfully quantified skin's anisotropy, evidenced by a difference in vertical and horizontal displacements of the sample, and an elliptical out-of-plane displacement contour.

To visualize how macroscopic deformations are distributed in the structure, other measurement techniques can be implemented. The reorganization of the collagenous network in skin has been observed *in situ* by Second Harmonic Generation coupled with DIC by Nesbitt et al. on mouse skin [123] and by Small Angle X-ray Scattering (SAXS) by Yang et al. [40] on rabbit skin. Both studies show that collagen fibrils gradually align towards the direction of tension, before eventually undergoing stretching, sliding, and delamination, which precedes fracture. This fiber recruitment process has also been recorded with *ex situ* SEM by Yang et al. [40] for rabbit skin (Fig. 2.10), and earlier by Brown [67] for human skin. Tensile tests were interrupted at different increments of strain, and samples were fixed prior to SEM imaging. This is further evidenced by Transmission Electron Microscopy of pig skin, before and after tensile testing (Pissarenko et al. [12]). When observed in a plane parallel to the outer surface of the dermis, collagen fibers, initially crimped and oriented in various in and out of plane directions, appear to have straightened and aligned in the tensile direction after extension to failure (Fig. 2.11).

2.4. Summary of experimentally observed features

It can be challenging to compare *in vivo* and *ex vivo* experimental results given the large differences in terms of protocol, sample configuration, and spanned deformations. However, good agreements have been observed when comparing low deformation curves, obtained from the same animal, for identical types of loadings [68]. An additional feature is the degradation of the skin in *ex vivo* testing, which starts immediately after removal from host. Preservation methods vary and this introduces additional variations in results.

With considerable variations due to specifics of the experimental protocol, e.g. boundary conditions, sample geometry, measurement accuracy, or spanned deformation, as well as inter-species and inter-subject variations, it is difficult to quantitatively obtain comparable mechanical parameters. A non-exhaustive summary of reported values of the tangent modulus of skin encountered in the literature is presented in Table 2.1. It highlights the high discrepancy between these results, and corroborates observations from Rodrigues et al. [35].

Fig. 2.12a presents a typical stress-strain curve for skin, obtained from uniaxial tensile tests. The so-called J-curve is observed for a broad range of collagenous materials (tendon, arterial wall, epimysium [124]) and can be decomposed in three distinct regions, which are associated with different deformation mechanisms at the microstructural level:

- the toe region, where collagen fibers gradually align with the tensile direction;
- the heel region, where the rotation continues and aligned fibers start uncrimping;
- the linear region, where aligned and straightened fibers undergo stretching, sliding past each other, delaminating, and ultimately failing, causing macroscopic damage and failure.

Thus, isolating a single value for the tangent modulus of a nonlinear curve depends highly on the portion of the stress-strain curve that is chosen (or accessible) to evaluate it, which affects the wide disparity in reported data that can be seen in Table 2.1. Moreover, tissue anisotropy, mainly caused by the distribution of collagen fibers (and responsible for the Langer lines), makes it impossible to fully describe the response of skin under tensile loads, without prior knowledge of the structural arrangement of its constituents, or

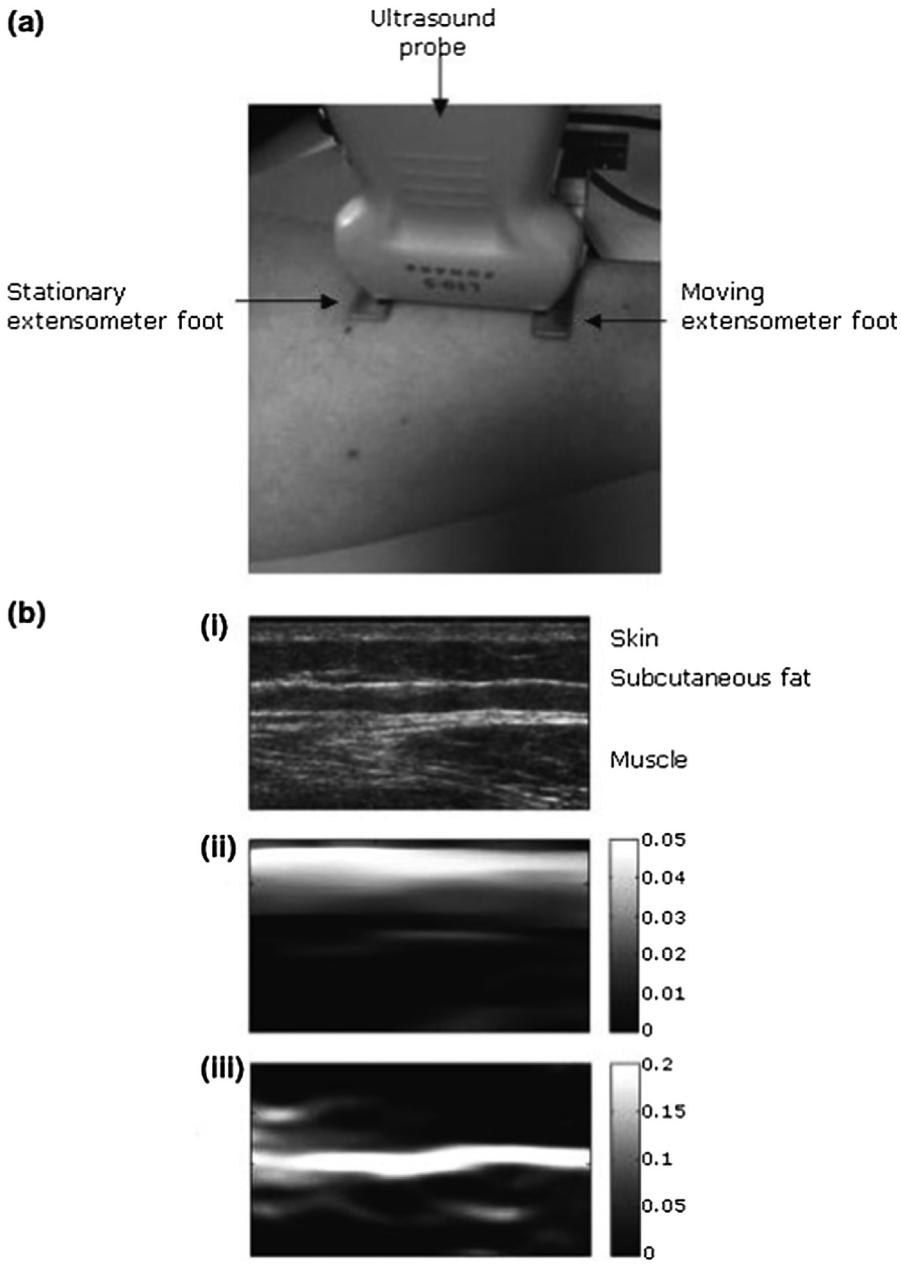

Fig. 2.7. (a) Photograph of a uniaxial extensometer attached to forearm skin of a human subject, paired with an ultrasound probe for elastography. (b)(i) Ultrasound image with corresponding examples of (ii) tensile normal strain elastogram and (iii) shear strain elastogram. Reprinted from Coutts et al. [87].

without a certain set of assumptions with respect to this arrangement.

Some further characterization of skin's nonlinear and anisotropic behavior needs to be implemented to yield a better description. Mechanical models that attempt to do so are developed in the following chapters. Even qualitatively, some important factors cause rather large variations to the experimental result. Fig. 2.12b. shows that for identical experimental conditions, there can be important inter-sample variations, even for samples taken from the same species, or the same specimen.

2.4.1. Scaling of skin mechanics across species

It is rather common to expand results observed for a given animal to the behavior of human skin, but such considerations need to be addressed with caution. Although there are many commonalities in the structure of mammal skins, some fundamental differences can affect the mechanical behavior. Allometric considerations have to be made and a guiding parameter is that the volume (and therefore the mass M) increases with the cube of the radius R, assuming a spherical body. We consider an average thickness t of the

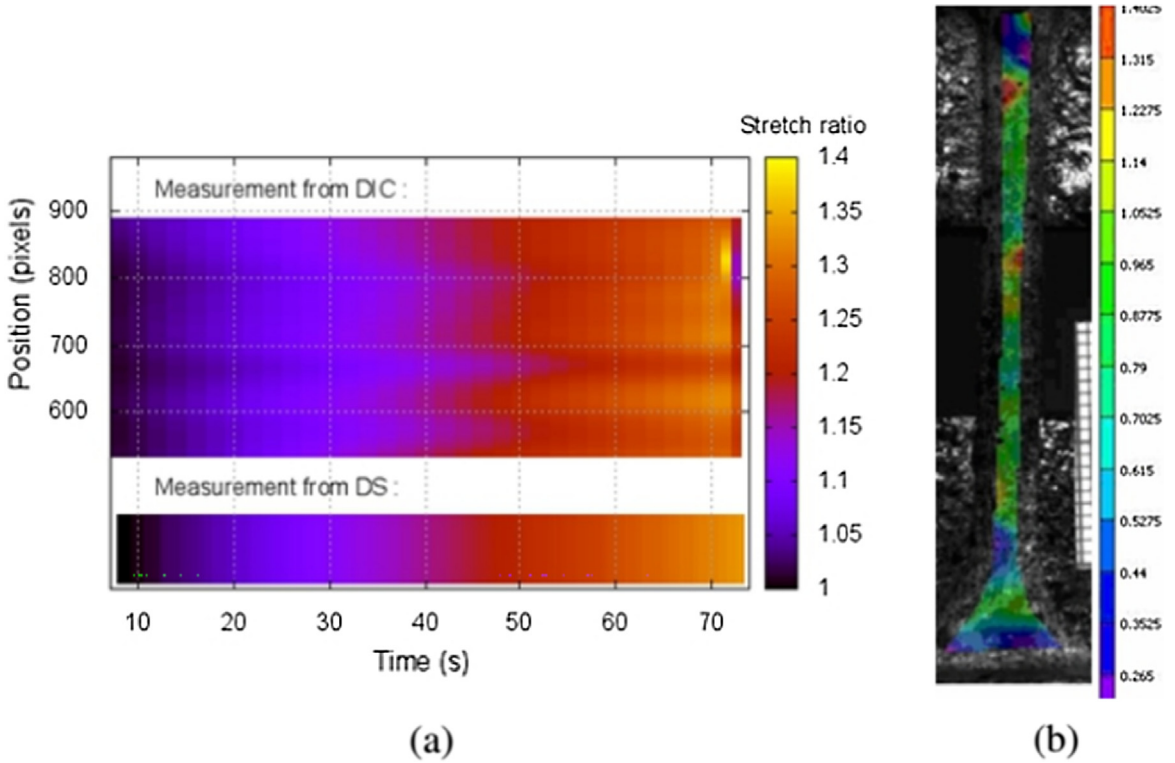

Fig. 2.8. (a) Comparison of stretch measurement from DIC and Displacement Sensor (DS) over the length of the specimen, throughout the duration of a given tensile test. (b) Distribution of local Lagrangian strains just before rupture of a dumbbell shaped skin sample. From Ni Annaidh et al. [54].

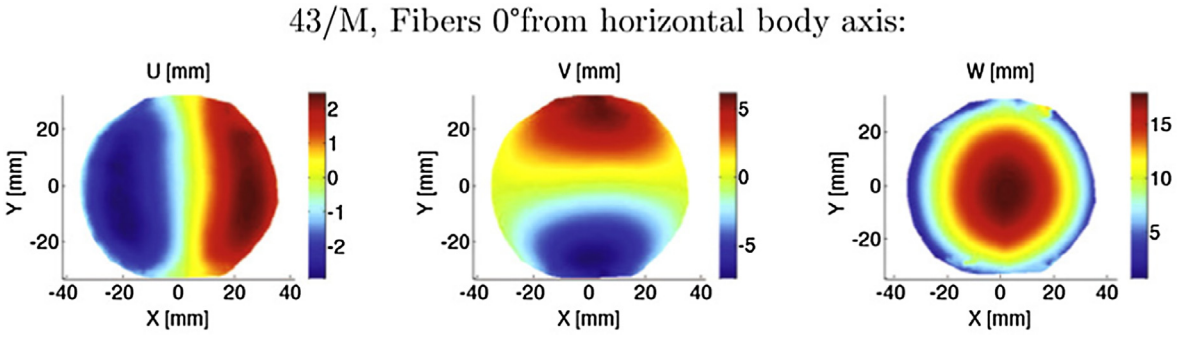

Fig. 2.9. Three-dimensional DIC contours of displacement components in the body axis coordinates ((U, V): in-plane, W: out-of-plane) for a 43-year-old male from *in vivo* suction tests on human subjects. Anisotropy of the tissue is evident from the rotated U and V contours and the elliptical W contour. From Tonge et al. [61].

skin and an average density ρ_s. Considering that skin envelops all internal organs, it must contain them without deforming too much itself. A schematic representation of the problem is given Fig. 2.13a. By isolating the bottom hemispherical envelope of skin from the top part, the section of skin is subjected to the effect its own weight, as well as the internal forces at the interface with the upper half. The equilibrium of the isolated part can be expressed as follows:

$$2\pi R t \sigma_i = 2\pi R^2 t \rho_s g \tag{2.7}$$

where σ_i is the internal normal stress at the interface. The mass of the lower envelope is equal to the product of its density ρ_s times the volume, where the volume of the hemispherical thin shell is approximated by $2\pi R^2 t$. Further simplification leads to the following relationship:

$$\sigma_i = \rho_S g R \tag{2.8}$$

Then, for a spherical body, we have:

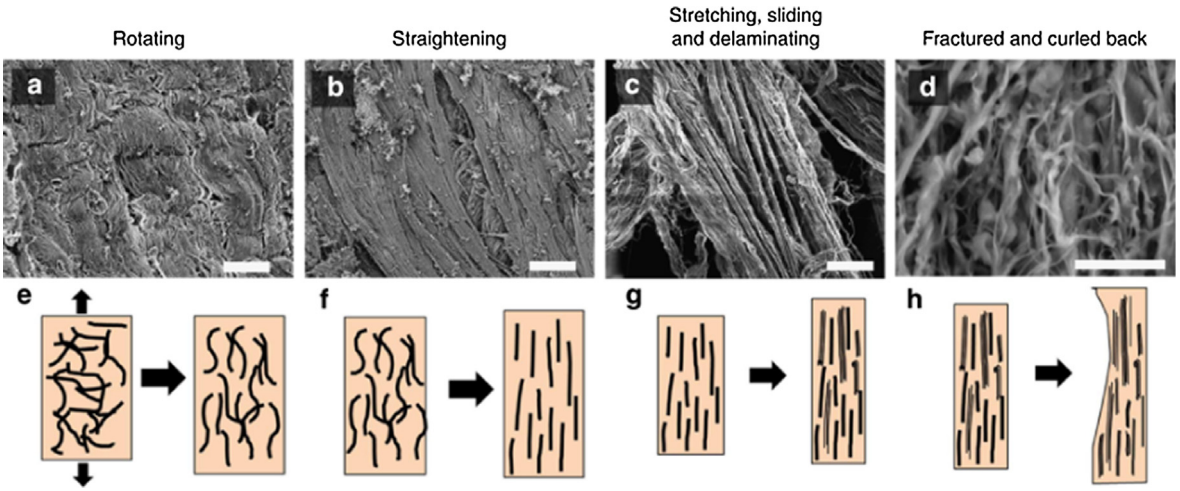

Fig. 2.10. Collagen fiber recruitment and deformation during tension, visualized by *ex situ* SEM (a–d), and schematic illustration of the process of deformation (e–f). Reprinted from Yang et al. [40].

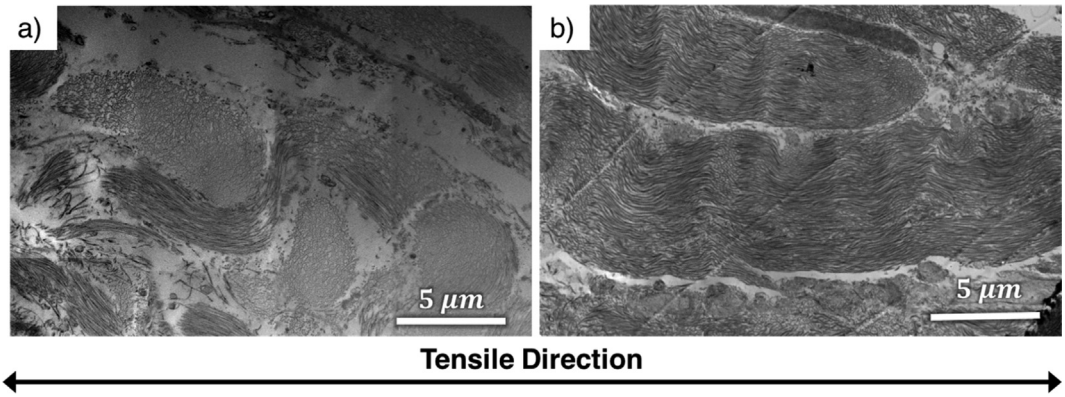

Fig. 2.11. *ex situ* TEM of pig skin taken before testing (a) and after sample failure (b). Slices were cut parallel to the outer surface of the dermis. Micrographs show that in the underformed configuration (a), crimped collagen fibers form a three dimensional network and do not seem to follow any preferred orientation. After deformation (b), straightened collagen fibers have reoriented in the tensile direction and lie in-plane. (Pissarenko et al. [12]).

$$R \propto \left(\frac{3}{4\pi}M\right)^{1/3} \tag{2.9}$$

Which leads us to the following allometric relationship:

$$\sigma_i \propto M^{1/3} \tag{2.10}$$

By considering an equivalent level of "sagging" strain for each species, this implies that the tangent modulus of skin should scale with body mass to an exponent of 1/3, assuming that $\sigma_i \propto E\varepsilon_i$. We compared this prediction to a set of experimental results collected in the literature, most of which are presented in Table 2.1. To avoid disparity, we gathered data for *ex vivo* uniaxial tensile experiments performed under similar conditions (strain rate, temperature, type and region of the sample) for all types of orientations (Fig. 2.13b) from animals ranging from a rat ($M \approx 10^2$ g) [38,39] to a rhinoceros ($M \approx 10^6$ g) [83]. The most consistent parameter appears to be the slope of the linear region of the J-curve. A least-squares approach was used to fit two power laws: one with unrestricted parameters (blue dotted line) yields $y = 1.94x^{0.34}$ with an R-square coefficient of 0.86. For the second curve (red dotted line), the exponent was fixed to 1/3, as predicted by our approximation, and $y = 2.21x^{1/3}$ with an R-square coefficient of 0.84, showing a satisfying agreement with our prediction. This correlation is indeed fascinating and demonstrates that the slope of the linear region increases with the mass of the animal and scales with an allometric exponent of 0.33, as predicted from a simple dimensional analysis.

2.4.2. Alignment with the Langer lines

The orientation dependence is perhaps the most fundamental mechanical characteristic of skin and can be directly linked to Langer's description of lines of pre-stress, and consequently skin's anisotropy. It has been repeatedly reported that when pulled along

Table 2.1
Comparative analysis of reported tangent modulus, failure strain, and failure stress found in previous studies (ranked by chronological order). N.A. = Not Applicable; N.R. = Not Reported.

Reference	Year	Tested Species - Region	Type of Experiment	Tangent Modulus E (MPa)	Failure Strain	Failure Stress (MPa)
Jansen and Rottier [74]	1958	Human - Abdomen	*Ex vivo* – Uniaxial tension	2.9–54.0	0.17–2.07	1–24
Stark et al. [75]	1977	Human - Back	*In vivo & ex vivo* – Uniaxial tension	0.26–0.83	0.16–0.52	N.A.
Vogel and Hilgner [38]	1979	Rat – Dorsal Skin	*Ex vivo* – Uniaxial tension	35.2–36.9	0.63–0.86	10.6
Agache et al. [53]	1980	Human - Back	*In vivo* – Torsion	0.42–0.85	N.A.	N.A.
Dunn and Silver [145]	1983	Human – Abdomen and Thorax	*Ex vivo* – Uniaxial tension	0.1–18.8	1.0	7
Vogel [76]	1987	Human – N.R.	*Ex vivo* – Uniaxial tension	15–150	0.3–1.15	5–32
Haut [39]	1989	Rat – Dorsal Skin	*Ex vivo* – Dynamic tensile tests	4.4–11.1	0.52–1.25	1.2–3.2
Shadwick et al. [83]	1992	Rhinoceros – Back and Flanks	*Ex vivo* – Uniaxial tension	107.8–237.3	0.24–0.33	14.5–30.5
Diridollou et al. [77]	1998	Human – Forehead and Arm	*In vivo* – Suction	0.12–0.25	N.A.	N.A.
Ankersen et al. [46]	1999	Pig – Back and Abdomen	*Ex vivo* – Uniaxial tension	N.R.	0.49 + /-0.28	14.5 + /-7.0
Hendriks et al. [78]	2003	Human - Forearm	*In vivo* - Suction	0.056 + /-0.021	N.A.	N.A.
Khatyr et al. [79]	2004	Human - Tibia	*In vivo* – Uniaxial tension	0.13–0.66	N.A.	N.A.
Ventre et al. [82]	2006	Calf/Bovine Skin - Back	*Ex vivo* – Uniaxial tension	50.11 + /-7.47	0.59 + /-0.06	16.80 + /-1.95
Jacquemoud et al. [80]	2007	Human – Forehead and Arm	*Ex vivo* – Uniaxial tension	19.5–87.1	0.27–0.59	5.7–12.6
Jachowickz et al. [81]	2007	Human – Face and Forearm	*In vivo* – Indentation	0.007–0.033	N.A.	N.A.
Pailler-Mattei et al. [52]	2008	Human – Arm	*In vivo* – Indentation	0.0045–0.008	N.A.	N.A.
Zhou et al. [47]	2010	Pig – Abdomen	*Ex vivo* – Uniaxial tension	0.9–4.2	1.23–1.26	0.25–1.0
Lim et al. [42]	2011	Pig – Back and Abdomen	*Ex vivo* – Dynamic tensile tests	N.R.	0.16–0.30	0.1–0.8
Wong et al. [25]	2012	Pig – Eyelid, Back, Cheek, Forelimb, Abdomen, and Chest	*Ex vivo* – Uniaxial tension (scarred tissue)	0.121–0.532	N.R.	N.R.
Ni Annaidh et al. [54]	2012	Human – Back	*Ex vivo*– Uniaxial tension	83.3 + /-34.9	0.54 + /-0.17	21.6 + /-8.4
Gallagher et al. [56]	2012	Human – Back	*Ex vivo*– Uniaxial tension	146–171	0.37–0.55	30–37
Sherman et al. [11]	2016	Rabbit – Back and Belly	*Ex vivo* – Uniaxial tension	11.5–40.4	0.74–1.33	4.52–16.75

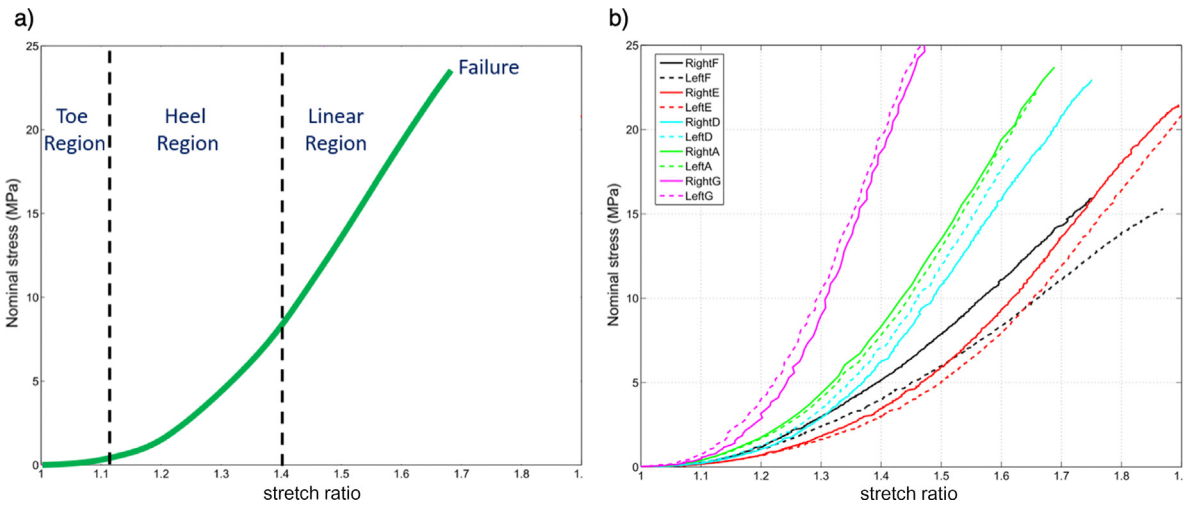

Fig. 2.12. (a) Typical J-curve response of skin under uniaxial tension, showing three distinct regions. Depending on the isolated portion, the measurement of the tangent modulus can considerably vary. (b) Stress-stretch response from *in vitro* uniaxial tensile tests of adjacent samples human back skin, with similar orientation. Colors indicate different subjects while solid and dashed lines indicate samples to the right and left of the spinal line respectively, illustrating inter-subject and intra-subject variations. Adapted from Ni Annaidh et al. [54].

the principal alignment direction of collagen fibers (i.e. parallel to the Langer lines), skin exhibits a higher ultimate tensile stress and higher tangent modulus [42,46,54,107], illustrated here in Fig. 2.14. The influence of the Langer lines on failure stretch are disputable, and region dependence needs to be taken into account, see Section 2.4.3.

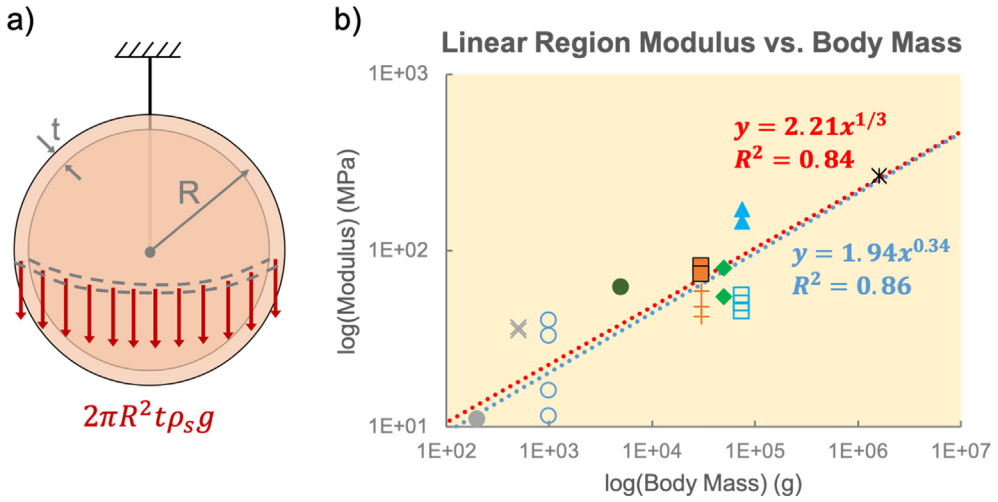

Fig. 2.13. (a) Schematic representation of a spherical body with an outer layer of skin. The skin envelope must be able to withstand its own weight with limited stretch; by isolating the top hemisphere we see that the total vertical force is proportional to the mass of the lower hemisphere. (b) Logarithmic plot of the slope of the linear region of the stress-strain curve versus body mass. Data for *ex vivo* uniaxial tensile tests of rat (● - Haut [39], × - Vogel [76]), rabbit (○ - Sherman et al [11]), cat (● - Veronda and Westmann [135]), pig(■ - Ankersen et al. [46], + - Pissarenko et al. [12]), calf (◆ - Ventre et al. [82]), human (□ - Ni Annaidh et al. [54], ▲ - Gallagher et al. [56]), and rhinoceros (✳ - Shadwick et al. [83]) skins. Blue and red dotted lines represent least-squares fit power law functions with unrestricted parameters and fixed exponent, respectively. Experiments were generally conducted with fresh skin, at ambient temperature, at strain rates around 10^{-2} s^{-1}. (For interpretation of the references to color in this figure legend, the reader is referred to the web version of this article.)

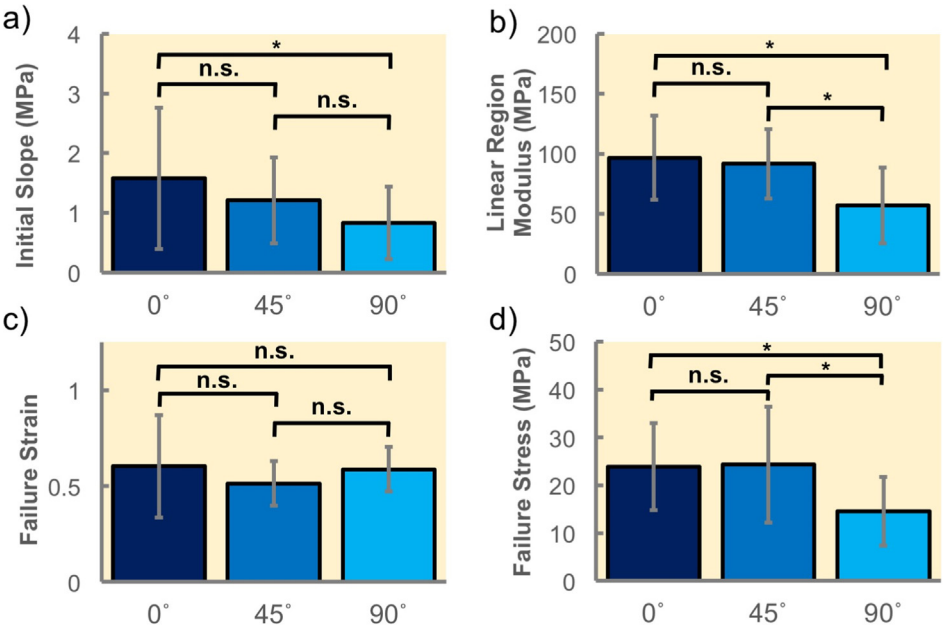

Fig. 2.14. Influence of orientation on the (a) initial slope, (b) linear region modulus, (c) failure strain, and (d) failure stress for human back skin, tested uniaxially. Samples were taken parallel (0° - N = 16), diagonally (45° - N = 26), and perpendicularly (90° - N = 14) to the Langer lines, mean values and standard deviations are shown. Comparisons where no statistically significant difference was observed are marked with an "n.s." symbol. Otherwise, asterisk (*) symbols are marked when $p < 0.05$. N designates the number of tested samples. Adapted from Ni Annaidh et al. [54].

2.4.3. Region dependence

The findings of Agache et al. [53] exemplify how different locations of the body have varying responses to deformation, where the belly region needs to be highly deformable in the transverse direction while other areas such as the back tend to be thicker and stiffer in order to protect the spine. Values reported in Table 2.1 illustrate this suggestion, and particularly results reported by Ankersen et al. [46] where the back and belly regions of excised pig skin were tested uniaxially (see Fig. 2.15). Their results demonstrate that location does not only affect elasticity but also the degree of anisotropy within the tissue, which can be understood by the fact that

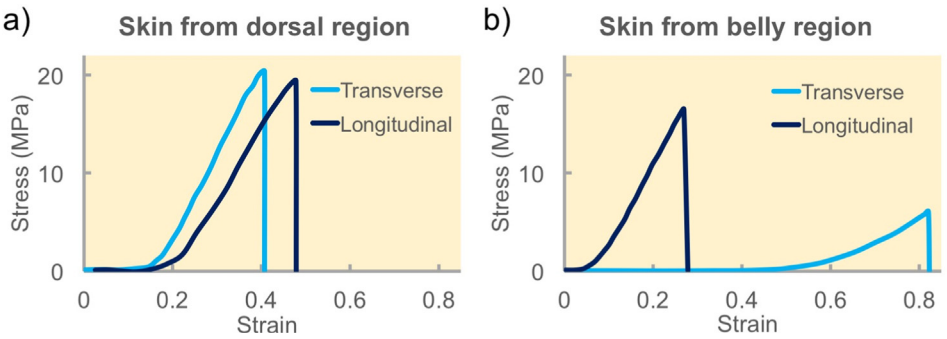

Fig. 2.15. Stress-strain curves of pig skin tested in longitudinal (parallel to spine) and transverse (perpendicular to spine) directions via uniaxial tensile tests: (a) back, (b) belly, showing the influence of the tested region. From Ankersen et al. [46].

each region needs to sustain a different set of deformations of varying amplitudes. This degree of anisotropy was shown to significantly vary between two comparable specimens as well by Lanir and Fung [41] from their biaxial testing experiments.

2.4.4. Influence of aging

Age is a significant factor affecting the mechanical response of skin. As mentioned previously, certain *in vivo* experimental techniques can be applied to assess the aging of the tissue depending on observable parameters such as apparent stiffness, or relaxation time. Boyer et al. [63] used the Cutometer® and an indentation device on human skin to show that apparent stiffness and the elasticity ratio U_R/U_E decrease with increasing age of subject, while the U_V/U_E ratio increases. Similar trends for U_V/U_E were reported from torsion tests on male and female subjects by Agache et al. [53]. However, the elasticity ratio appears to increase until the age of 30 before eventually decreasing, which agrees with some other reported findings [90,93]. It is worth noting that this increase is generally more pronounced amongst female subjects, which can be linked to morphological adaptations for pregnancy, pointing out the influence of gender on experimental measurements.

2.4.5. Hydration

Hydration is an external parameter of significant contribution to skin's elasticity. Its impact has been studied through variations of external humidity [40,61,125,126], or application of hydrating agents or water immersion [103,120,121,127,128], and reported for the first time by Christensen et al. [127]. They tested the external surface of skin with an electrodynamometer and noted a softening response after application of water and emollient. Later, Auriol et al. [129] performed *in vivo* suction experiments on human subjects and observed an increase up to 14% in skin's extensibility, depending on the time water was applied prior to testing, and this number rose to 21% when women were considered apart from men. Hydration mostly affects the stiffness of the stratum corneum [103,125], which for women represents a higher ratio of the total skin thickness, suggesting that its changes in mechanical response have a more perceptible effect on the overall response of the tissue. The mechanical sensitivity of the stratum corneum to humidity has been quantified by Levi et al. [125], who measured an increase in thickness and a decrease in Young's modulus with water content. Yang et al. [40] report a significant stiffening of rabbit skin after drying (Fig. 2.16). The stiffness of the skin scales with the reduction in weight due to water loss. Dry skin, with a 35% reduction of weight due to dehydration, has a radically altered mechanical response. Nonetheless, Tonge et al. [61] report that variations in the humidity level of the testing chamber have no significant effect on bulge

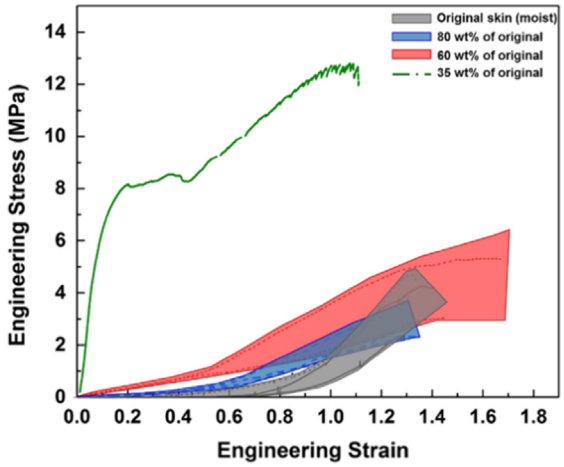

Fig. 2.16. Stress-strain curves of original moist skin and dehydrated skin of different amounts. Adapted from Yang et al. [40].

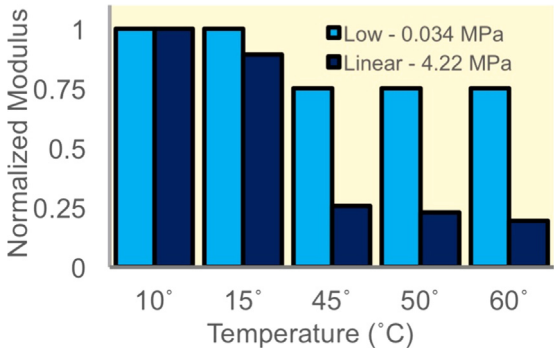

Fig. 2.17. Influence of external temperature on tangent modulus in the low strain and linear regions of the J-curve, for tensile tests on pig skin at a strain rate of 0.01 s^{-1}. Values are normalized by their maximum to highlight decreasing trend. Adapted from Zhou et al. [47].

tests on human skin.

2.4.6. *Influence of temperature*

Thermal effects have also been studied, due to their notable interest in dermatological and surgical applications. Zhou et al. [47] tested uniaxially pig belly skin under temperatures ranging from 10 ˚C to 60 ˚C and observed a softening response, marked by a longer toe region and a decrease of the Young's modulus in the linear region with increasing temperature (Fig. 2.17). According to their findings, high temperatures damage the tissue and denature collagen which loses its structural integrity and thus its mechanical properties, along with other effects such as changes in hydration and water intake.

2.4.7. *Strain-rate sensitivity*

The time-dependent behavior of skin can be observed by changing the strain rate of the applied load. Zhou et al. [47] conducted experiments on excised pig belly skin samples under uniaxial tension, with loading rates ranging from 0.25% s^{-1} to 10% s^{-1}. The reported curves (Fig. 2.18) show a reduced toe region and, most importantly, a hardening response with increasing crosshead speed. The authors suggest that higher strain rates increase the shear interactions between the structural elements of the dermis and alter the movement of internal fluids, thus affecting the viscoelasticity and dissipative behavior of the tissue. Strain-rate sensitivity of skin was suggested earlier by Finlay [57], who stated that skin exhibits tixothropy. It was further validated by other studies involving uniaxial [12,42,130], biaxial [41] and compressive [10,44] tests. Pissarenko et al. [12] further illustrated this effect by directly changing the applied strain rate during uniaxial tensile testing of porcine skin, when the J-curve reaches the linear regime, in an attempt to eliminate the inter-sample variability. Results show that the slope of the linear region noticeably increases with an increase in strain rate, and the transition is marked by a brief jump in stress, before reaching a new linear regime. For a decrease in strain rate, the slope of the linear region decreases, and a short relaxation is observed before linear stabilization.

2.4.8. *Stress-relaxation and creep*

Standardized measurements by the suction and torsion methods include time-dependent parameters, namely U_V, U_F, and U_R (Figs. 2.2 and 2.3), which, depending on the controlled input (i.e. applied force or applied displacement), can be assimilated to creep or stress relaxation tests. Time-dependent parameters have shown to be a good indicator of skin aging [53], and location [60]. Direct stress-relaxation tests have been conducted by Lanir and Fung [41] with their biaxial testing setup, and show that the relaxation response is dependent of the strain or initial stress at which the sample is relaxed. This is comparable to the observations later made

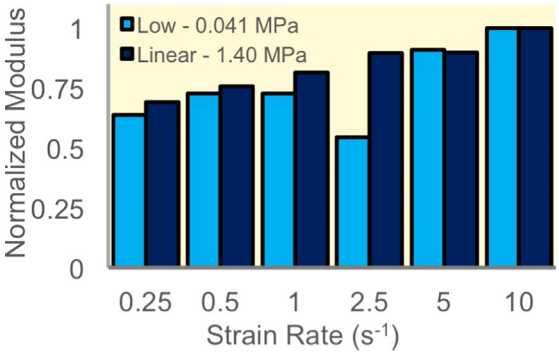

Fig. 2.18. Influence of strain rate on tangent modulus in the low strain and linear regions of the J-curve, for tensile tests on pig skin at a temperature of 45˚C. Values are normalized by their maximum to highlight decreasing trend. Adapted from Zhou et al. [47].

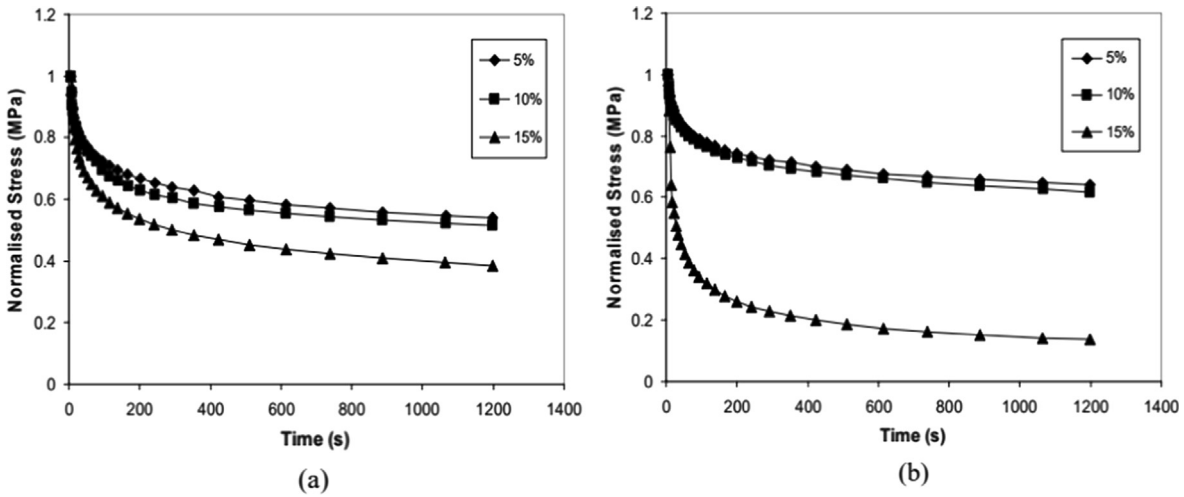

Fig. 2.19. Stress relaxation trend of pig skin at different strains in (a) samples parallel to the spine, and (b) samples perpendicular to the spine direction. All stresses are normalized to the initial stress. From Liu and Yeung [131].

by Liu and Yeung [131], although the authors emphasize the fact that the stress relaxation rate varies according to the region of the J-curve that has been reached as well as the sample orientation (Fig. 2.19). Relaxation curves are generally normalized by the maximum stress, which is why these results need to be addressed carefully because stress levels are different parallel and perpendicular to the spine due to of skin anisotropy.

2.4.9. Irreversible damage and the Mullins effect

The changing relaxation behavior with repeated cycles or for different levels of relaxation stress suggests that the tissue undergoes irreversible deformations that start accumulating after stretching. This may principally be caused by fibers realigning permanently in the principal direction of tension and eventually sliding past each other [40,67,123]. A consequence of this damage-induced behavior is the Mullins effect, commonly encountered for filled rubber materials, which can be examined during cyclic tests at large deformations [132] (Fig. 2.20a). The non-overlapping loading curves imply a loss of viscoelastic energy [65] and material softening

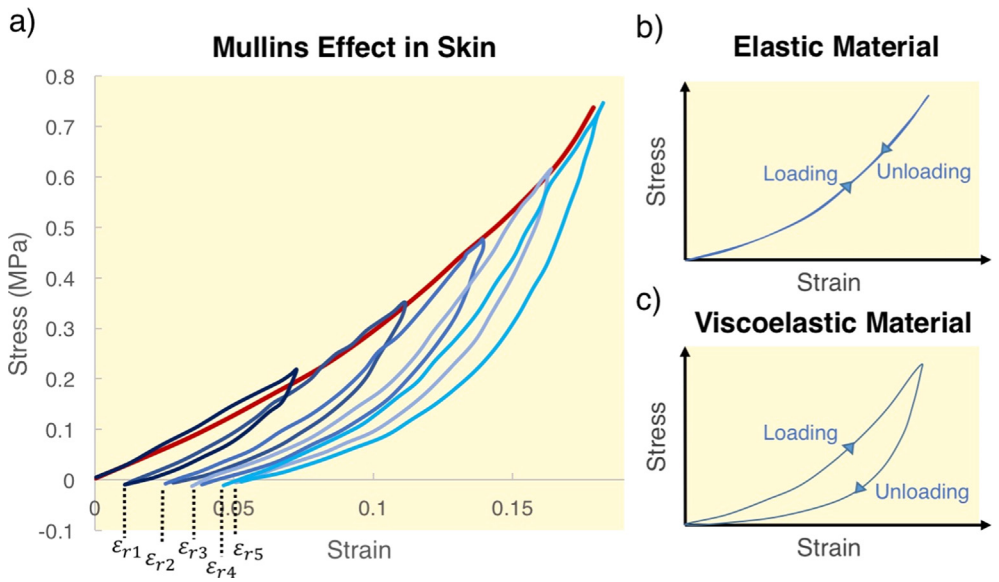

Fig. 2.20. (a) Experimental results obtained from the skin of an 18-month male mouse, adapted from Muñoz et al. [132]. The primary loading curve of the cyclic test (dark blue line) closely follows the monotonic one (red line), which describes an envelope curve for the cyclic test. Each reloading cycle then follows the previous unloading curve, a phenomenon called the Mullins effect. After each unloading cycle, remnant strains ε_r remain, indicating irreversible damage in the material. (b) For an elastic material, loading and unloading follow the same path. (c) In the case of a viscoelastic material, hysteresis can be observed, reflecting the dissipated viscoelastic energy. (For interpretation of the references to color in this figure legend, the reader is referred to the web version of this article.)

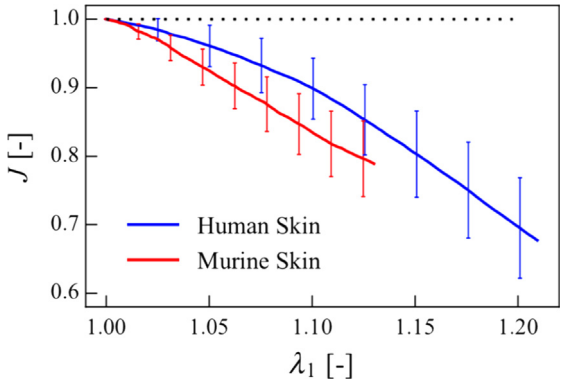

Fig. 2.21. Loss of volume with applied stretch in human and murine skin samples during uniaxial tension tests, expressed by normalized volume change $J = V/V_0$. The dotted line indicates a constant volume ($J = 1$). Reproduced from [133].

[50]. Upon reloading, the material follows the previous unloading curve, showing that there is no further damage. The typical responses for nonlinear elastic and nonlinear viscoelastic materials are shown in Fig. 2.20b. and c, showing that the loading and unloading paths are different for the latter. In their study, Muñoz et al. [132] also showed that for each testing cycle, residual strains accumulate, mainly for deformations above 10%, indicating irreversible damages in the tissue at this level. Values of these remnant strains after each loading cycles are marked in the abscissa in Fig. 2.20a.

In contrast, preconditioning consists of reaching overlapping hysteresis cycles at low strains (< 10%) to ensure repeatability and reduce inter-sample variations [56,131], by maximizing fiber alignment, and has been first introduced by Fung [36].

2.4.10. Volume changes

It is often assumed that biological tissues are incompressible, suggesting that no change in volume occurs during deformation. This has substantial consequences on the constitutive modeling of the material, where the incompressibility condition yields an additional relationship between the model invariants, and reduces the material constants that need to be determined. As a result, the out-of-plane deformation component is sometimes neglected in experimental characterization, as it can be described by the in-plane components [7]. However, recent studies involving image-based analyses of the lateral and out-of-plane deformations in skin during uniaxial *ex vivo* tensile tests report variations in the volume ratio J. Wahlsten et al. [133] measured a decrease of the volume ratio with increasing tensile deformation for murine and human skins [133], as illustrated in Fig. 2.21. The authors attribute this trend to an outflow of the internal fluids, leading to volume loss, explaining also the irreversible cyclic behavior of the tissue. Similar observations were made on porcine skin by Pissarenko et al. [12], with some samples showing a gradual decrease of the volume ratio with applied tension. At high strains, liquid drops start forming on the skin surface, confirming a loss in water content. Interestingly, for some samples closer to the belly region an increase in volume is measured, suggesting that some regions can exhibit auxeticity, an effect that was also suggested by Lees et al. for cow teat skin [134] and Veronda and Westman for cat skin [135]. This property could be due to a specific arrangement of the fiber network in the tissue, but requires further microscale characterization.

It is more difficult to confirm that volume changes occur in the *in vivo* configuration. The out-of-plane deformation cannot be estimated using conventional imaging techniques, and different lateral constraints. Still, comparable trends in lateral contraction were reported [133].

2.4.11. Storage conditions

Recently, Caro-Bretelle et al. [49] have pointed out the importance of storage conditions of skin samples prior to testing by quantifying the softening behavior after cyclic loading of pig skin, either fresh or stored under different conditions. Their results showed that conserving in saline solution or freezing the skin significantly and irreversibly alters the mechanical properties, while cryopreservation appears as the only suitable method for maintenance, if not tested fresh.

The vast amount and variety of work that has been done on experimental characterization of skin's viscoelastic properties provides a broad framework to gain a better understanding of skin mechanics. It is clear that skin is a *nonlinear, anisotropic, viscoelastic* structural material that is sensitive to temperature, humidity, aging, UV exposure [136], radiation, as well as other external factors. Despite the complexity of providing a fully descriptive mechanical model for skin, researchers have attempted to predict its mechanical behavior under certain limited conditions and hypotheses. The following section describes some of the nonlinear elastic and viscoelastic models that have been implemented to this end.

3. Constitutive and semi-structural models of skin mechanics

Experimental studies on skin's mechanical properties often report values for an elastic modulus. In most cases, it is calculated by isolating the slope of a quasilinear portion of the stress-strain curve, although some authors have their own way of estimating it. Nonetheless, the span of the measured curve varies from one study to another, yielding different possibilities for the calculated elastic

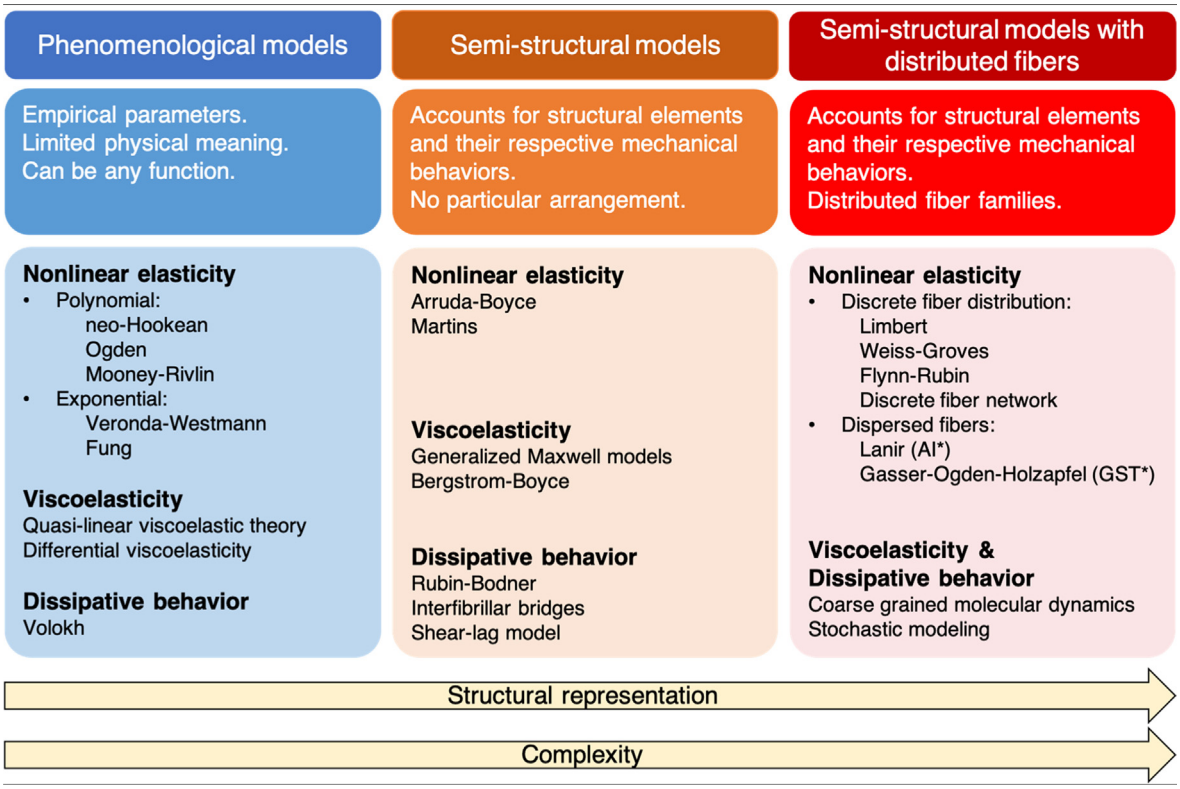

Fig. 3.1. Summary of constitutive models used to represent the nonlinear elasticity, the viscoelasticity, and the dissipative behavior of skin, classified into three different categories. A few examples are listed for each category, some of which are presented in this review. Phenomenological models of nonlinear elasticity are not further developed, due to their inability to capture tissue anisotropy. As the complexity increases, the description of the materials structure and microscale behavior is improved. (*AI: angular integration; *GST: generalized structural tensors).

modulus. Considering the skin's nonlinear and anisotropic behavior, limiting the description of the tissue response to a single linear parameter can be misleading, and can result in inconsistencies. It is therefore important to define and use more complete models that accurately describe skin mechanics, and incorporate its structural arrangement. Moreover, viscoelasticity and loading history dependent processes, such as damage, need to be considered. It is generally done by strain or stress-based linear decomposition of the elastic and viscous behaviors for viscoelasticity. The dissipative behavior, illustrated for example by the Mullins effect in loading-unloading experiments, is either described by the introduction of dissipative factors in the energy function, or by including shearing or friction interactions between components of the structure.

Fig. 3.1 summarizes the most commonly encountered models for skin and other soft tissues, sorted in three main categories:

– phenomenological models, where the response is essentially based on empirical observations. For the most part, these models were initially introduced for the description of rubber-like materials and polymers, and their use was extended to biological tissues, as a first approximation and as an attempt to fit the J-curve. Although phenomenological descriptions of nonlinear elasticity have been widely used in the literature to model the mechanical response of skin, mainly for their ease of implementation, several shortcomings limit their applicability, and the obtained parameters tend to lack physical meaning. Some examples are the Ogden model, the Mooney-Rivlin model, or the Fung model [48,51,124,137-139], as listed in the first column of Fig. 3.1. Most of these descriptions are isotropic, and as a result fail to capture the anisotropy of the tissue, which eventually yields inconsistent results depending on sample orientation, location on the body, or testing conditions. The obtained parameters can lead to ambiguous interpretations, so the implementation of such models is not recommended, and is not further developed in this review. Nonetheless, hyperelastic constitutive laws can be encountered for the representation of the nonlinear elastic behavior of the ground matrix in semi-structural models, with some examples developed in the following section.
– In semi-structural models take into account the constituents of the material and include their respective mechanical behaviors, and potentially their relative interactions. An advantage of such a representation is that some characteristics of the material behavior can be attributed to some specific constituents, or their structure. The case of skin, this particularly involves the distinction between the contribution of the constitutive fibers, from the contribution of the ground matrix. For example, material anisotropy can be included by introducing preferred directions in the material, along which some families of fibers can be aligned, or viscoelasticity can be solely attributed to the surrounding matrix.
– Semi-structural models with distributed fibers. In this category of models, the fibrous network of biological tissues is represented

using fiber families with distributed orientations, embedded in an isotropic matrix. The anisotropy of the tissue is thus mostly attributed to the splay of collagen fibers, and sometimes elastin. This distribution is either described by a discrete number of preferred directions, or by introducing fiber dispersion around the principal orientations. Dispersion can be represented using a pre-selected distribution function for the angular orientation of the fibers, integrated at each time step of the resolution, in which case the approach is called "angular integration" (AI), or directly incorporated into a generalized structure tensor, also referred to as the GST approach. These methods are further developed in the sections below.

Semi-structural models, due to their increased level of complexity, often introduce considerably more parameters, which can be associated with specific components or physical processes within the tissue. Their implementation requires some prior knowledge of the structure of skin, which can be identified using various microscopy imaging techniques such as scanning electron microscopy, transmission electron microscopy, histology, or second harmonic generation imaging. This information, along with some additional knowledge of the mechanical properties of the material constituents, obtained from small scale characterization, can be used to pre-set some constitutive parameters and consequently reduce the number of parameters to estimate.

Note that more complete representations of skin's behavior can be obtained by coupling different constitutive models for non-linear elasticity, viscoelasticity, and dissipative behavior. The following sections provide a more detailed review of some of the models that have been successfully implemented for skin for each of these properties. Their respective advantages and limitations are also discussed, with the idea in mind to provide some guidelines for selecting the appropriate model, for given experimental conditions or specific testing criteria.

3.1. Continuum description and constitutive framework

We start by assuming that the material is initially in a stress-free reference configuration Ω_0. The position of a material point in the reference state is described by its coordinates vector $\boldsymbol{X}$. In the deformed current configuration Ω, the spatial position of this point is described by $\boldsymbol{x} = \varphi(\boldsymbol{X})$. The deformation gradient $\boldsymbol{F}$ is defined as:

$$\boldsymbol{F}(\boldsymbol{X}) = \frac{\partial \varphi(\boldsymbol{X})}{\partial \boldsymbol{X}} \tag{3.1}$$

The local change in volume ratio is indicated by $J = \det(\boldsymbol{F})$. We also define the right Cauchy-Green deformation tensor $\boldsymbol{C} = \boldsymbol{F}^{\boldsymbol{T}}\boldsymbol{F}$, associated with the reference (Lagrangian) state, and the left Cauchy-Green deformation tensor $\boldsymbol{b} = \boldsymbol{F}\boldsymbol{F}^{\boldsymbol{T}}$, associated with the current (Eulerian) state. The isotropic component of the strain-energy function can be fully expressed by the strain invariants of $\boldsymbol{C}$ (or equivalently of $\boldsymbol{b}$), which are:

$$\begin{aligned} I_1 &= tr(\boldsymbol{C}) \\ I_2 &= \tfrac{1}{2}(tr(\boldsymbol{C})^2 - tr(\boldsymbol{C}^2)) \\ I_3 &= \det(\boldsymbol{C}) = J^2 \end{aligned} \tag{3.2}$$

For a fibrous tissue like skin, the splay in orientation of the collagen fiber network has a notable influence on the anisotropy of the material [13,114,140]. The arrangement of the fibers in the dermis can be approximated by defining n_f fiber families where each one follows a distinct principal alignment, equivalent to a peak in the orientation distribution profile. Let $\boldsymbol{n}_{0i}\,(i = 1.\ .n_f)$ be the unit vector describing the main direction of fiber family i in the reference configuration. Accordingly, we define the structural tensors $\boldsymbol{B}_{0i}$ as:

$$B_{0i} = n_{0i} \otimes\ n_{0i}\ \ (i = 1.\ .n_f) \tag{3.3}$$

For each fiber family, two additional deformation invariants can be introduced

$$\begin{aligned} I_{4i} &= \boldsymbol{C}\colon \boldsymbol{B}_{0\boldsymbol{i}} = \lambda_i^2 \\ I_{5i} &= \boldsymbol{C}^2\colon \boldsymbol{B}_{0\boldsymbol{i}} \end{aligned} \tag{3.4}$$

λ_i denotes the stretch of the fibers oriented along $\boldsymbol{n}_{0i}$. For most semi-structural models presented below, it is the principal invariant that is used to characterize the contribution of the fibers to the deformation process. Other invariants associated with the relative interaction between the fiber families can be introduced, but these are generally neglected, either directly or by assuming material orthotropy or transverse anisotropy [9,141,142]. Tissue orthotropy is obtained when the principal material directions are orthogonal to each other, limiting the number of fiber families to three. For two fiber families (planar orthotropy), the normal to the plane formed by these two directions is also a preferred direction. Transverse isotropy is a special case of orthotropy, with only one principal fiber direction.

For dispersed fiber models, deviation around the principal orientation axis is incorporated, either by choosing a probability distribution function for the angular integration (AI) models, or by defining a set of generalized structure tensors for each fiber family for GST models. These concepts are further developed in the sections below, but an important notion is that this framework affects the expression of the deformation invariants associated with fiber deformation. For the sake of generality, the notations I_{4i} and I_{5i} are maintained in this subsection.

Following [114], the strain-energy function W of a fibrous biological tissue can be decomposed into an isotropic component, attributed to the ground substance, and the contribution of the fibers, such that:

$$W = W_m(\boldsymbol{C}) + \sum_{i=1}^{n_f} W_{fi}(\boldsymbol{C}, I_{4i}, I_{5i}) \tag{3.5}$$

where n_f is the number of distinct fiber families in the model. The second Piola-Kirchhoff stress tensor $\boldsymbol{S}$, associated with the reference configuration, can be obtained by derivation of the strain-energy function W:

$$\boldsymbol{S} = 2\sum_{j=1}^{n_{inv}} \frac{\partial W}{\partial I_j}\frac{\partial I_j}{\partial \boldsymbol{C}} \tag{3.6}$$

With n_{inv} the total number of invariants considered in the model. The Cauchy stress tensor $\boldsymbol{\sigma}$, associated with the current state, is obtained by push-forward operation from the reference state [142]:

$$\boldsymbol{\sigma} = \frac{1}{J}\boldsymbol{F}^{\boldsymbol{T}}\boldsymbol{S}\boldsymbol{F} = \frac{2}{J}\left[\sum\nolimits_{j=1}^{n_{inv}} \frac{\partial W}{\partial I_j}\boldsymbol{F}^{\boldsymbol{T}}\frac{\partial I_j}{\partial \boldsymbol{C}}\boldsymbol{F}\right] \tag{3.7}$$

In the following sections, some semi-structural and dispersed fiber models that have been implemented to represent the nonlinear elastic response of skin are presented, and the corresponding strain-energy function is provided.

3.2. Semi-structural models

3.2.1. The Arruda-Boyce eight-chain model

The Arruda-Boyce constitutive equation [143], also referred to as the eight-chain model, was initially introduced to mimic the behavior of rubber-like elastomers at high levels of strain, based on the entropy change upon stretching of macromolecules. The isotropic formulation is based on a cubic Representative Volume Element (RVE) consisting of eight freely-jointed chains starting from each corner and joining at the center. The initial length of each chain can be described by random walk: $r_0 = l\sqrt{N}$, with N the number of segments in the chain and l their length. The length of a fully extended chain is given by $r_L = Nl$, thus a "locking" stretch can be defined as:

$$\lambda_{lock} = \frac{r_L}{r_0} = \sqrt{N} \tag{3.8}$$

One can also express the stretch of a single chain: $\lambda_{chain} = \sqrt{I_1/3}$. The energy density function of such a system, with the hypothesis of material incompressibility, is the following:

$$W(\lambda_{chain}) = nk_B\Theta\left[\lambda_{lock}\lambda_{chain}\beta - \lambda_{lock}^2 \ln\left(\frac{sinh\beta}{\beta}\right)\right] \tag{3.9}$$

where n is the chain density, k_B the Boltzmann constant, Θ the absolute temperature and β is the inverse of the Langevin function: $\beta = \mathcal{L}^{-1}(\lambda_{chain}/\lambda_{lock})$, and $\mathcal{L}(\beta) = \coth\beta - 1/\beta$. The Arruda-Boyce model solely requires the identification of two parameters, the chain density n and the number of segments per chain N, which can potentially add physical meaning to the description.

In the context of skin mechanics, Bischoff et al. [144] implemented the isotropic Arruda-Boyce model to match experimental data reported in other studies [145-147]. The model has been shown to work particularly well at high strains. Interestingly, the anisotropic behavior of skin was also successfully captured by introducing an anisotropic stress-state, i.e. pre-existing stretches on the RVE.

The freely-jointed chain representation in the Arruda-Boyce model can also be replaced by a wormlike chain (WLC) model [110,111], which has a smoother curvature, and is therefore potentially better suited to mimic collagen in skin. In this case, the strain-energy function becomes:

$$W_{WLC} = \frac{k_B\Theta r_L}{4L_p}\left(2\left(\frac{\lambda_{chain}}{\lambda_{lock}}\right)^2 + \frac{1}{(1-\lambda_{chain}/\lambda_{lock})} - \frac{\lambda_{chain}}{\lambda_{lock}}\right) \tag{3.10}$$

Here L_p is the persistence length of a chain, i.e. its inherent stiffness.

The WLC model was implemented by Kuhl et al. [111] to simulate biaxial testing experiments conducted by Lanir and Fung [41] on rabbit skin, with the addition of transverse isotropy via a parallelepiped RVE with dimensions (a, b), and the effects of a surrounding matrix. The total energy density function of the tissue then becomes:

$$W_{Kuhl} = W_{bulk} + \gamma_{chain}(W_{WLC} + W_{rep}) \tag{3.11}$$

where W_{bulk} accounts for bulk effects due to the incompressibility of the matrix, γ_{chain} is the chain density per unit of length, and W_{rep} is a repulsive energy that ensures a stress-free reference configuration, and prevents the chains from collapsing. Their expressions are as follows:

$$\begin{aligned} W_{bulk}(I_1, I_3) &= \kappa\left[I_1 - 3 + \tfrac{1}{\beta}(I_3^{-\beta} - 1)\right] \\ W_{rep} &= \tfrac{k_B\Theta}{4L_p}\left(\tfrac{1}{r_L} + \tfrac{1}{4r_0(1-\lambda_{lock}^{-1})^2} - \tfrac{1}{4r_0}\right)\bar{W}_{rep}(I_1, I_4) \end{aligned} \tag{3.12}$$

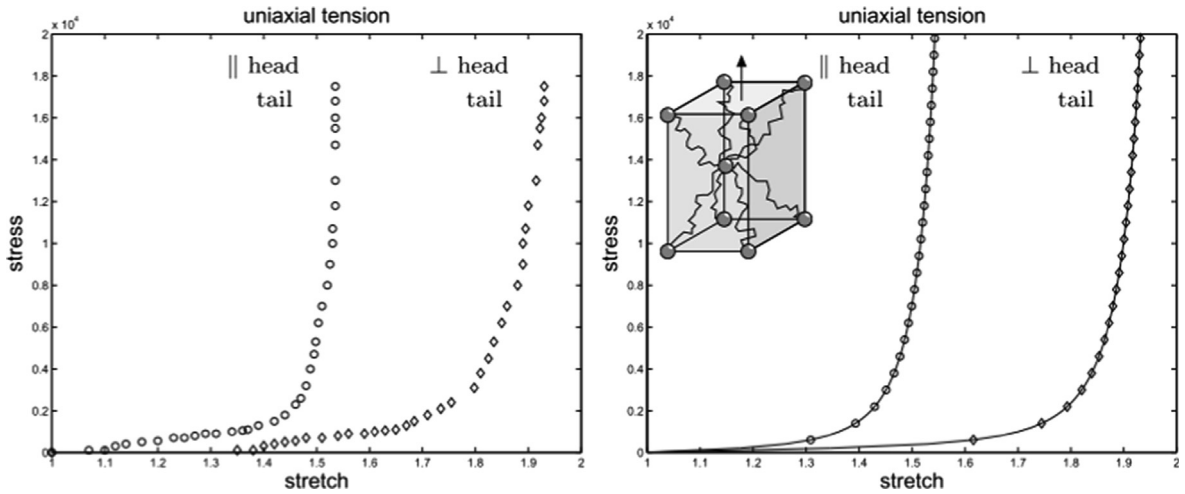

Fig. 3.2. Anisotropy of rabbit skin. Left: Experimental results from biaxial tensile tests reported by Lanir and Fung [41]. Right: Simulation with a transversely isotropic eight-chain model using a worm-like chain description, by Kuhl et al. [111]. The model captures adequately the anisotropy of skin, as well as the curve shape.

where $\bar{W}_{rep}(I_1, I_4)$ is a repulsion weighing factor characterized by the geometry of the representative volume element (RVE). Note that W_{bulk} has a form close to the neo-Hookean formulation. In this representation, the direction n_0 of transverse isotropy is the normal to the square section of the RVE with sides b. I_4 is therefore the square of the stretch along the a-direction, and is not related to fiber stretch. The current fiber length is $r = \sqrt{I_4 a^2 + (I_1 - I_4)b^2}$. Thus, material parameters are the bulk modulus κ, the bulk parameter β, the persistence length L_p, the chain density γ_{chain}, the contour length r_L, and the dimensions of the parallelepiped RVE (a, b). Fig. 3.2 shows that, after parameter identification, the transversely isotropic eight-chain model nicely captures the tissue's anisotropy and the J-curve elastic behavior. This framework can also be extended to material orthotropy by defining an RVE with three different lengths (a, b, c), as in the rheological model proposed by Bischoff et al. [148] to incorporate viscoelastic effects in skin, presented in Section 3.4.2.

The eight-chain model is a simple yet efficient way to represent a fibrous material. Some physical aspects can be integrated by assimilating the deformation of the chain with the straightening process of collagen fibers in the dermis, and the fiber arrangement is tridimensional, i.e. angular orientations in planes parallel and orthogonal to the dermis surface can be described. However, it can be challenging to physically interpret the nature of the attachment points at the center and in the corners of the RVE, and fiber volume fraction is quite limited. Nonetheless, it offers interesting perspectives for synthetic material design that would replicate the behavior of skin tissue, with characteristics resembling truss-lattice architectures, see for example [149].

3.3. Semi-structural models with discrete fiber distributions

3.3.1. The Weiss-Groves model

Weiss et al. [150] proposed a transversely anisotropic hyperelastic model of collagenous tissues for the description of ligaments, accounting for the uncrimping process of collagen fibers. This formulation was later adapted for skin by Groves et al. [37], in an attempt to fit their data on uniaxial tensile tests on human and murine skin. In their model, three fiber families with distinct orientations are considered, and the out-of-plane direction is restricted. The strain-energy function is decomposed into the contribution of the matrix, represented by a Veronda-Westmann model, a volumetric component, and the contribution of the fibers, such that: $W_{Weiss} = W_{VW}(I_1, I_2) + W_{vol}(J) + \sum_{i=1}^{3} W_{fiber_i}(\lambda_i)$. More specifically, we have:

$$\begin{aligned} W_{VW}(I_1, I_2) &= C_1(e^{C_2(I_1-3)} - 1) - \tfrac{C_1 C_2}{2}(I_2 - 3) \\ W_{vol}(J) &= \tfrac{K}{2}(\ln J)^2 \end{aligned} \tag{3.13}$$

For each fiber direction, the deformation depends on the fiber stretch λ_i, with $\lambda_i = \sqrt{I_{4i}}$:

$$\frac{\partial W_{fiber_i}(\lambda_i)}{\partial \lambda_i} = \frac{1}{\lambda_i}\begin{cases} 0, \lambda_i \le 1 \\ c_3[e^{c_4(\lambda_i - 1)} - 1], 1 \le \lambda_i \le \lambda_{lock} \\ c_5\lambda_i + c_6, \lambda_i \ge \lambda_{lock} \end{cases} \tag{3.14}$$

where λ_{lock} corresponds to the uncrimping stretch. Fibers are not given any compressive resistance, and the straightening process is described by an exponential function. Once fully uncrimped, their behavior becomes linear elastic. Thus, fiber geometry, which dictates the process of deformation, is taken into account by associating different elasticity functions for different stretching states, in a piecewise fashion. The Weiss-Groves model requires initially the identification of fifteen parameters, which can be reduced to six if all three fiber families share the same properties.

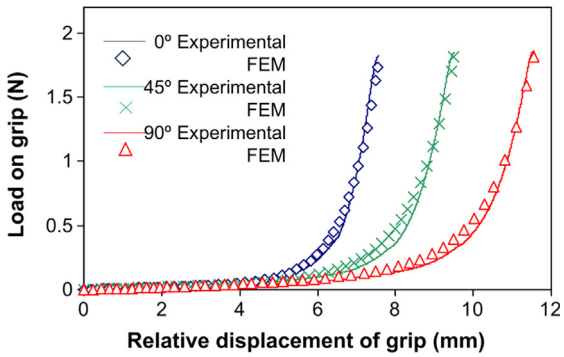

Fig. 3.3. Load-displacement curve of a circular human skin sample from mastectomy, tested in three different orientations. Experimental measurements and FEM calculations. Tests were interrupted at a low load and relaxed for 30 s between each measurement to avoid irreversible deformations when changing orientations. Reprinted from Groves et al. [37].

Groves et al. [37] obtained parameters with a very good consistency, both for human and murine skin, despite a high inter-sample variability. The model was able to accurately reproduce skin anisotropy, with a lowest R-square coefficient of 98.4%. An example for human skin is shown in Fig. 3.3. The piecewise function allows for a good description of the transition from the low-load regime in the toe region and the heel region to the linear portion of the J-curve. Hence, the Weiss-Groves model is an interesting approach for the comparison of specific areas of the deformation curve. The authors showed for example that main differences between samples from the same species is the degree of anisotropy (angular distribution), while differences between human and murine skin are seen with a shorter toe region for the latter. They attributed these differences mainly to the fiber network, the matrix conserving similar material properties.

It is important to observe that such a representation of skin suggests a layered arrangement of collagen fibers, parallel to the outer surface of the dermis. The model is therefore only transversely isotropic at the level of a single layer. Potential interactions between the three fiber families, which are generally not orthogonal to each other, are not considered. Moreover, the absence of an out-of-plane fiber component is in contradiction with several experimental observations, showing that the collagen network is initially tridimensional [12,13]. While this description may provide satisfying predictions of in-plane deformations, it may face difficulties with data from compressive or shear tests.

3.3.2. The Limbert model

The model proposed by Limbert [110] is the first to explicitly incorporate the contribution of inter-fiber and fiber-matrix shear into the deformation process of skin, although it can also be found in works on tendon by Szczesny and Elliott [151], Gao et al. [152] for the epimysium of skeletal muscles, and Peng et al. [153] for the annulus fibrosis. The formulation is based on the transversely isotropic model described by Lu and Zhang [154], who proposed a decoupling of the transformation gradient into volumetric, deviatoric, and shear components. In several other constitutive models, the shear energy is captured by the matrix/isotropic component but does not account for the influence of fiber deformation on the shearing interaction and does not make any distinction between shear occurring in the direction of local transverse anisotropy and the plane perpendicular to it. Considering an initial configuration where collagen fibers are wavy and follow different orientations, it is reasonable to assume that the interaction with the surrounding substance, or with other fibers, changes as the fibers stretch and realign.

In the Limbert model, a pair of orthogonal fiber families is embedded in a compressible matrix. The strain energy function is obtained by summation of each contribution:

$$W_{Limbert} = W_{vol}(J) + \sum_{i=1}^{2} W^i_{dev}(\bar{\lambda}_i) + W^i_1(\alpha_{i1}) + W^i_2(\alpha_{i2}, \bar{\lambda}_i) \tag{3.15}$$

with $\bar{\lambda}_i = J^{-\frac{1}{3}}\sqrt{I_{4i}}$ the deviatoric stretch (without loss of volume) of fiber family i, and:

$$\begin{aligned} \alpha_{i1} &= \frac{I_1 I_{4i} - I_{5i}}{\sqrt{I_3 I_{4i}}} \\ \alpha_{i2} &= \frac{I_{5i}}{I_{4i}^2} \end{aligned} \tag{3.16}$$

are invariants associated with transverse shear (perpendicular to the direction of local transverse anisotropy) and in-plane shear (i.e. the plane containing fiber family i), respectively. The total set of invariants is obtained by orthogonal decomposition of the stress tensor into hydrostatic pressure, deviatoric fiber tension, and in-plane and out-of-plane shear, and by identifying the strain invariants that directly yield this decomposition after differentiation of the strain-energy function. A detailed demonstration is provided in [154].

The volumetric component is defined as follows:

$$W_{vol}(J) = \frac{1}{4}\kappa(J^2 - 2lnJ - 1) \tag{3.17}$$

for which κ is the bulk modulus of the matrix. The deviatoric strain-energy associated with fiber stretch in family i is defined by:

$$W_{dev}^{i}(\bar{\lambda}_i) = \begin{cases} n_i\mu_{0i}\left(\bar{\lambda}_i^{\,2} + \frac{2}{\bar{\lambda}_i} - 3\right) + \xi_{i0}n_i ln(\bar{\lambda}_i^{-r_{0i}^2}),\ if \bar{\lambda}_i \le 1 \\ n_i k_B\theta\frac{L_i}{4L_{pi}}\left(2\frac{\bar{\lambda}_i^2 r_{0i}^2}{L_i^2} + \left(1 - \frac{\bar{\lambda}_i r_{0i}}{L_i}\right)^{-1} - \frac{\bar{\lambda}_i r_{0i}}{L_i}\right) + \xi_{i0}n_i ln(\bar{\lambda}_i^{-r_{0i}^2}),\ if \bar{\lambda}_i \ge 1 \end{cases} \tag{3.18}$$

Each fiber family is therefore considered as a set of polymer chains, of density per unit volume n_i, and described by the Worm-Like Chain constitutive law in tension, with initial end-to-end length r_{0i}, contour length L_i, and persistence length L_{pi}. Note that this formulation associates a non-null stiffness to fibers in compression, using a neo-Hookean behavior, with shear moduli μ_{0i}. The last term in each loading case corresponds to a repulsion energy that ensures that the chain does not collapse onto itself, similarly to the model of Kuhl et al. [111].

$W_1^i(\alpha_{1i})$ corresponds to the isotropic shear energy, effective in a plane transverse to the direction of family i, to which a shear modulus μ_{i1} is associated:

$$W_1^i(\alpha_{i1}) = \frac{\mu_{i1}}{2}(\alpha_{i1} - 2) \tag{3.19}$$

$W_2^i(\alpha_{i2}, \bar{\lambda}_i)$ corresponds to an anisotropic shear energy associated with the fiber-fiber and fiber-matrix interactions, along the direction of transverse anisotropy:

$$W_2^i(\alpha_{i2}, \bar{\lambda}_i) = \frac{\mu_{i2}}{2}(\alpha_{i2} - 1)^2\frac{1}{1 + a_i e^{-b_i(\bar{\lambda}_i - \bar{\lambda}_i^c)}} \tag{3.20}$$

The left part of Eq. (3.20) describes a classical one dimensional shear energy, while the right term is a sigmoid function, implemented to adjust the interaction energy for different stretching states [110]. A suggested justification for this behavior is that when adjacent fibers are stretching, the stiffness of their cross-links tends to increase, and therefore the shearing constraint is affected as well [153,155].

The Limbert model initially requires the identification of 23 physical parameters. The authors point out that the parameter set can be reduced by pre-injecting some of these parameters *ab initio* from structural measurements and microscale experimental characterizations. It is the approach that was chosen by Limbert [110] to validate the model, using data from biaxial tests of rabbit skin by Lanir and Fung [41], as shown in Fig. 3.4. The fiber families are considered to be aligned with both tensile directions (parallel and perpendicular to the Langer lines), and parameter identification is possible because no inter-laminar shearing is taken into account. The compressive behavior was neglected, both fiber families were considered to have the same elastic properties, and parameters (n_{0i}, a_i, b_i, $\bar{\lambda}_i^c$) were initially injected, either from the literature or by adjusting the sigmoid function to the J-curve region shifts. This data, as well as other calculated parameters, are reported in Table 3.1.

The constitutive framework proposed by Limbert et al. results in a notoriously large number of parameters, and although the authors suggest that it can be reduced by pre-setting some of them based on prior knowledge of the structural arrangement, physical properties of the components, or adjustments with respect to the experimental J-curve, several problems can arise. First, convexity of the strain-energy potential must be addressed with care [113,141]; with such a large parameter range, uniqueness of a solution that

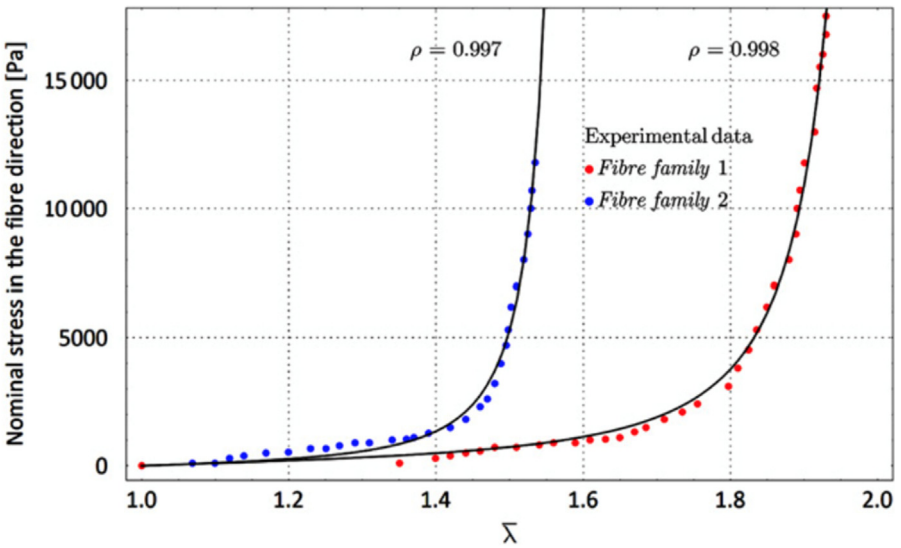

Fig. 3.4. Simulations using the Limbert model to match experimental data from biaxial tests on rabbit skin, performed in directions perpendicular (fiber family 1) and parallel (fiber family 2) to the Langer lines, reported by Lanir and Fung [41]. High correlation coefficients are found for both orientations. From Limbert [110].

Table 3.1
Values identified with the Limbert model applied on the biaxial tests on rabbit skin reported by Lanir and Fung [41]. Fiber family 1 is aligned across the Langer lines, and family 2 is aligned along the Langer lines. Parameters that were computed are marked in bold.

Parameter		Value
Bulk modulus of the matrix	κ	50 kPa
Sigmoid function parameter 1	a	50
Sigmoid function parameter 2	b	20
Sigmoid function locking stretch for fiber family 1	$\bar{\lambda}_1^c$	1.15
Sigmoid function locking stretch for fiber family 2	$\bar{\lambda}_2^c$	1.40
Chain density	n_{0i}	$7 \cdot 10^{21}$ m^{-3}
Tropocollagen (Type I) contour length	L_i	309 nm
Transverse shear modulus	$\boldsymbol{\mu_{i1}}$	**150.123 Pa**
Fiber-fiber/fiber-matrix shear modulus	$\boldsymbol{\mu_{i2}}$	**9.981 Pa**
Collagen persistence length for fiber family 1	$\boldsymbol{L_{p1}}$	**22 nm**
Initial length of crimped collagen for fiber family 1	$\boldsymbol{r_{01}}$	**155 nm**
Collagen persistence length for fiber family 2	$\boldsymbol{L_{p2}}$	**65 nm**
Initial length of crimped collagen for fiber family 2	$\boldsymbol{r_{02}}$	**198 nm**

minimizes the optimization problem cannot be guaranteed. This can be attenuated by restricting each parameter to a value within a physically realistic range; however, this may not be sufficient, as our current knowledge of the structure-mechanics relationship of the constituents of skin is rather limited, and different initial guesses on the parameter values may easily lead to different solutions. This statement is also relevant to other structural models with a large parameter set to identify. Secondly, the model presupposes that the family of fibers are aligned with both tensile directions from Lanir and Fung's experiment, attributing transitions in the tensile J-curve solely to the fiber straightening process. Fiber reorientation is not considered as a participating process in the nonlinear response of the tissue. Moreover, the worm-like chain model is essentially phenomenological, thus relating the parameters of the model with physical quantities reported elsewhere may offer limited perspectives. The other calculated moduli are also difficult to relate with any physical entity of the structure, or a microstructurally based interaction. Further analyses, such as molecular dynamics of interacting collagen chains, *in situ* microscopic characterization, and a better knowledge of the structural arrangement of the building components of skin, could be conducted to inform the model. Nonetheless, an equivalent Young's modulus was identified for collagen fibers, using $E_{ci} = 4L_{pi}k_B\theta/(\pi R^4)$ and assuming that the chain is contained within a cylindrical volume of radius R. Using calculated parameters for fiber families 1 and 2 (see Table 3.1), one can find 293 MPa and 865 MPa, respectively, which falls within an acceptable range.

The semi-structural models of skin presented above commonly consist of a superposition of the contributions of the ground substance and the fiber families, oriented along a discrete, limited number of directions. Tissue anisotropy is therefore attributed to the arrangement of collagen fiber families, and structural parameters, such as fiber crimp, can be implemented to describe the nonlinear elastic response of skin. Still, the distinct models that are used to represent each component remain phenomenological, and they do not necessarily provide an accurate description of the microscale processes occurring in the tissue. Fiber alignment is often limited to two or three principal directions, and the out-of-plane component is often neglected, except in the anisotropic eight-chain model. A structurally-based model of fibrous tissue yields physically relevant parameters only if the description of the fiber network is well informed with structural data [114], which is generally obtained from microscopy imaging. For skin, this implies that fiber splay and the tridimensional interweaving of the collagen network should be included in the constitutive framework.

3.4. Distributed fiber models of skin with fiber dispersion

Ex situ Transmission Electron Micrographs of pig skin, taken parallel to the outer surface of the dermis, show that in the initial configuration (Fig. 2.11a) collagen fibers are wavy and oriented in varying directions, forming a three-dimensional lattice. Fiber orientations are distributed along preferred directions, described by the Langer lines [13,69]; however, some degree of dispersion around these principal orientations is observed [140,156]. After application of tensile loads (Fig. 2.11b), this configuration is replaced by straightened fibers aligned closer to the tensile direction. The fibrils show a waviness with a reduced wavelength which is thought to be due to shrinking after fracture. It has been the goal of physically-based constitutive models of skin to incorporate these processes, namely gradual realignment of fibers and straightening. It is the coupled contribution of these processes that results in the nonlinear response of the material [40]. We present here the two main approaches used to incorporate fiber dispersion in the constitutive modeling of skin: angular integration (AI) and via generalized structural tensors (GST). The Lanir model and the Gasser-Ogden-Holzapfel model are introduced as examples for each approach. A more detailed classification of dispersed fiber models of soft collagenous tissues is reported by Holzapfel et al. [157].

3.4.1. An example of the angular integration approach: The Lanir model

Perhaps the first structurally-based constitutive model for soft collagenous tissues, the model introduced by Lanir in 1983 [158] is also one of the few that takes into account the contribution of elastin to the total deformation of the tissue. The model is based on a

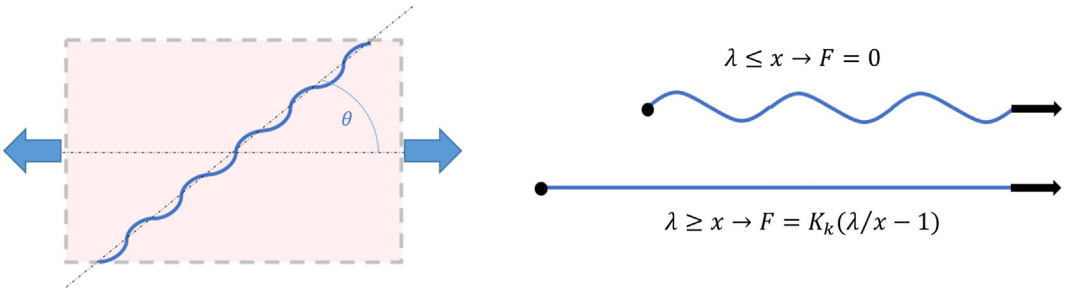

Fig. 3.5. Left: Schematic illustration of a crimped collagen fiber in a rectangular RVE, oriented by an angle θ with the principal direction. In the Lanir model, fiber orientations follow a $R_k(\theta)$ distribution. Right: Illustration of the straightening model of a collagen fiber. When the stretch is below a locking value x, no load is needed to straighten it. When fully uncrimped, the fiber follows a linear elastic law.

Representative Volume Element (RVE) consisting of an isotropic ground substance, modeled by a neo-Hookean function, a fraction ϕ_c of collagen and ϕ_e of elastin.

$$W_{Lanir} = (1 - \phi_c - \phi_e)\frac{\mu}{2}(I_1 - 3) + \phi_c W_c(\lambda) + \phi_e W_e(\lambda) \tag{3.21}$$

Each fiber is oriented at an angle θ with a chosen principal direction and these orientations follow a statistical distribution $R_k(\theta)$; $(k = \{c, e\})$. The schematic illustrations in Fig. 3.5 describe the corresponding RVE and the straightening process. It is assumed that collagen fibers are crimped and follow a one-dimensional linear elastic behavior only when unfolded; they buckle under compressive loads and no load is required to fully straighten them. The strain in the fiber is purely uniaxial. Elastin is already straight and linear elastic as well.

For collagen, the locking stretch x also follows a probability distribution function $D_c(x)$, implying that not all fibers follow the same geometry and curvature, and therefore a different stretch is required to fully straighten them. The energy density function of a given fiber type is then defined by integration of the elastic energy over the angular and locking distributions:

$$\begin{aligned} W_c(\lambda) &= \int_0^{\pi} \mathcal{R}_c(\theta) \int_1^{\lambda(\theta)} D_c(x)\frac{K_c}{2}\left(\frac{\lambda(\theta)}{x} - 1\right)^2 dx d\theta \\ W_e(\lambda) &= \int_0^{\pi} \mathcal{R}_e(\theta)\frac{K_e}{2}(\lambda(\theta) - 1)^2 d\theta \end{aligned} \tag{3.22}$$

where K_k is the stiffness of fiber type k and $\lambda(\theta)$ is the stretch in the direction of the fiber. Thus, numerical integration is required in the Lanir model. In its early formulation, Lanir [158] opted for normally distributed orientations restricted to a two-dimensional plane, and locking stretches for collagen, and a uniform distribution for straight elastin fibers. In an extended version of the same model proposed by Lokshin and Lanir [159] for uniaxial tests on rat skin, it was considered that solely fibers aligned parallel to the tensile direction contribute to the deformation process. Fiber realignment was neglected, and the influence of the matrix hydrostatic pressure on fiber rotation as well. Hence, fibers that are not aligned with the tensile direction are either undergoing compression or are not fully stretched, and therefore withstand no load. For fiber uncrimping, a beta distribution was chosen for the locking stretch, because it can be integrated over a finite interval and it can be asymmetric. Their nonlinear elastic formulation was paired with a Quasi-Linear Viscoelastic (QLV) model to study time-dependent processes, which will be described in the next section.

Modeling of skin's elasticity with the Lanir approach can be encountered in the works of Jor et al. [160] and Meijer et al. [161].

Table 3.2
Parameters of the Lanir model applied for skin in the works of Meijer et al. [161] and Jor et al. [160]. Values marked in bold indicate parameters that were identified by Finite Element Analysis (FEA) while other values were implemented *ab initio*, from data in the literature. N.A.: Not Applicable.

Reference	Meijer et al. [161]	Jor et al. [160]
Experimental Method	*In vivo* uniaxial stretching of human skin + Image tracking + FEA	*Ex vivo* biaxial stretching of porcine skin + Image tracking + FEA
Matrix Stiffness μ	None	**2.5 − 15.9 kPa**
Collagen Volume Fraction ϕ_c	0.3 [162]	0.3 [162]
Elastin Volume Fraction ϕ_e	0.02 [162]	None
Collagen Orientation $R_c(\theta)$	$1/\pi + C_1(\cos^4(\theta - C_2) - 0.375)$	π-periodic Von Mises Distribution $(\mu_\theta, \kappa_\theta)$
Elastin Orientation $R_e(\theta)$	Uniform Distribution $1/\pi$	N.A.
Collagen Undulation $D(x)$	Normal Distribution μ_x = **1.418 − 1.433**, σ_x = 0.2 [162]	Gaussian Distribution μ_x = **1.04 − 1.34**, σ_x = 0.2 [162]
Collagen Stiffness K_c	**50.9 − 85.7 MPa**	**48 − 366 MPa**
Elastin Stiffness K_e	1 MPa	N.A.

Their assumptions and findings are compared Table 3.2. In both studies, displacements on the surface of the skin were measured using image based point tracking, and a Finite Element Analysis mesh grid was superposed to identify a set of parameters for the Lanir model. In order to limit the amount of parameters to identify, and consequently save computational time, quantitative data from the literature is pre-injected into the model. Characterizations of the structural arrangements of collagen and elastin can indeed be useful to estimate their volume fraction, distribution, splay, and undulation. Jor et al. [160] chose to neglect the contribution of the elastin network, focusing primarily on the response at high strains of skin, while Meijer et al. [161] considered that the contribution of the matrix only takes place through hydrostatic pressure. Thus, parameter identification mainly focuses on collagen stiffness and mean undulation in each case.

Studies with experimental measurements on isolated collagen fibers report values from 30 MPa up to 1570 MPa for fiber stiffness [108] and of 1.2–1.6 for mean undulation (i.e. locking stretch) [162], which is in agreement with identified ranges in both studies. Computed collagen stiffness seem to fall closer to the lower bound of the experimental values, which could be attributed to the fact that, in the Lanir model, fiber-fiber and matrix-matrix sliding are ignored, although they might be a cause for tissue failure rather than failure of collagen itself. Moreover, these shearing interactions contribute also to the aggregation and realignment of fibers in the tensile direction.

Other models using the angular integration approach can be also encountered in the works of Tonge et al. [163] for skin, Freed et al. [164] and Driessen et al. [165] for cardiovascular tissues, and Federico and Gasser [166] for articular cartilage. Notable changes in the methods include two-dimensional or three-dimensional distributions, and different probability density functions (Gaussian [158,165], Beta [167], and Von Mises distributions [163,166], for example).

The angular integration approach accounts for fiber splay by introducing a probability density function as a continuous weighting factor for angular orientation [164]. Assuming an accurate estimation of collagen dispersion in the dermis, it is a rather elegant approach that introduces a relatively small number of additional parameters. A significant limitation of the AI approach is the considerable added computational cost, due to the fact that the integration needs to be performed for each point over the unit sphere [157,168].

3.4.2. The Gasser-Ogden-Holzapfel model: A GST approach

The Gasser-Ogden-Holzapfel (GOH) model [169] was first introduced to capture the deformation process of the arterial wall, an orthotropic soft tissue. Two main fiber families are considered, aligned with the material plane. For each fiber family, a generalized structure tensor $\boldsymbol{H_{0i}}$, is defined:

$$\boldsymbol{H_{0i}} = \kappa_i \boldsymbol{I} + (1 - 3\kappa_i)\boldsymbol{B_{0i}} \tag{3.23}$$

in which κ_i is the three-dimensional dispersion factor of family i, an integral of the probability distribution function of fiber orientations around the average direction over a unit sphere:

$$\kappa_i = \frac{1}{4}\int_0^{\pi} \rho_i(\theta)\sin^3\theta d\theta \tag{3.24}$$

where $\rho_i(\theta)$ is the assumed distribution of fiber family i. $\kappa_i = 0$ corresponds to a fiber family where all the fibers are perfectly aligned in the same direction, whereas for $\kappa_i = 1/3$ all directions are equiprobable (isotropic). Note also that non-symmetric or bimodal fiber distributions can be incorporated, which yields a slightly more complex form of $\boldsymbol{H_i}$ [114,157]. A planar dispersion can also be assumed, in which case:

$$\boldsymbol{H_{0i}} = \kappa_{i2D}\boldsymbol{I}_2 + (1 - 2\kappa_{i2D})\boldsymbol{B_{0i}} \tag{3.25}$$

where $\boldsymbol{I}_2$ is the two-dimensional identity tensor, in the plane of fiber alignment, and κ_{i2D} is the planar dispersion of fiber family i [157,163]. The energy density function was defined as follows:

$$W_{GOH} = \frac{\mu}{2}(I_1 - 3) + \sum_{i=1}^{2} \frac{k_{i1}}{2k_{i2}}[exp(k_{i2}(\boldsymbol{H_{0i}}\colon \boldsymbol{C} - 1)^2) - 1] \tag{3.26}$$

One can observe that the first term of Eq. (3.26) is the neo-Hookean behavior applied to describe the matrix, with shear modulus μ, while fiber stretching is described with exponential terms. k_{i1} and k_{i2} are material parameters proper to each fiber family. With dispersion factors κ_i; $i = (1, 2)$ and assuming a perpendicular arrangement of fiber families, this potentially results in eight parameters that need to be identified.

In the context of skin mechanics, Ní Annaidh et al. [69] implemented the GOH model with uniaxial tests of human samples. They used histological cross-sections of slides taken parallel to the epidermis and estimated the distribution of orientations of the collagen fibers. Straight collagen fiber segments were identified and are marked by black lines in Fig. 3.6. These lines tend to align with the horizontal direction. To simplify the approach and reduce the number of parameters, it was assumed that the two main fiber families are oriented symmetrically to the tensile direction and possess the same material properties. An orientation angle γ and the dispersion factor κ were determined and injected into the model. Thus, it is the first model introduced here where parameters are determined based on structural observations, instead of phenomenological ones. Very good agreement between experimental results and Finite Element Analysis calculations based on the GOH description were found, for tests performed along and across the Langer lines (see Fig. 3.6).

In a comparative analysis of models to simulate full field bulge tests on skin, Tonge et al. [163] compared a 3-D GOH, a 2-D GOH, and a fully integrated fiber (AI) models to match their experimental results. Their transversely isotropic 3D-GOH model assumes the

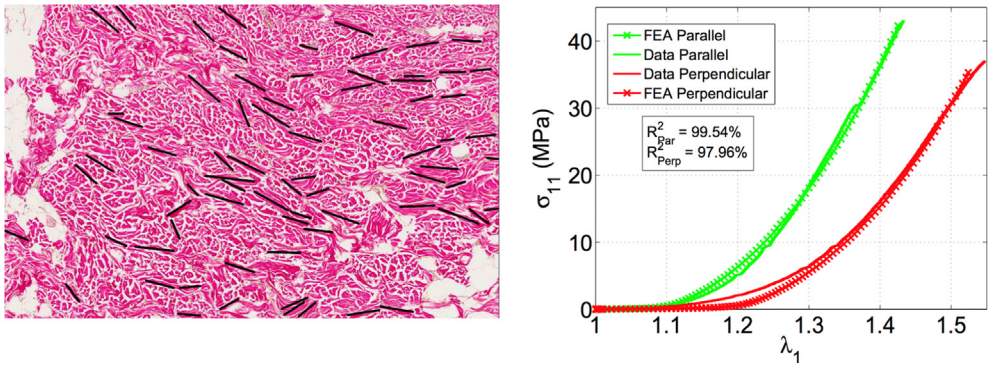

Fig. 3.6. Left: Manual segmentation of collagen from histology image. Elongated fibers are marked by black lines, their orientation is then measured manually to estimate the main orientation and the dispersion factor. Right: Comparison of experimental data from uniaxial tensile tests with simulations based on the GOH model for samples parallel (green) and perpendicular (red) to the Langer lines. From Ní Annaidh et al. [69]. (For interpretation of the references to color in this figure legend, the reader is referred to the web version of this article.)

existence of only one fiber family, with a three-dimensional dispersion vector, whereas for the 2D-GOH model the out-of-plane direction is restricted, which affects the structural tensor $\boldsymbol{H}$, as described in Eq. (3.25). The fully integrated (AI) model uses a Von Mises distribution and assumes a planar arrangement of fibers. In their conclusions, the authors observed that a three-dimensional distribution does not seem appropriate to represent the actual collagen fiber distribution in skin, and that both formulations of the GOH model have difficulties reflecting the anisotropy of the material, which was much more successful with the FI model. An advantage of the former formulation is that the energy density function presents a closed-form expression whereas the latter necessitates numerical integration. It is also relevant to point out that better results have been obtained with two fiber families instead of one, and that these observations are specific to the bulge tests reported in their study.

Buganza-Tepole et al. [170] used the GOH model for simulations of tissue expansion methods to identify the one that would minimize the concentration of stresses, which they associated with the likelihood of tissue necrosis. Their study is a remarkable illustration of the application of structural models to predict tissue behavior and consequently improve medical techniques.

The GST approach differs from the AI method mainly by the fact that the distribution of fiber orientations is directly averaged and incorporated into the structural tensors $\boldsymbol{H}_i$. This results in a superior computational efficiency, compared to AI, as the angular integration is only performed once [168]. However, a resulting limitation of this averaging method is that selectively attributing a different behavior for fibers undergoing compression or straightening is no longer possible, which does not reflect the real behavior of the tissue [114]. This is in agreement with the observations made by Tonge et al. [163] in their comparative analysis. Methods attempting to exclude compressed fibers in the generalized structure tensor, by either reducing the integration interval in the dispersion parameter, or introducing a Heaviside function in the strain-energy of the fibers, were reviewed by Holzpafel et al. in [114]. It is also not possible to consider a distributed fiber undulation, as it can be in the AI method.

Dispersed fiber models present an improvement in the representation of the collagen network, and the angular distribution of fibers can be quite accurately captured by a selected probability density function, with a reduced amount of added constitutive parameters. This implies that some prior information on fiber dispersion in the material is needed, whether it is assumed from general observations of the skin microstructure, or if it is directly measured on the tested sample. With higher structural accuracy, the deformation processes in the structure are more likely to reflect reality and the obtained parameters gain in physical relevance. Variations in these parameters can be then attributed to differences in tissue anisotropy (i.e. dispersion), fiber concentration, or crimp. However, these models do not take into account fiber-fiber interactions, such as the influence of inter-fiber cross-linking, which may play a role in fiber recruitment, tissue stiffening, or delamination before failure. The improved structural accuracy is also hindered by the added computational cost of angular integration. A compromise to this shortcoming was proposed by Flynn et al. [171], who suggested the use of a discretized weighted fiber distribution for collagen (with 6 principal fiber directions). A closed-form solution of the strain-energy function becomes possible, and distributed fiber undulation can be considered, as well as potential fiber-fiber interactions. Nonetheless, material anisotropy and continuous fiber realignment are less accurately captured with this approach, and the stress-stretch curve shows more pronounced transitions as fiber families get recruited.

Another aspect of skin mechanics that needs to be taken into consideration is viscoelasticity, as the nonlinear elastic formulations described so far do not include the influence time-dependent processes.

3.5. Modeling viscoelasticity

In tests such as stress-relaxation and creep, the viscoelastic behavior of skin is revealed and characterized by a response that changes with time and loading history. In loading-unloading tests, the hysteresis of the stress-strain curve also indicates a dissipative viscoelastic behavior. The strain rate sensitivity of the tissue is another example of this behavior. Hence, for a more complete description of the mechanical response of skin under different types of loads, it is important to consider the effect of time-dependent processes occurring in the material. In the case of soft fibrous tissues, viscoelastic effects are often decoupled from the elastic

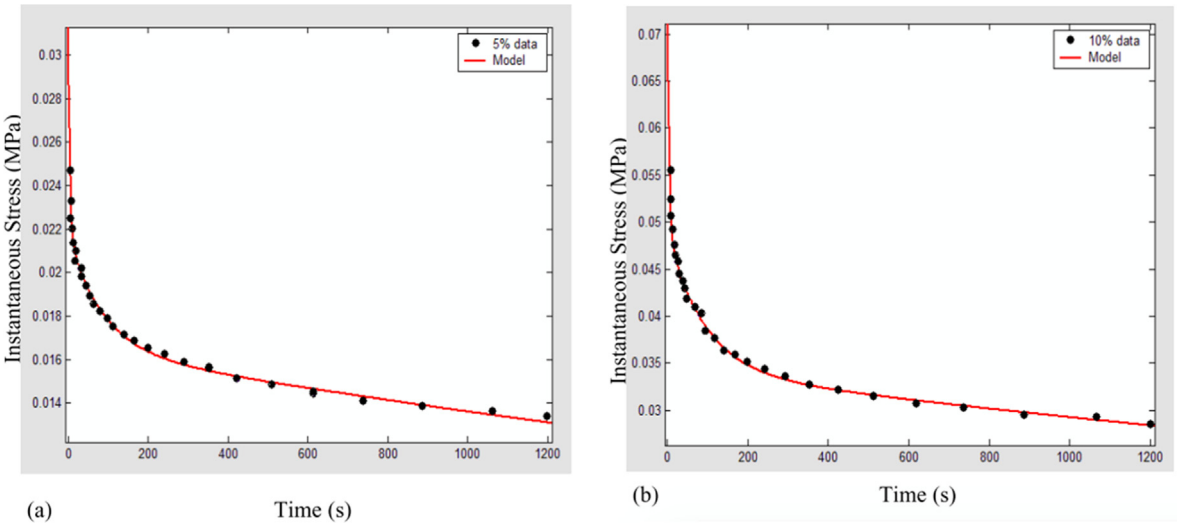

Fig. 3.7. Stress relaxation tests on swine skin, initiated at different strains (black dots). Because it encompasses the loading history, the QLV theory (red lines) fits very well both for cases. Adapted from Liu and Yeung [131]. (For interpretation of the references to color in this figure legend, the reader is referred to the web version of this article.)

contribution, and the total response of the material is obtained by superposition of the elastic and time-dependent processes.

3.5.1. *Quasi-linear viscoelastic theory (QLV)*

Fung [124] first proposed in 1967 to describe the stress-strain relationship of soft biological materials by linear decomposition of stresses into an elastic part and a history-dependent part, i.e. a viscoelastic component, in an integral form:

$$\sigma(t) = \int_0^t g(t-\tau)\frac{\partial \sigma_{el}(\tau)}{\partial \tau} d\tau \tag{3.27}$$

where $g(t)$ is the reduced relaxation function, and σ_{el} is the instantaneous elastic nominal stress. The elastic stress can be any nonlinear function chosen to describe tissue deformation. Eq. (3.27) contains a history-dependent component via the time integral and is essentially a convolution between the reduced relaxation $g(t)$ and the time derivative of the elastic component of the stress. Different forms for $g(t)$ can be encountered, including Prony series [10,66], exponential functions [72,131,159,172], logarithmic functions [173], and power law functions [174]. The QLV model generally offers good flexibility with a tunable quantity of descriptive parameters. Liu and Yeung [131] implemented an exponential stress-strain relationship and a sum of three decreasing exponentials for the relaxation function. Relaxation of swine skin, taken at different relaxation strains, was very well captured (see Fig. 3.7). Bischoff et al. [172] modeled porcine skin with QLV by coupling an orthotropic worm-like chain model and an exponential integral relaxation function, and found very satisfying results with only seven parameters. Stress relaxation and cyclic loading were well captured by the model. However, researchers highlight the lack of consistency of this approach, with different parameters identified for different loading conditions [172], and an inability to capture short-term viscoelastic phenomena, such as preconditioning or strain rate sensitivity [66].

3.5.2. *Differential viscoelastic models*

According to the *principle of fading memory* [9,175], recent deformations have a greater influence on the stress-state than those that happened in a distant past. Thus, one apparent limitation of the QLV approach is that the integral form captures the entire deformation history without any emphasis on recent events, an important consideration at high deformation speeds. Following this observation, Pioletti et al. [55] proposed a differential viscoelastic law for soft biological materials, based on the Clausius-Duhem inequality under isothermal conditions [176]:

$$\left(\boldsymbol{S} - 2\rho_0 \frac{\partial W_e}{\partial \boldsymbol{C}}\right) : \frac{\dot{\boldsymbol{C}}}{2} \geq 0 \tag{3.28}$$

where $\boldsymbol{S}$ is the second Piola-Kirchhoff stress tensor, $\boldsymbol{C}$ the right Cauchy-Green deformation tensor, $\dot{\boldsymbol{C}}$ its first time derivative, ρ_0 the initial material density, and W_e the elastic potential. For a viscoelastic material subject to energy dissipation, one can assume the existence of a viscoelastic potential W_v [55], such that:

$$\boldsymbol{S} = 2\rho_0 \frac{\partial W_e}{\partial \boldsymbol{C}} + 2\frac{\partial W_v}{\partial \dot{\boldsymbol{C}}} \tag{3.29}$$

The formulation detailed in Eq. (3.29) takes into account rate-dependency and enables the modeling of nonlinear viscoelastic

materials via the introduction of suitable elastic and viscoelastic potentials. Pioletti et al. [55] successfully modeled the strain-rate sensitivity of tendon and ligament using a Veronda and Westmann elastic potential [135] and the following viscous potential:

$$W_v = \frac{\eta}{4} tr\dot{\boldsymbol{C}}^2 (tr\boldsymbol{C} - 3) \tag{3.30}$$

with η as a viscosity factor. Very good consistency is obtained with a reduced number of parameters, although the assumption of an isotropic material is disputable. Limbert and Middleton [177] further extended this framework to transverse isotropy using tensors, and found as well good agreement with their experimental results.

3.5.3. Generalized Maxwell models and nonlinear extensions

A Generalized Maxwell Model is an arrangement in series or in parallel of viscous and elastic components, usually mimicking the microscale arrangement of constituents within the material. There are three common representations: the Maxwell, the Kelvin-Voigt, and the Standard models. Other Generalized Maxwell viscoelastic models can be formed by assembling, in series or in parallel, these three classic formulations, such as the Burgers model for example. At higher levels of complexity, it becomes more difficult to analytically solve governing stress-strain equations, and numerical solving needs to be performed. Each building block of the model can be used to represent a sub-unit or constituent of the tissue at a given hierarchical level. For example, Puxkandl et al. [178] proposed a model for collagen fibers in tendons consisting of two Kelvin-Voigt cells in series: one block to describe fibrils, and the other block for the surrounding proteoglycan matrix. This formulation was used to quantify effects of strain rate on the apparent viscosity of tendons. It is however less common to encounter Generalized Maxwell models used to represent the viscoelasticity of skin. The structural arrangement is more complex than in the case of tendons, where collagen fibers are mainly aligned with the direction of tension [172,178], and the standardized elastic block cannot capture the nonlinear behavior of skin in tension. Instead, linear strain and stress decomposition can be extended to nonlinear constitutive laws, both for the elastic components as well as the inelastic (viscous) ones. For example, Yang et al. [40] introduced a modified Maxwell model for skin using a polynomial function for the elastic constitutive equation between the external stress and elastic strain, to take into account the nonlinearity of the tissue. Another formulation for viscoelasticity, based on the Standard model, was proposed by Bergstrom and Boyce [179], and is presented in the following section.

3.5.4. Bergstrom-Boyce model

Bischoff et al. [148] implemented the Bergstrom-Boyce model for their modified rheological model of skin. Initially intended for the characterization of the viscoelastic properties of rubber-like elastomers, Bergstrom and Boyce's constitutive law [179] is based on the proposition that an elastomer can be modeled as two interacting networks of polymers, the first one capturing the elastic (or equilibrium) response of the material and the other one the time-dependent deviation from equilibrium, as earlier suggested by Roland [180]. This can be represented by a modified Standard Maxwell element (see Fig. 3.8). In this representation the total true stress is obtained by summation of the stress state in both components $T = T_A + T_B$. The deformation gradient in the same in both networks: $\boldsymbol{F} = \boldsymbol{F}_A = \boldsymbol{F}_B$. The purely elastic component A follows an orthotropic Arruda-Boyce model. For the sake of simplicity, it is described here for the isotropic case:

$$W_A = n_A k_B \Theta \left[\lambda_{lock_A} \lambda_{chain_A} \beta - \lambda_{lock_A}^2 ln\left(\frac{sinh\beta}{\beta} \right) \right] \tag{3.31}$$

The true stress-stretch relationship $T_A(\lambda_{chain\,A})$ is then obtained by derivation, where $\lambda_{chain_A} = \sqrt{tr(\boldsymbol{B}^*)/3}$ is the effective distortional stretch of chain A, and $\boldsymbol{B}^* = J^{-2/3}\boldsymbol{F}\boldsymbol{F}^{\boldsymbol{T}}$. For component B, the transformation gradient is decomposed into purely elastic and viscous components: $\boldsymbol{F_B} = \boldsymbol{F_B^{el}}\boldsymbol{F_B^{v}}$. The elastic block of component B is also described by the Arruda-Boyce model. The effective distortional elastic stretch in network B can be obtained by isolating the elastic contribution of the transformation gradient:

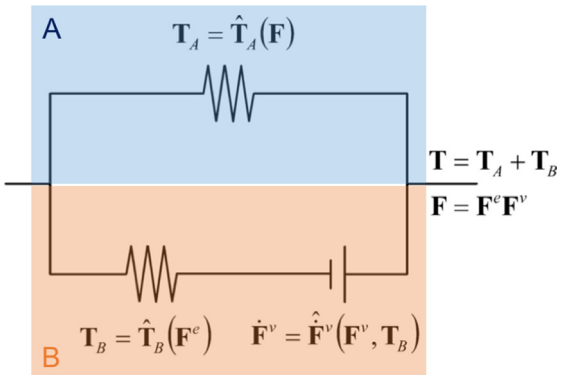

Fig. 3.8. Schematic description of the rheological model based on the Standard Maxwell model using the Bergstrom-Boyce formulation of viscoelasticity, implemented by Bischoff et al. [148] to capture the mechanical behavior of skin. Component A is purely elastic, component B contains a viscous part.

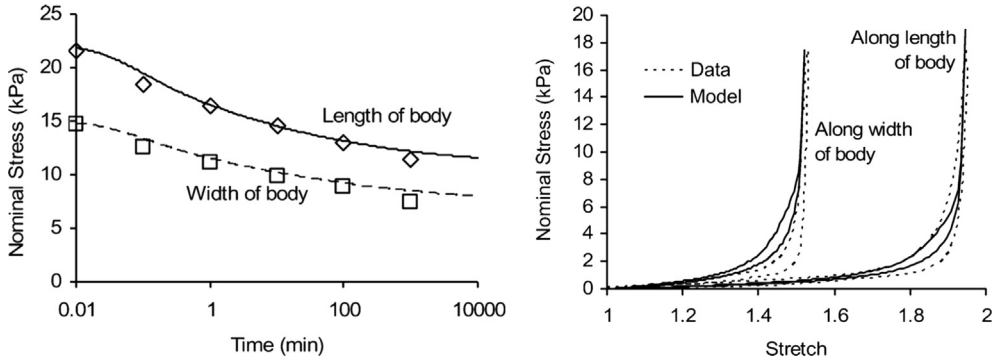

Fig. 3.9. Experimental data from planar biaxial tests on rabbit skin by Lanir and Fung [41], captured by the Bergstrom-Boyce model. Left: Stress relaxation done along the length and the width of the body (experiments – symbols; simulations - lines). Right: Loading/unloading tests conducted along the length and the width of the body (experiments – dashed lines; simulations – lines). From Bischoff et al. [148].

$\lambda_{chain_B}^{el} = \sqrt{tr(\boldsymbol{B}_B^{el*})/3}$, with $\boldsymbol{B}_B^{el*} = J_B^{el-2/3}\boldsymbol{F}_B^{el}\boldsymbol{F}_B^{elT}$, and $J_B^{el} = \det(\boldsymbol{F}_B^{el})$.

The velocity gradient of the viscous network is also defined $\boldsymbol{L}_B^{\nu} = \dot{\boldsymbol{F}}_B^{\nu}\boldsymbol{F}_B^{\nu-1}$ where the first term corresponds to the time derivative of the viscous deformation gradient tensor. In the absence of plastic spin [179], the velocity gradient becomes equal to the viscous rate of change $\boldsymbol{D}_B^{\nu}$, which, in the Bergstrom-Boyce framework, is constitutively prescribed by:

$$\boldsymbol{D}_B^{\nu} = \dot{\gamma}_{\nu}\frac{dev(\boldsymbol{T}_B)}{\|\boldsymbol{T}_B\|} \tag{3.32}$$

where $\dot{\gamma}_{\nu}$ is the effective deformation rate (or reptation coefficient), and $dev(\boldsymbol{T}_B)/\|\boldsymbol{T}_B\| = \boldsymbol{N}_{\nu}$ is a vector defining the direction of the stress driving the viscous deformation. The expression of $\dot{\gamma}_{\nu}$ is then based on the theory of reptation [148]:

$$\dot{\gamma}_B = \dot{\gamma}_0(\lambda_B^{\nu} - 1)^C\left(\frac{\|\boldsymbol{T}_B\|}{\tau}\right)^m \tag{3.33}$$

and $\dot{\gamma}_0$, C, τ, and m are material parameters, and $\lambda_B^{\nu} = \sqrt{tr(\boldsymbol{F}_B^{\nu}\boldsymbol{F}_B^{\nu T})/3}$. Hence, a relationship between $\boldsymbol{F}_B^{\nu}$ and the nominal stress tensor $\boldsymbol{T}_B$ can be obtained. By numerical integration, the total stress-stretch relationship can then be solved. Bischoff et al. [148] employed the orthotropic formulation of this method to fit the stress-relaxation and the loading-unloading curves from Lanir and Fung [41], performed biaxially in the two main orientations. Their results, reproduced in Fig. 3.9, show that the model can capture time-dependent processes quite well, with a consistent set of parameters. Inaccuracies could stem from the lack of knowledge of the tissue's real orientation, rather than from the model itself. A drawback of the Bergstrom-Boyce model is that, in order to capture viscoelasticity, 10 additional material parameters are involved. Moreover, the description developed in this constitutive framework does not take into consideration the real structure of the tissue, and the parameters involved are purely phenomenological. The freely-jointed chain model, used to describe fiber stretch, is not defined for values of λ above λ_{lock}, meaning that the fiber cannot stretch more than its maximal extended length. This poses substantial problems in terms of representation of the deformation sequence of collagen fibers in the dermis [40].

In order to provide a better description of the tissue structure, the approach used by Bischoff et al. [148] can adapted to a rheological framework with a matrix component and a fiber component in parallel, as suggested by Limbert [9]. The method described in the section above can then be applied to each component, where separate elastic and viscoelastic sub-components are introduced for each network. Note that for the elastic components, other models than the eight-chain function can be implemented.

The decomposition of the total deformation in an elastic and a viscoelastic component offers flexibility in terms of selecting separate constitutive behaviors for each contribution, including the ones listed above. Models for the viscoelastic component are generally simple and phenomenological, mainly to reduce the set of added parameters, but also because the physical time-dependent processes occurring in the tissue, such as internal reorganization of the microstructure, fluid flow, fiber sliding, and intrinsic component viscoelasticity, are still not fully understood and lack experimental characterization. Furthermore, said processes are believed to be the cause of other dissipative and loading history-dependent features of the mechanical behavior of skin, which should be taken into consideration and are developed in the next section.

3.6. Modeling the dissipative behavior of skin

In his book on the Mechanical Properties of Living Tissues, Fung [181] listed several physical features characteristic of soft biological tissues under uniaxial tension:

– The stress-strain relationship of the material is nonlinear,
– A hysteresis loop can be observed during loading-unloading tests,
– Stress relaxation occurs at constant strain,

– Preconditioning: with repeated loading cycles, the tissue reaches a steady-state, and the hysteresis loop reduces in width with each cycle,
– The stress relaxation at a fixed stress level reduces with repeated cycles,
– The hysteresis response is nearly independent of strain rate.

A number of these features are illustrated for skin in Section 2.4. To the authors' knowledge, experimental data on skin is lacking on the effect of strain rate on the hysteresis loop. Nonlinear elasticity is a well-known property of skin, and has been developed in detail in this review. Stress relaxation and hysteresis, to which creep and strain rate sensitivity can be added, reflect the viscoelastic behavior of the material, as discussed in the previous section. However, nonlinear elasticity and viscoelasticity are not sufficient to explain the last three material properties identified by Fung [181]. The preconditioning behavior, the displayed Mullins effect (see Section 2.4.9), and the existence of remnant strains after each loading-unloading cycle (see Fig. 2.20a) are clearly indicative that the loading history has an influence on the material response. This suggests that irreversible changes in the tissue have occurred, and that a new equilibrium state is being reached. These changes are believed to be caused by rearrangements of the microstructure during loading, and a redistribution of the internal fluids [133,182]. Interfibrillar cross-links may break and reform, affecting the resting configuration of the material. At larger strains, more pronounced irreversible processes take place: fiber sliding, delamination, and finally tissue failure are observed [40]. This is translated by a softening response of the material prior to failure.

The aforementioned phenomena are often neglected in constitutive models of skin, generally because the reference experiments are taken before failure and are limited to single uniaxial tests, one loading-unloading cycle, or normalized stress relaxation. Some models that incorporate these dissipative inelastic properties are presented in this section, with either a phenomenological approach or a semi-structural description of the processes at stake.

3.6.1. The Rubin-Bodner model

Rubin and Bodner [182] described in 2002 a formulation to model the dissipative response of soft tissue, based on phenomenological elastic-viscoplastic constitutive equations. Their objective was to fully address the physical features of soft biological tissues identified by Fung [181], with a three-dimensional model capturing material anisotropy. In the elastic-viscoplastic theory, history dependent state-variables are introduced and determined by evolution equations [182,183].

The current configuration of the material is taken at time t. The velocity gradient tensor $\boldsymbol{L}$ is introduced as time derivative operator of the deformation gradient $\boldsymbol{F}$:

$$\dot{\boldsymbol{F}} = \boldsymbol{L}\boldsymbol{F} \tag{3.34}$$

The rate of deformation tensor $\boldsymbol{D}$ is then expressed as the symmetric part of the velocity gradient:

$$\boldsymbol{D} = \frac{1}{2}(\boldsymbol{L} + \boldsymbol{L}^T) \tag{3.35}$$

In the presented continuum description, $\boldsymbol{D}$ effectively serves as a measure of the evolution of the deformation. It is convenient to separate the total deformation tensor $\boldsymbol{b}$ ($\boldsymbol{b} = \boldsymbol{F}\boldsymbol{F}^T$), into the dilatation $J = \det\boldsymbol{b}$ and a unimodular distortional component $\boldsymbol{b}^* = J^{-2/3}\boldsymbol{b}$. Since $\det\boldsymbol{b}^* = 1$, two independent invariants of $\boldsymbol{b}^*$ can be introduced:

$$\begin{aligned}\beta_1 &= \boldsymbol{b}^*\colon \boldsymbol{I}\\ \beta_2 &= \boldsymbol{b}^*\colon \boldsymbol{b}^*\end{aligned} \tag{3.36}$$

The time derivatives of J, $\boldsymbol{b}^*$, β_1, and β_2 are expressed via the evolution equations:

$$\begin{aligned}\dot{J} &= J\boldsymbol{D}\cdot\boldsymbol{I}\\ \dot{\boldsymbol{b}}^* &= \boldsymbol{L}\boldsymbol{b}^* + \boldsymbol{b}^*\boldsymbol{L}^T - 2/3(\boldsymbol{D}\colon \boldsymbol{I})\boldsymbol{b}^*\\ \dot{\beta}_1 &= 2[\boldsymbol{b}^* - 1/3(\boldsymbol{b}^*\colon \boldsymbol{I})\boldsymbol{I}]\colon \boldsymbol{D}\\ \dot{\beta}_2 &= 4[\boldsymbol{b}^{*2} - 1/3(\boldsymbol{b}^{*2}\colon \boldsymbol{I})\boldsymbol{I}]\colon \boldsymbol{D}\end{aligned} \tag{3.37}$$

Following the work of Rubin and Attia [184], a distortional tensor for the elastic part of the dissipative component is defined, by integration of the evolution equation:

$$\dot{\boldsymbol{b}}^*_{\boldsymbol{de}} = \boldsymbol{L}\boldsymbol{b}^*_{\boldsymbol{de}} + \boldsymbol{b}^*_{\boldsymbol{de}}\boldsymbol{L}^T - 2/3(\boldsymbol{D}\colon \boldsymbol{I})\boldsymbol{b}^*_{\boldsymbol{de}} - \Gamma\boldsymbol{A}_{\boldsymbol{d}} \tag{3.38}$$

in which $\Gamma\boldsymbol{A}_{\boldsymbol{d}}$ is a measure of the rate of inelastic deformation, with:

$$\boldsymbol{A}_{\boldsymbol{d}} = \boldsymbol{b}^*_{\boldsymbol{de}} - \left(\frac{3}{\boldsymbol{b}^{*-1}_{\boldsymbol{de}}\colon \boldsymbol{I}}\right)\boldsymbol{I} \tag{3.39}$$

And where $\Gamma$is a non-negative scalar function to be defined. Similarly, two independent invariants associated with the inelastic component can be introduced:

$$\begin{aligned}\alpha_1 &= \boldsymbol{b}^*_{\boldsymbol{de}}\colon \boldsymbol{I}\\ \alpha_2 &= \boldsymbol{b}^*_{\boldsymbol{de}}\colon \boldsymbol{b}^*_{\boldsymbol{de}}\end{aligned} \tag{3.40}$$

and their corresponding time derivatives are:

$$\dot{\alpha_1} = 2[\boldsymbol{b}^*_{\boldsymbol{de}} - 1/3(\boldsymbol{b}^*_{\boldsymbol{de}}\colon \boldsymbol{I})\boldsymbol{I}]\colon \boldsymbol{D} - \Gamma \boldsymbol{A_d}\colon \boldsymbol{I}$$
$$\dot{\alpha_2} = 4[\boldsymbol{b}^{*2}_{\boldsymbol{de}} - 1/3(\boldsymbol{b}^{*2}_{\boldsymbol{de}}\colon \boldsymbol{I})\boldsymbol{I}]\colon \boldsymbol{D} - \Gamma \boldsymbol{A_d}\colon \boldsymbol{b}^*_{\boldsymbol{de}} \tag{3.41}$$

The Rubin-Bodner model also includes a set of N fiber families, with a given orientation $\boldsymbol{n_{ti}}$ in the current configuration ($i = 1, 2, \cdots N$). The stretch of a fiber family is measured by λ_i. Their evolution equations are expressed as follows:

$$\dot{\lambda_i} = \frac{1}{\lambda_i}(n_{ti} \otimes \ n_{ti})\colon D \tag{3.42}$$

The strain-energy function of the material can therefore be defined as a function of the invariants: $W = W(J, \beta_1, \beta_2, \alpha_1, \alpha_2, \lambda_1, \cdots, \lambda_N)$.

The rate of material dissipation $\mathcal{D}$, based on the balance of entropy [182,184,185], is defined by:

$$\mathcal{D} = \boldsymbol{\sigma}\colon \boldsymbol{D} - \rho_0 \dot{W} \geq 0 \tag{3.43}$$

and is always zero or positive. Note that the equation above is equivalent to the Clausius-Duhem inequality introduced in Eq. (3.28). By decomposing the Cauchy stress into deviatoric and hydrostatic terms: $\boldsymbol{\sigma} = \boldsymbol{\sigma_{dev}} - p\boldsymbol{I}$, Eq. (3.43) becomes:

$$\boldsymbol{\sigma_{dev}}\colon \boldsymbol{D} - p\boldsymbol{I}\colon \boldsymbol{D}$$
$$- \rho\left(\frac{\partial W}{\partial J}J\boldsymbol{D}\colon \boldsymbol{I} + \frac{\partial W}{\partial \beta_1}\dot{\beta_1} + \frac{\partial W}{\partial \beta_2}\dot{\beta_2} + \frac{\partial W}{\partial \alpha_1}\dot{\alpha_1} + \frac{\partial W}{\partial \alpha_2}\dot{\alpha_2} + \sum_{i=1}^{N}\frac{\partial W}{\partial \lambda_i}\dot{\lambda_i}\right) \geq 0 \tag{3.44}$$

Terms with the factors $\boldsymbol{D}$ and $\boldsymbol{I}\cdot\boldsymbol{D}$ (deviatoric and distortional terms) correspond to purely elastic equilibrium and get canceled out. The dissipative terms remain:

$$\mathcal{D} = \frac{\partial W}{\partial \alpha_1}\Gamma \boldsymbol{A_d}\colon \boldsymbol{I} + \frac{\partial W}{\partial \alpha_2}\Gamma \boldsymbol{A_d}\colon \boldsymbol{b}^*_{\boldsymbol{de}} \geq 0 \tag{3.45}$$

A hyperelastic model for W, as well as a suitable function for Γ, need to be defined. For the latter, positivity of the dissipation needs to be ensured, and the following function is generally used:

$$\Gamma = (\Gamma_1 + \Gamma_2\|\boldsymbol{D}\|)\exp\left(-\frac{1}{2}\left(\frac{Z}{\|\boldsymbol{b}^*_{\boldsymbol{de}}\|}\right)^{2n}\right) \tag{3.46}$$

where Z is the effective hardening associated with fluid flow, Γ_1, Γ_2, n are material parameters and $\|\boldsymbol{X}\| = \sqrt{2/3\boldsymbol{X_{dev}}\colon \boldsymbol{X_{dev}}}$ is a specific tensorial norm, analogous to the definition of the Von Mises stress, the subscript *dev* referring to the deviatoric part of tensor $\boldsymbol{X}$, i.e. $\boldsymbol{X_{dev}} = \boldsymbol{X} - 1/3(\boldsymbol{X}\colon \boldsymbol{I})\boldsymbol{I}$. Z is determined by the evolution equation:

$$\dot{Z} = \left(\frac{r_1 r_3 + r_2\|\boldsymbol{D}\|}{r_3 + \|\boldsymbol{D}\|}\right)\Gamma\|\boldsymbol{b}^*_{\boldsymbol{de}}\| - r_4 Z^{r_5} \tag{3.47}$$

and $(r_1, \cdots, r_5)$ are additional material constants. Note that $\|\boldsymbol{D}\|$ corresponds to the effective total distortional deformation rate $\dot{\varepsilon}$.

The Rubin-Bodner model incorporates hyperelasticity, tissue anisotropy with the introduction of fiber families, and a dissipative component represented here as a consequence of temporary structural rearrangements and fluid flow in the material. The observed changes in volume during deformation, as described in Section 2.4.10, can be therefore explained by the outflow of the water content and quantified in the model. In essence, the constitutive framework is akin to a Maxwell model with an elastic component and a dissipative/viscoplastic component in parallel. Although the general form of the Rubin-Bodner model is quite complex, several simplifications are often made. Rubin and Bodner [182] chose an exponential hyperelastic function that neglects the influence of β_2 and α_2, and only one fiber family was considered, without dispersion and no resistance to compression. The experimental dataset on excised facial skin, taken from the work of Har-Shai et al. [186], is not sufficient to fully determine the 14 constitutive parameters of the proposed model. The authors suggested to reduce the parameter set to 7 material constants, by pre-setting the value of the 7 others, based on expected physical features of the tissue. It was also assumed that the volumetric deformation is characterized by the volumetric response of the internal fluid, assimilated here to water. The proposed formulation has proven to be a very good descriptor for cyclic loading and stress relaxation of facial skin, and captures all the physical features identified by Fung [181].

The same constitutive framework was implemented into a finite element model of facial skin and subcutaneous layers by Mazza et al. [183] to simulate the long term effects of aging. No fibers were incorporated; instead, a layered model was described and an aging parameter was introduced, to model loss of tissue stiffness with time. Although the simulations are based on very simplistic assumptions of the tissue behavior, their results suggest that the short-term response of facial tissue is not affected over large periods of time, and that the long-term response is dominated by the gradual reduction in elastic stiffness, which has interesting ramifications for the study of aging mechanisms. Additional experimental data on *in vivo* facial skin were later gathered by Barbarino et al. [187] to improve the accuracy of the layered model.

Flynn and Rubin [185] applied a similar approach with a discretized fiber distribution model [171] coupled with a dissipative component, described following Hollenstein et al. [188]. Although their model successfully matches the biaxial loading-unloading and stress relaxation tests of rabbit skin reported by Lanir and Fung [41], the large parameter set (21 material constants) poses substantial problems in terms of uniqueness of the identified solution. The authors indicate this set can be reduced by pre-

determining some of the structural quantities, e.g. the orientation distribution of collagen fibers, yet a notable limitation is that the model parameters are for the most part phenomenological. The dissipative features, as well as fiber uncrimping, are not described by physical processes of the tissue structure. The model also shows limited success at larger strains, where more irreversible processes start taking place.

3.6.2. Breakage and rearrangement of interfibrillar bridges

In a soft collagenous tissue, the collagen fibrils within a same fiber are interconnected via peripheral cross-links that bridge them together. With the assumption of discontinuous fibrils, these cross-links, besides providing structural integrity to the fiber, also enable force transfer, something that has been modeled earlier by Puxkandl [178] for collagen in tendon. Upon stretching, mechanisms of rupture, slippage, and reformation of these junctions can therefore ensue. Thus, irreversible deformation happens when ruptured bonds can no longer (or do not have the time to) reform and slippage reaches a critical level. Ciarletta and Ben Amar [189] addressed this aspect with a dissipative constitutive model, intended for ligaments and tendons in their case, but which could be extended to skin as well. The model considers a set of collagen fiber families (ff) embedded in an isotropic matrix (m). For the sake of simplicity index $i = \{m, ff\}$ is used to refer to each constituent, unless the equation differs. During deformation, one can consider that a certain fraction of mass of constituent i, $N_i(t, \tau)$ has rearranged before an intermediate time τ, such that $0 \leq \tau \leq t$. $N_i(t, 0)$ is therefore the current concentration of constituent that has not rearranged yet. Relative rates of reformation $\gamma_i(\tau)$ [190] are defined by:

$$\gamma_i(\tau) = \frac{1}{N_i(0,0)}\left[\frac{\partial N_i(t,\tau)}{\partial \tau}\right]_{t=\tau} \tag{3.48}$$

These occur at random times. Similarly, rates of breakage of the constituents can be introduced:

$$\begin{aligned} \Gamma_i(t,0) &= -\frac{1}{N_i(t,0)}\frac{\partial N_i(t,0)}{\partial t} \\ \Lambda_i(t,\tau) &= -\left[\frac{\partial N_i(t,\tau)}{\partial \tau}\right]^{-1}\frac{\partial^2 N_i(t,\tau)}{\partial t \partial \tau} \end{aligned} \tag{3.49}$$

where $\Gamma_i(t, 0)$ is the rate of breakage of units that have not rearranged, while $\Lambda_i(t, \tau)$ is the rate of breakage of units rearranged before time τ. Integration of Eqs. (3.48) and (3.49) leads to the following expressions:

$$\begin{aligned} N_i(t,0) &= N_i(0,0)\exp\left(-\int_0^t \Gamma_i(s,0)ds\right) \\ \frac{\partial N_i(t,\tau)}{\partial \tau} &= N_i(0,0)\gamma_i(\tau)\exp\left(-\int_\tau^t \Lambda_i(s,\tau)ds\right) \end{aligned} \tag{3.50}$$

By decoupling the behavior of rearranged and broken units in the energy density function, a dissipative component of the mechanical response can be isolated, capturing history-dependent processes. Functions $\gamma_i(\tau)$ and $\Lambda_i(t, \tau)$ are fully determined by the thermally activated processes that govern the kinetics of breakage and rearrangement, as well as by the loading conditions. In their models of tendon and ligament, Ciarletta and Ben Amar [189] chose to represent the matrix using a Mooney-Rivlin description, and implemented a modified GOH model for the collagen fibers. The rates of breakage in the matrix and at the interfibrillar level were defined via the Eyring theory of thermally activated processes [191] and the Wagner phenomenological relationship [192]:

$$\Gamma_i(t,0) = \Gamma_i^0 \exp\left(\kappa_i \sqrt{N_i(0,0)W_i(t,0)}\right) \tag{3.51}$$

where Γ_i^0 is the constant rate of breakage of component i,and κ_i is a material parameter. Breakage and rearrangement occurs at the interfibrillar level and in the matrix, allowing for a representation of both damage and viscoelasticity, which can be particularly suited for cyclical or dynamic testing of collagenous tissues, and has proven to give accurate results with a considerably reduced amount of parameters (see Fig. 3.10).

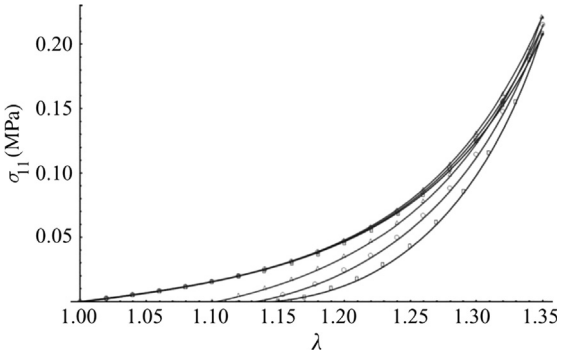

Fig. 3.10. The dissipative constitutive model proposed by Ciarletta and Ben Amar [189] shows remarkable agreement with experimental results from strain-dependent tensile loading and unloading tests in periodontal ligaments, performed by Natali et al. [223]. From [189].

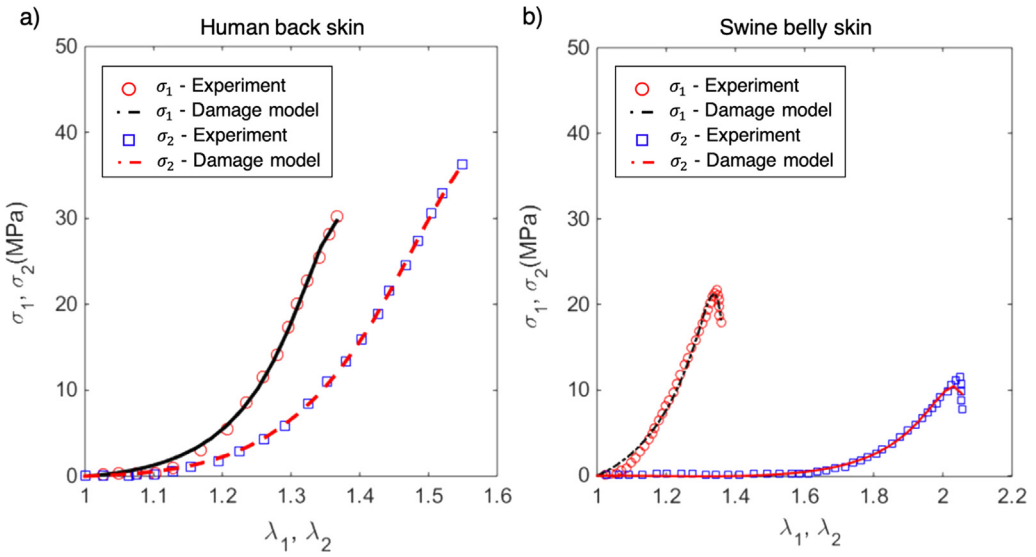

Fig. 3.11. Computed and measured stress-stretch curves of uniaxial tests in perpendicular orientations on (a) human back skin [140] and (b) swine belly skin [46]. Li and Luo [194] implemented a Volokh damage model with a GOH nonlinear elastic model to capture the softening behavior of skin prior to sample failure. Adapted from [194].

3.6.3. Volokh's model

Volokh [193] proposed a phenomenological model for the damage-induced behavior of soft anisotropic materials, by introducing energy limiters. When failure is initiated, the global stress in the material decreases and the behavior can no longer follow the strain energy function of the intact material. The following formulation for the strain energy ψ was suggested:

$$\psi(\phi, m, W) = \frac{\phi}{m}\left[\Gamma\left(\frac{1}{m}, 0\right) - \Gamma\left(\frac{1}{m}, \frac{W^m}{\phi^m}\right)\right] \tag{3.52}$$

where ϕ is the energy limiter, m describes the sharpness of the failure transition, W is the strain energy function of the intact material, and Γ is the upper-incomplete gamma function $\Gamma(s, x) = \int_x^\infty t^{s-1}e^{-t}dt$. It can be noted that for $\phi = \infty$, then $\psi = W^m$, which corresponds to a material without failure, otherwise the energy is always limited by the value of ϕ.

Volokh [193] suggested that an extended GOH model with two fiber families f_i and a neo-Hookean matrix M would be particularly suited to simulate the damage-induced behavior of arterial walls:

$$\psi(\phi_i, m_i, W_i) = W_M(\phi_M, m_M, W_{NH}) + \sum_{i=1}^{2} W_{fi}(\phi_{f_i}, W_{GOH}) \tag{3.53}$$

Li and Luo [194] implemented the Volokh framework to model uniaxial deformation of skin from different species, for which the data was accessible from the literature. The model reproduced very well the softening behavior at high strains with a relatively low number of additional parameters, although some of them need to be pre-set in the case of uniaxial tensile tests, where information on the anisotropy of the material is lacking. Some results showing the performance of the model on human skin [140] and swine belly skin [46] are presented Fig. 3.11. The authors report that the mean fiber angle β and the dispersion factor κ of the GOH model are the parameters that have the highest influence on the damage model, suggesting that it is preferable to determine them initially.

3.6.4. Shear-Lag model

It is generally believed that mechanisms of shear play an critical role in the viscoelastic and dissipative behavior of skin, mostly at high strains [7,40,178]. Interfibrillar and fiber-matrix shear interactions occur during the straightening process of fibers (or fibrils), and most importantly when they start sliding past each other. The shear-lag model takes these processes into consideration by estimating the relative displacement between fibers during deformation. It was initially introduced by Cox in 1952 [195] for fiber reinforced composites, and later on adapted to biological tissues [151,196-198].

In the model, a unit representative cell consists of two discontinuous elastic fibrils embedded in a viscous matrix. When a tensile load is applied at the edges of the cell, the two fibrils move in opposing directions, thus generating shear in the matrix interface. Szczesny and Elliot [151] also incorporated fiber crimp in their shear-lag model of tendon, but assumed that only fully straightened fibers bear load and transfer shear stresses. Following the representation in Fig. 3.12, we consider that a tensile load is applied in the x-direction, +P for fiber 1 and –P for fiber 2. Fibers are of initial length L (such that the unit cell is of length L/2) and of radius r, and are significantly stiffer than the viscoelastic matrix. In this case, the stresses in each fiber σ_i must equilibrate with circumferential shear stresses τ:

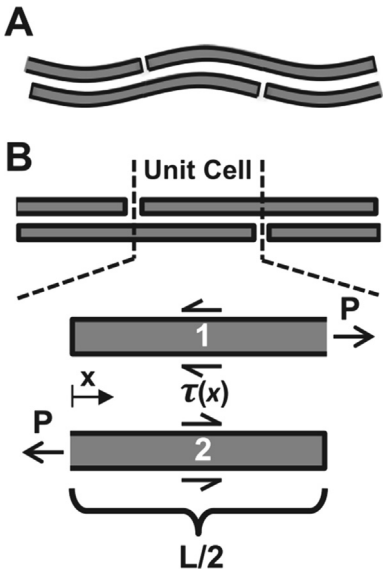

Fig. 3.12. Microstructural shear-lag model described by Szczesny and Elliot [151]. A simplified representation of discontinuous fibers consists of a unit cell with two fibers embedded in a matrix. In the initial configuration, fibers are crimped (A), and bear loads only when fully straightened (B). The applied tensile loads are transferred to the matrix via shear stresses τ.

$$\frac{\partial \sigma_1(x,\,t)}{\partial x} = -\frac{\partial \sigma_2(x,\,t)}{\partial x} = \frac{2\tau(x,\,t)}{r} \tag{3.54}$$

Additionally, the force balance on the unit cell gives the following relationship:

$$P(x,\,t) = \pi r^2(\sigma_1(x,\,t) + \sigma_2(x,\,t)) \tag{3.55}$$

Shear stresses lead to relative sliding δ between fibers 1 and 2, with:

$$\delta(x,\,t) = u_1(x,\,t) - u_2(x,\,t) \tag{3.56}$$

The constitutive relationship in each fiber yields:

$$\sigma_i(x,\,t) = E_f \varepsilon_i(x,\,t) = E_f \frac{\partial u_i(x,\,t)}{\partial x} \tag{3.57}$$

where E_f is the Young's modulus of the fibrils. Eqs. (3.55), (3.56), and (3.57), can be rearranged such that:

$$\begin{aligned} \sigma_1(x,\,t) &= \frac{E_f}{2}\frac{\partial \delta(x,t)}{\partial x} + \frac{P(x,t)}{2\pi r^2} \\ \sigma_2(x,\,t) &= -\frac{E_f}{2}\frac{\partial \delta(x,t)}{\partial x} + \frac{P(x,t)}{2\pi r^2} \end{aligned} \tag{3.58}$$

Lastly, the interfibrillar matrix shear strain $\gamma(x,\,t)$ is expressed as:

$$\gamma(x,\,t) = \frac{\delta(x,\,t)}{h} \tag{3.59}$$

where h is the vertical spacing between fibers. By rearranging Eqs. (3.54), (3.58) and (3.59), we find that:

$$\frac{rhE_f}{4}\frac{\partial^2 \gamma(x,\,t)}{\partial x^2} = \tau(\gamma) \tag{3.60}$$

So the evolution of γ depends on the constitutive law between the shear stress τ and the shear strain γ.

In their shear-lag model of tendon fascicle, Szczesny and Elliot [151] compared elastic, plastic, and combined elastoplastic models for the constitutive relationship of the interfibrillar shear stress. According to their analysis, the plastic model represents more accurately the deformation process of a fascicle than the elastic model, because it predicts the observed tissue softening behavior (Fig. 3.13). The combined elastoplastic model, which introduces an additional parameter, slightly improves the total prediction, but stays very close to the plastic model.

More recently, Wu et al. [196] implemented a Kelvin-Voigt model for the shear behavior of the matrix, to account for viscoelastic processes occurring in the structure. This requires complex solving of a nonhomogeneous PDE. Although the model encompasses the dynamic behavior of the tissue, it still cannot represent the softening response captured by the plastic model.

It should also be pointed out that shear-lag models of collagenous tissue are principally representing interactions at the fibril level. Although relative sliding at the fiber level probably plays a non-negligible role in the dissipative behavior of skin, some key points

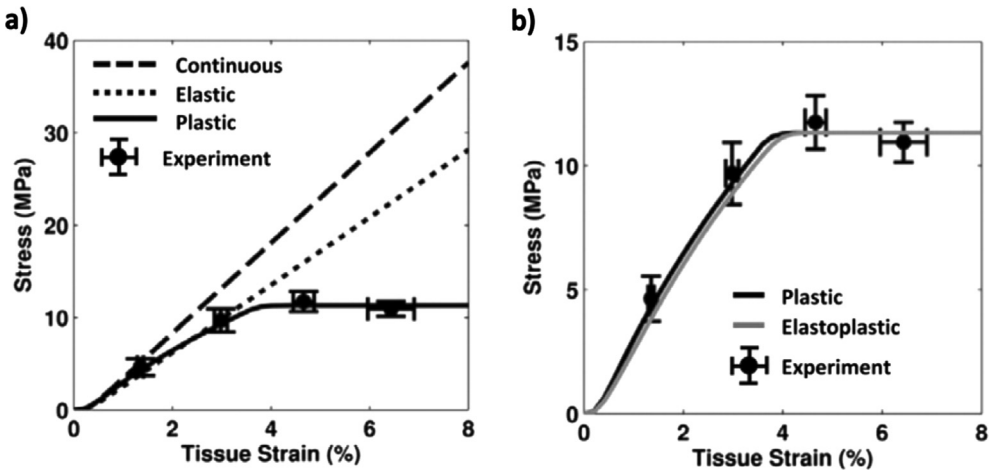

Fig. 3.13. Performance of the shear lag model to predict the tensile behavior of tendon fascicle, with different constitutive laws for the shear behavior of the matrix: (a) – continuous (no shear lag), elastic, plastic; (b) – plastic and combined elastoplastic. Even though the elastic shear lag model gives a better representation of the macroscopic stiffness of the fascicle, it is unable to simulate the softening behavior at higher strains, unlike the plastic and elastoplastic models. From [151].

need to be addressed to include these processes into a structural model of the dermis. First, the description of the unit representative cell in the shear-lag model entails fiber discontinuity, and little is known about the extended length of collagen fibers in the dermis, or on how fibers are connected at their ends. Second, fiber dispersion in skin makes it challenging to provide a global representation of the shear interaction, compared to the proposed parallel arrangement. Further complications are introduced if one accounts for a certain degree of fiber entanglement.

4. Advantages and limitations of semi-structural modeling

The present review details a broad range of models that have been (or could be) implemented to describe the mechanical behavior of skin, including nonlinear elasticity, anisotropy, viscoelasticity, evolution of damage, or other dissipative processes. Although phenomenological isotropic models are sometimes preferred for their simplicity and ease of implementation, they are generally limited by the lack of physical significance of the parameters at play. Moreover, because soft collagenous tissues like skin exhibit high anisotropy, isotropic models do not appear as an appropriate choice. In contrast, semi-structural models attempt to bridge the structure-property gap by taking into account the contribution of distinct constituents and, to some degree, their structural arrangement. In the case of skin, the material is generally represented as the assembly of the collagenous network, the ground substance, and more rarely the elastin fibers. This decomposition enables the decoupling of strain-energy functions, usually phenomenological, associated with the behavior of each component. With this approach, specific physical features of the material can be attributed to the properties of separate constituents: tissue anisotropy can be related to collagen fiber splay, or viscoelasticity can be taken a property of the ground substance, for example. For the collagen fiber network, additional structural accuracy is reached by incorporating the dispersion in orientation of fibers.

With a more detailed description, models increase in complexity, and more constitutive parameters are generally introduced. Concurrently, the representation of the structure is more accurate, and the parameters gain in physical relevance. The macroscopic deformation of the tissue can be associated with processes occurring in the microstructure, and the model can be informed by previously determined structural data on the material, thus potentially reducing the number of constitutive parameters that need to be identified. However, the predetermination of material constants should be addressed with care: this approach is only appropriate if the proposed structural arrangement and the associated mechanical processes provide a reasonable approximation of reality.

A considerable amount of research has been conducted to fully characterize the mechanical properties of the main components of skin [11,199,200]. Main difficulties that remain to be overcome to improve semi-structural models are to identify the correct structural arrangement of each of these components, and how they interact with each other. Current knowledge on the actual distribution of collagen fibers in the dermis is still quite limited, especially given that it varies substantially according to species, region of the body, age, and other factors.

Studies that involve microscopic imaging of skin are essentially restricted to two-dimensional visualization of the dermis, and understanding the out-of-plane arrangement can still be challenging. Li [201] reviewed some existing hypotheses for the distribution of collagen fibers in skin, essentially centered around idealized two-dimensional fiber networks with varying degrees of freedom [202-204]. Sherman et al. [11], based on Transmission Electron Micrographs of rabbit skin, proposed that the dermis consists of plane layers of imbricated collagen fibers, also with varying angular distributions, supporting the hypothesis of a planar arrangement as well. Yet, some other studies, including the work of Jor et al. [13] for pig skin and Ferdman and Yannas [205] for human skin, report a three-dimensional organization of collagen, with preferred angular alignments close to $\pm$ 45° in the cross-section and a high

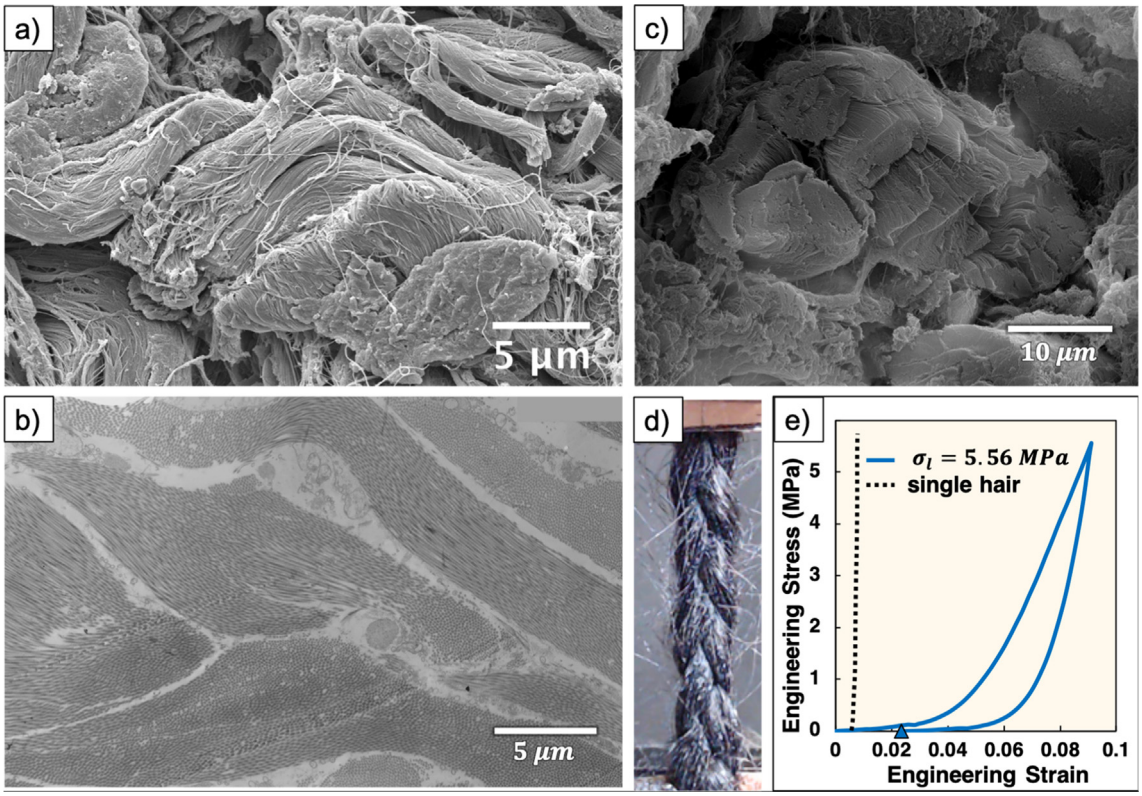

Fig. 4.1. (a) Scanning electron micrograph (SEM) of collagen in the porcine dermis, showing entangled collagen fibers. (b) The transmission electron micrograph of a longitudinal section of porcine dermis also suggests that such an arrangement is possible, with many neighboring fibers, approximately 3–5 μm in diameter, coming in and out of plane. (c) SEM of a cross-section of porcine dermis, with a fascicle-like group of collagen fibers, having a diameter of 30 μm approximately. Since these structures do not seem to appear continuously in the dermis, perhaps the entanglement is not constant and only some portions are interwoven. (d) Triple braid of dark human hair, used as an analogy to describe the mechanical behavior of braided structures in the dermis. (e) The associated loading/unloading curve shows a response that reminds of the dissipative behavior of skin. From Pissarenko et al. [12].

degree of interweaving, far from planar models for which this angle stays at 0°, and where fibers do not cross. Models extending to three-dimensional networks, or with braided structures, have seldom been explored at this point. Pissarenko et al. [12] proposed that a certain degree of entanglement could exist between collagen fibers, sometimes resulting in twisted or braided structures, as Fig. 4.1 shows. These entanglements could be locally dispersed in the dermis, and a simple analogy with triple braids of hair suggests that this kind of structural arrangement could explain to some extent the dissipative behavior observed in loading/unloading tests, at the fiber level.

Fiber crimp plays an important role in the nonlinear behavior of skin. The tensile response of wavy collagen fibers is marked by a transition from the straightening process, requiring little elastic energy, followed by a purely tensile state. In semi-structural models, this process is incorporated by defining piecewise phenomenological functions for collagen fibers, depending on the stretch state, or nonlinear functions that approximate this transition, such as exponential functions for example. In a number of representations, it is also frequently assumed that collagen fibers bear no load in compression. This distinction in elastic behavior participates to the anisotropy and the nonlinear elasticity of the material, and is therefore an important mathematical consideration for constitutive models. Models can be informed by direct measurements of the undulation of collagen fibers in their resting state, which provides an estimate of the transition from crimped to fully taught configurations. To incorporate fiber curvature, beam-like representations of collagen fibers can also be encountered in the literature, most of which were reviewed by Sherman et al. [108] (see Fig. 4.2). Planar representations include rigid corner [206,207], sequential loading [208], sinusoidal [152,209,210], and semi-circular [11,40] models. The helical model [211] is the only representation with a three-dimensional fiber configuration, forming a spring-like coil. While it is probably more suitable to describe a tridimensional, interwoven arrangement of the collagen network, the determination of an undulation parameter is more challenging. An advantage of beam-like descriptions is that such models can be adjusted to reproduce the microscale deformation of collagen fibers, and the framework can be extended to a macroscale model of the dermis, based on representative elements [149,152,212]. Microscopic imaging of the collagen network and micromechanical testing on isolated fibers provide information that can serve to tune the model. Important questions remain concerning fiber characteristic length, and the nature of their attachment with other fibers and their surroundings, which need to be address to define appropriate loading and boundary conditions.

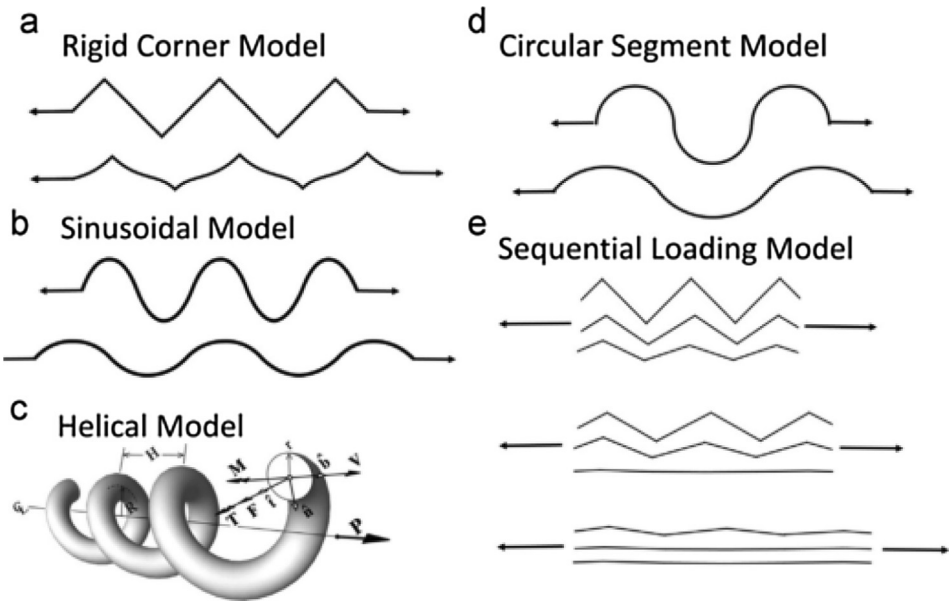

Fig. 4.2. Beam-like models of collagen fibers. (a) The rigid corner model (Diamant et al. [206]) assumes that straight oblique beams are rigidly jointed together, adding rigidity to the structure and limiting the straightening process. (e) The sequential loading model (Kastelic et al. [208]) assumes free rotation at the joints, implying that the beam bears load only when fully straightened, as in most elastic models presented in this review. The (b) sinusoidal (Comminou and Yannas [209], Lanir [174], Gao et al. [152]) and (d) circular segment (Sherman et al. [11]) models attempt to replicate the smooth curvy shape of collagen in the dermis. (c) The helical model (Freed and Doehring [211]) extends the structure in three dimensions, to account for the out-of-plane configuration of the fibers. Reprinted from Sherman et al. [108].

Significantly less information is available on elastin. Weinstein and Boucek [213], but also Brown [67], and Belkoff and Haut [146], question its contribution in the deformation process, mainly because of its low weight percentage in the dermis and its high extensibility. This justification is often provided when the influence of the elastin network is neglected in constitutive models, or absorbed into the contribution of the ground substance. Yet, Lanir [174], Oxlund et al. [214], as well as others [56,159,160], argue that elastin is mainly responsible for the quick recoil of skin at low strains, which studies on skin with denatured elastin seem to confirm [214].

5. An application of skin mechanics: Synthetic skin

Current signs of progress in bioengineering are gradually broadening the possibilities in terms of mimicking the behavior of biological materials. Important breakthroughs involve the development of functional and biocompatible synthetic materials with matching structure and mechanical properties. In the clinical context, applications with synthetic skin grafts can offer great perspectives for patients with deep and/or large burns, or large tissue excisions for example. Various products are already commercially available, ranging from synthetic sheets [215-217] to 3D printed tissue [32,218,219]. However, an ongoing challenge is to match as closely as possible the mechanical properties of the skin, in order to maximize conformity between the graft and the tissue, in the affected region. Difficulties arise from the fact that these properties can vary according to region of the body, age, gender, and health condition. It is therefore essential to have a complete understanding of the mechanics of the material prior to replicating it, both from macrostructural and microstructural standpoints. Experimental results supply a large database of expected responses, while models can provide objectives in terms of mechanical parameters to match. By referring to them, the choice of fabrication materials is simplified.

Common existing solutions consist of a polymer sheet that provides a scaffold for new skin to grow. This process can be facilitated by pre-growing in a bioreactor some of the patients' fibroblasts and keratinocytes from their healthy skin into the scaffold. The cells are expected to produce a suitable extracellular matrix, compliant with the properties of the skin. During the regeneration process, the mechanical properties change, due to densification of collagen and keratin (at the epidermis level). Sander et al. [220] reported these changes from collagenous scaffold grafted on mice, presented in Fig. 5.1. Their study shows that engineered synthetic skin, initially quasilinear elastic, starts stiffening and eventually behaves more nonlinearly, after infiltration of cells and grafting. Six weeks after surgery, synthetic skin replicates quite well the J-curve behavior in tension, although the regenerated tissue is still too stiff to fully comply with healthy skin. Similar observations are also made with autografts or scarred tissue. The authors point out that cell concentration, polymer properties, infiltration and post-grafting times are important parameters that will affect the response of the material, and should be investigated in the future. To palliate problems with densification, and to better control the regeneration of the tissue, other approaches intend to directly create a scaffold mimicking the collagen fiber arrangement, and therefore matching the mechanical properties of skin. This can be achieved by electrospinning, where fiber geometry, orientation, and mechanics can tuned.

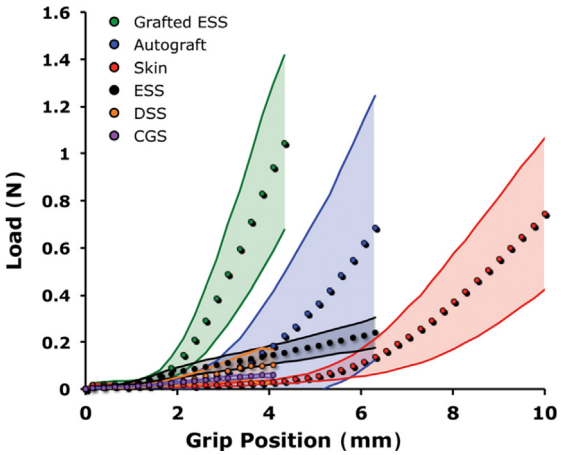

Fig. 5.1. Tensile response of engineered synthetic skin grafts at different stages of cell infiltration and post-surgery. Healthy skin and autografted skin are also added for comparison. CGS: Collagenous Scaffold; DSS: CGS infiltrated with fibroblasts; ESS: DSS seeded with keratinocytes on the top surface. Results six-weeks after surgery (Grafted ESS) show that the grafted synthetic skin starts replicating the nonlinear behavior of healthy and autografted skin, but the material is stiffer and less stretchable. Reprinted from Sander et al. [220].

Such methods have been reviewed in detail by Dias et al. [221]. 3D printed truss-lattice microstructures are another interesting direction that has been adopted for wearable devices [149,222], and could be potentially extended to synthetic grafts.

6. Conclusions and future challenges

In order to fulfill a broad range of vital functions throughout life, it is essential for skin to maintain a certain level of structural integrity, and to have the ability to undergo large deformations caused by motion, impact, and other external factors. The present review focuses on the tensile properties of skin, mostly attributed to the response of the dermis. Understanding, characterizing, and predicting the mechanical response of this complex anisotropic structure to various loads is of valuable importance in many fields of engineering.

The variety of experimental protocols, most of which are reviewed here, and the lack of standardized testing methods for skin yield results that often cannot be directly compared. For example, the estimation of a tangent modulus for the linear portion of skin depends on the testing conditions, the experimental protocol, or the tested species. It shows values that can differ by up to four orders of magnitude (cf. Table 2.1). This indicates that particular attention needs to be paid to the specifics of the experimental methods, and to the approach used to obtain representative parameters. With a consistent experimental framework, some qualitative and sometimes quantitative results can be observed, highlighting the influence of factors such as tested organ, age, gender, species, external temperature, hydration, and dynamics and loading history. Constitutive modeling is a valuable tool to extract quantitative information from the database of experimental results, via the identification of material constants.

However, in a number of studies, the experimental characterization and constitutive modeling are often conducted independently from each other. Experimental results are taken from a previous study, or the protocol is designed without accounting for the amount of information that is required by the model to adequately determine the material constants. As pointed out by Rubin and Bodner [182] and by Holzapfel et al. [114], there is a need to develop experimental methods in concert with model development, so that sufficient information is available, and the three-dimensional mechanical response of skin can be fully characterized.

Constitutive models of skin vary in complexity, with a tradeoff between the number of parameters and the ability of the model to reflect the material's structural arrangement, as well as the mechanical processes taking place at the microstructure scale. While it can be preferable to maintain a certain level of simplicity to reduce the computational cost and increase the robustness of a model, more accurate and consistent parameters can be obtained with a more realistic description of the tissue structure. Ideally, a good constitutive model should not only be descriptive, and match the mechanical response for a fixed number of experimental results, but also predictive, meaning that it should also be able to predict the behavior of the material for given loading conditions that differ from the reference test set. This is one of the fundamental limitations encountered with isotropic hyperelastic models, despite the fact that they have been extensively used to characterize the tensile response of skin. In contrast, structurally-based descriptions of the dermis enable the incorporation of effects of anisotropy, with physically relevant constitutive parameters, under the condition that the assumptions of the model are in close agreement with reality.

It is also important to consider the experimental results that are available to inform the model: for example, a dissipative component has limited interest if the dissipative response of the tissue is not observed. *In vivo* or *ex vivo* testing conditions yield notable differences in edge effects, surrounding tissues, and potentially compressibility, which need to be considered in the selected model. Uniaxial tensile testing does not provide sufficient information to fully characterize skin anisotropy, therefore the identified material constants may not be unique or reflect reality if a complex anisotropic model with dispersed fibers is chosen. Moreover, if no structural data are available on the tested sample, then the representation of fiber distribution is merely an assumption of the model,

based on available statistical analyses on fiber dispersion. With significant inter-sample variability, pre-setting the associated constitutive parameters increases the likelihood of inaccurately describing the material. Hence, there is a need to develop multi-scale modeling frameworks coupled with experimental techniques that inform the model at different levels of scale, such as *in situ* microscopy imaging, as well as more general testing protocols that characterize the three-dimensional response of skin [9,113,114] and provide additional insight into the interactions between the constitutive elements.

The structural arrangement of the constituents of the dermis can be investigated using microscopy imaging techniques, such as scanning electron microscopy (SEM), transmission electron microscopy (TEM), or multiphoton microscopy. With large inter-sample variations, it is an arduous task to reach a general level of representation of the tissue structure. Semi-structural models with angular integration or generalized structure tensors opt for a statistical description of the collagen network, offering a reasonable compromise between structural representativity and model complexity. With recent developments in computational modeling, discrete network modeling with stochastic fiber distributions are also an interesting direction to pursue.

SEM, multiphoton microscopy, or small angle x-ray scattering, can be coupled with mechanical testing devices to observe the deformation *in situ*, adding the possibility to study time-dependent and dissipative processes at the microscale level. These approaches involve the development of advanced testing platforms, and are complicated by several factors. It is challenging to apply them in the *in vivo* configuration, and the testing conditions *ex vivo* often require vacuum, water immersion, lengthy sample preparation (and potential deterioration), which is far from physiological conditions.

Replicating the structure and the mechanical behavior of skin can yield important outcomes in fields such as tissue engineering, interventional surgery, or cosmetics, where conformity of the material is essential. Developing fabrication methods that generate synthetic tissues that match the features of skin is another challenging task. The following are some unresolved problems that, in our opinion, would benefit from concentrated research efforts:

- What is the role of elastin in the mechanical response of the skin? Although elastin represents only a small volume fraction, some researchers attribute a significant effect on the mechanical response. There are varied comments about its role, some dealing with the reversible deformation. Nevertheless, there is little quantification of its effect.
- What are the processes associated with changes in volume during the deformation of skin? A reduction in volume is often associated with internal fluid outflow, but this process has not been quantified in detail. On the other hand, increases in volume are attributed to the auxetic nature of the fiber network, although there is very little evidence of structural features that support these claims at the moment.
- The fracture toughness and tear resistance of skin have been studied to a limited extent. Conventional tear opening tests for Mode I with a conventional tensile geometry presents problems such as the warping of the specimen out of the plane. The trouser test for Mode III is sometimes preferred for elastomers, but this yields a parameter in the out-of-plane direction, which might not be the principal mode of tear propagation in skin. The application of the J-integral approach to the fracture toughness of skin could also reveal many important structure-property features.
- Mechanical response of scar tissue. Scars affect the distribution of tension in skin, as shown for example by Wong et al. [25], and cause stress concentration at the interface with healthy tissue. How do these stresses vary with distance from the scar? Some analogies with the process of tear propagation and toughness could be drawn, and lead to improved surgical procedures and minimally invasive surgery.
- Dynamic response of skin. Little has been done, other than compressive tests (with strain rates up to 4000 s^{-1}) by Shergold et al. [44] on porcine skin, and tensile testing by Ottenio et al. [130] (up to 167 s^{-1}) on human skin. This has important potential applications in the study of trauma and blast injury in skin.
- Correlation between mechanical extension and structural evolution. Although there are preliminary results, a one-to-one quantitative correlation is lacking. Advanced *in situ* characterization techniques such as small angle X-ray scattering or confocal microscopy can provide answers.

Declaration of Competing Interest

The authors declare that they have no known competing financial interests or personal relationships that could have appeared to influence the work reported in this paper.

Acknowledgments

This work was partially funded by a Multi-University Research Initiative (grant no. AFOSR-FA9550-15-1-0009) from the Air Force Office of Scientific Research to the University of California Riverside, through subcontracts to the University of California, San Diego and the University of California, Berkeley.

References

[1] Tortora GJ, Derrickson B. Principles of anatomy and physiology. John Wiley and Sons, Inc.; 2009.
[2] Whitton JT, Everall JD. The thickness of the epidermis. Br J Dermatol 1973;89:467–76. https://doi.org/10.1111/j.1365-2133.1973.tb03007.x.
[3] Huzaira M, Rius F, Rajadhyaksha M, Anderson RR, González S. Topographic variations in normal skin, as viewed by in vivo reflectance confocal microscopy. J Invest Dermatol 2001;116:846–52. https://doi.org/10.1046/j.0022-202X.2001.01337.x.

[4] Sandby-Møller J, Poulsen T, Wulf HC. Epidermal thickness at different body sites: relationship to age, gender, pigmentation, blood content, skin type and smoking habits. Acta Derm Venereol 2003;83:410–3. https://doi.org/10.1080/00015550310015419.
[5] Hendriks FM, Brokken D, Oomens CWJ, Bader DL, Baaijens FPT. The relative contributions of different skin layers to the mechanical behavior of human skin in vivo using suction experiments. Med Eng Phys 2006;28:259–66. https://doi.org/10.1016/j.medengphy.2005.07.001.
[6] Leyva-Mendivil MF, Page A, Bressloff NW, Limbert G. A mechanistic insight into the mechanical role of the stratum corneum during stretching and compression of the skin. J Mech Behav Biomed Mater 2015;49:197–219. https://doi.org/10.1016/j.jmbbm.2015.05.010.
[7] Jor JWY, Parker MD, Taberner AJ, Nash MP, Nielsen PMF. Computational and experimental characterization of skin mechanics: identifying current challenges and future directions. Wiley Interdiscip Rev Syst Biol Med 2013;5:539–56. https://doi.org/10.1002/wsbm.1228.
[8] Wilkes GL, Brown IA, Wildnauer RH. The biomechanical properties of skin. CRC Crit Rev Bioeng 1973;1:453–95.
[9] Limbert G. Mathematical and computational modelling of skin biophysics: a review. Proc R Soc A Math Phys Eng Sci 2017;473:20170257. https://doi.org/10.1098/rspa.2017.0257.
[10] Butler BJ, Boddy RL, Bo C, Arora H, Williams A, Proud WG, et al. Composite nature of fresh skin revealed during compression. Bioinsp Biomim Nanobiomater 2015;4:133–9. https://doi.org/10.1680/bbn.14.00028.
[11] Sherman VR, Tang Y, Zhao S, Yang W, Meyers MA. Structural characterization and viscoelastic constitutive modeling of skin. Acta Biomater 2017. https://doi.org/10.1016/j.actbio.2017.02.011.
[12] Pissarenko A, Yang W, Quan H, Brown KA, Williams A, Proud WG, et al. Tensile behavior and structural characterization of pig dermis. Acta Biomater 2019. https://doi.org/10.1016/j.actbio.2019.01.023.
[13] Jor JWY, Nielsen PMF, Nash MP, Hunter PJ. Modelling collagen fibre orientation in porcine skin based upon confocal laser scanning microscopy. Ski Res Technol 2011:149–59. https://doi.org/10.1111/j.1600-0846.2010.00471.x.
[14] Zhou M, Zhang N, Liu X. Tendon allograft sterilized by peracetic acid/ethanol combined with gamma irradiation. J Orthop Sci 2014. https://doi.org/10.1007/s00776-014-0556-9.
[15] Parent G, Huppé N, Langelier E. Low stress tendon fatigue is a relatively rapid process in the context of overuse injuries. Ann Biomed Eng 2011;39:1535–45. https://doi.org/10.1007/s10439-011-0254-0.
[16] Schmidt EC, Chin M, Aoyama JT, Ganley TJ, Shea KG, Hast MW. Mechanical and microstructural properties of pediatric anterior cruciate ligaments and autograft tendons used for reconstruction. Orthop J Sports Med 2019:1–12. https://doi.org/10.1177/2325967118821667.
[17] Vardaxis NJ, Brans TA, Boon ME, Kreis RW, Marres LM. Confocal laser scanning microscopy of porcine skin: implications for human wound healing studies. J Anat 1997;190:601–11. https://doi.org/10.1046/j.1469-7580.1997.19040601.x.
[18] Pittet J, Freis O, Périé G, Pauly G. Evaluation of elastin/collagen content in human dermis in-vivo by multiphoton tomography—variation with depth and correlation with aging. Cosmetics 2014:211–21. https://doi.org/10.3390/cosmetics1030211.
[19] Powell JL. The Kerr Incision: John Martin Munro Kerr. J Pelvic Surg 2001;7:177–8.
[20] Meyers MA, Chen P-Y. Biological materials science. Cambridge University Press; 2014.
[21] Langer K. On the anatomy and physiology of the skin. Br J Plast Surg 1978;31:3–8. https://doi.org/10.1016/0007-1226(78)90003-6.
[22] Cox HT. The cleavage lines of the skin. Br J Surg 1941;29:234–40. https://doi.org/10.1002/bjs.18002911408.
[23] Kwak M, Son D, Kim J, Han K. Static Langer's line and wound contraction rates according to anatomical regions in a porcine model. Wound Rep Regen 2014;22:678–82. https://doi.org/10.1111/wrr.12206.
[24] Swaim SF, Henderson RA, Small Fowler D. Animal wound management. Vet Surg 2008;27:158. https://doi.org/10.1111/j.1532-950x.1998.tb00113.x.
[25] Wong VW, Levi K, Akaishi S, Schultz G, Dauskardt RH. Scar zones. Plast Reconstr Surg 2012;129:1272–6. https://doi.org/10.1097/PRS.0b013e31824eca79.
[26] Topaz M, Carmel N, Silberman A. The TopClosure ® 3S System, for skin stretching and a secure wound closure. Eur J Plast Surg 2012:533–43. https://doi.org/10.1007/s00238-011-0671-1.
[27] Gurtner GC, Dauskardt RH, Wong VW, Bhatt KA, Wu K, Vial IN, et al. Improving cutaneous scar formation by controlling the mechanical environment. Ann Surg 2011;254:217–25. https://doi.org/10.1097/SLA.0b013e318220b159.
[28] Gurtner GC, Dauskardt RH, Longaker MT, Yock P. Skin treatment devices and methods with pre-stressed configurations; 2016.
[29] Kamel RA, Ong JF, Eriksson E, Junker JPE, Caterson EJ. Tissue engineering of skin. J Am Coll Surg 2013;217:533–55. https://doi.org/10.1016/j.jamcollsurg.2013.03.027.
[30] MacNeil S. Progress and opportunities for tissue-engineered skin. Nature 2007;445:874–80. https://doi.org/10.1038/nature05664.
[31] Supp DM, Boyce ST. Engineered skin substitutes: practices and potentials. Clin Dermatol 2005;23:403–12. https://doi.org/10.1016/j.clindermatol.2004.07.023.
[32] Cubo N, Garcia M, Cañizo JF, Velasco D, Jorcano JL, del Cañizo JF, et al. 3D bioprinting of functional human skin: production and in vivo analysis. Biofabrication 2016;9:15006. https://doi.org/10.1088/1758-5090/9/1/015006.
[33] Schwartz G, Tee BCK, Mei J, Appleton AL, Kim DH, Wang H, et al. Flexible polymer transistors with high pressure sensitivity for application in electronic skin and health monitoring. Nat Commun 2013;4:1858–9. https://doi.org/10.1038/ncomms2832.
[34] Wang X, Gu Y, Xiong Z, Cui Z, Zhang T. Silk-molded flexible, ultrasensitive, and highly stable electronic skin for monitoring human physiological signals. Adv Mater 2014;26:1336–42. https://doi.org/10.1002/adma.201304248.
[35] Rodrigues L. EEMCO guidance to the in vivo assessment of tensile functional properties of the skin. Skin Pharmacol Physiol 2001;14:52–67. https://doi.org/10.1159/000056334.
[36] Fung YC. Biomechanics: its foundations and objectives. 2nd ed. Prentice Hall Inc.; 1972.
[37] Groves RB, Coulman SA, Birchall JC, Evans SL. An anisotropic, hyperelastic model for skin: experimental measurements, finite element modelling and identification of parameters for human and murine skin. J Mech Behav Biomed Mater 2013;18:167–80. https://doi.org/10.1016/j.jmbbm.2012.10.021.
[38] Vogel HG, Hilgner W. The, "step phenomenon" as observed in animal skin. J Biomech 1979;12:75–81. https://doi.org/10.1016/0021-9290(79)90011-3.
[39] Haut RC. The effects of orientation and location on the strength of dorsal rat skin in high and low speed tensile failure experiments. J Biomech Eng 1989;111:136–40. https://doi.org/10.1115/1.3168354.
[40] Yang W, Sherman VR, Gludovatz B, Schaible E, Stewart P, Ritchie RO, et al. On the tear resistance of skin. Nat Commun 2015;6:6649. https://doi.org/10.1038/ncomms7649.
[41] Lanir Y, Fung YC. Two-dimensional mechanical properties of rabbit skin—II. Experimental results. J Biomech 1974;7:171–82. https://doi.org/10.1016/0021-9290(74)90058-X.
[42] Lim J, Hong J, Chen WW, Weerasooriya T. Mechanical response of pig skin under dynamic tensile loading. Int J Imp Eng 2011;38:130–5. https://doi.org/10.1016/j.ijimpeng.2010.09.003.
[43] Uzer G, Ho A, Clark RAF, Chiang F. Mechanical properties of pig skin. Proc SEM Annu Conf. 2009.
[44] Shergold OA, Fleck NA, Radford D. The uniaxial stress versus strain response of pig skin and silicone rubber at low and high strain rates. Int J Impact Eng 2006;32:1384–402. https://doi.org/10.1016/j.ijimpeng.2004.11.010.
[45] Lim KH, Chew CM, Chen PCY, Jeyapalina S, Ho HN, Rappel JK, et al. New extensometer to measure in vivo uniaxial mechanical properties of human skin. J Biomech 2008;41:931–6. https://doi.org/10.1016/j.jbiomech.2008.01.004.
[46] Ankersen J, Birkbeck AE, Thomson RD, Vanezis P. Puncture resistance and tensile strength of skin simulants. Proc Inst Mech Eng H 1999;213:493–501. https://doi.org/10.1243/0954411991535103.
[47] Zhou B, Xu F, Chen C, Lu T. Strain rate sensitivity of skin tissue under thermomechanical loading. Philos Trans R Soc A Math Phys Eng Sci 2010;368:679–90. https://doi.org/10.1098/rsta.2009.0238.
[48] Łagan SD, Liber-Kneć A. Experimental testing and constitutive modeling of the mechanical properties of the swine skin tissue. Acta Bioeng Biomech Orig Pap 2017;19. https://doi.org/10.5277/ABB-00755-2016-02.
[49] Caro-bretelle AS, Gountsop PN, Ienny P, Leger R, Corn S, Bazin I, et al. Effect of sample preservation on stress softening and permanent set of porcine skin. J

Biomech 2015;48:3135–41. https://doi.org/10.1016/j.jbiomech.2015.07.014.
[50] Ehret AE, Hollenstein M, Mazza E, Itskov M. Porcine dermis in uniaxial cyclic loading: sample preparation, experimental results and modeling. J Mech Mater Struct 2011;6:1125–35. https://doi.org/10.2140/jomms.2011.6.1125.
[51] Lapeer RJ, Gasson PD, Karri V. Simulating plastic surgery: From human skin tensile tests, through hyperelastic finite element models to real-time haptics. Prog Biophys Mol Biol 2010;103:208–16. https://doi.org/10.1016/j.pbiomolbio.2010.09.013.
[52] Pailler-Mattei C, Bec S, Zahouani H. In vivo measurements of the elastic mechanical properties of human skin by indentation tests. Med Eng Phys 2008;30:599–606. https://doi.org/10.1016/j.medengphy.2007.06.011.
[53] Agache PG, Monneur C, Leveque JL, de Rigal J. Mechanical properties and Young's modulus of human skin in vivo. Arch Dermatol Res 1980;269:221–32. https://doi.org/10.1007/BF00406415.
[54] Ni Annaidh A, Bruyere K, Destrade M, Gilchrist MD, Ottenio M. Characterization of the anisotropic mechanical properties of excised human skin. J Mech Behav Biomed Mater 2012;5:139–48. https://doi.org/10.1016/j.jmbbm.2011.08.016.
[55] Pioletti DP, Rakotomanana LR, Benvenuti JF, Leyvraz PF. Viscoelastic constitutive law in large deformations: application to human knee ligaments and tendons. J Biomech 1998;31:753–7. https://doi.org/10.1016/S0021-9290(98)00077-3.
[56] Gallagher AJ, Ni Anniadh A, Kruyere K, Ottenio M, Xie H, Gilchrist MD. Dynamic tensile properties of human skin. 2012 IRCOBI Conf. 2012. p. 494–502. doi:Irc-12-59.
[57] Finlay B. Dynamic mechanical testing of human skin "in vivo". J Biomech 1970;3. https://doi.org/10.1016/0021-9290(70)90040-0.
[58] Kvistedal YA, Nielsen PMF. Estimating material parameters of human skin in vivo. Biomech Model Mechanobiol 2009;8:1–8. https://doi.org/10.1007/s10237-007-0112-z.
[59] Meijer R, Douven LFA, Oomens CWJ. Characterisation of anisotropic and non-linear behaviour of human skin vivo. Comput Meth Biomech Biomed Eng 2017;5842. https://doi.org/10.1080/10255849908907975.
[60] Leveque JL, de Rigal J, Agache PG, Monneur C. Influence of ageing on the in vivo extensibility of human skin at a low stress. Arch Dermatol Res 1980;269:127–35. https://doi.org/10.1007/BF00406532.
[61] Tonge TK, Atlan LS, Voo LM, Nguyen TD. Full-field bulge test for planar anisotropic tissues: Part I-experimental methods applied to human skin tissue. Acta Biomater 2013;9:5913–25. https://doi.org/10.1016/j.actbio.2012.11.035.
[62] Potts RO, Chrisman DA, Buras EM. The dynamic mechanical properties of human skin in vivo. J Biomech 1983;16:365–72. https://doi.org/10.1016/0021-9290(83)90070-2.
[63] Boyer G, Laquièze L, Le Bot A, Laquièze S, Zahouani H. Dynamic indentation on human skin in vivo: ageing effects. Ski Res Technol 2009;15:55–67. https://doi.org/10.1111/j.1600-0846.2008.00324.x.
[64] Reihsner R, Balogh B, Menzel EJ. Two-dimensional elastic properties of human skin in terms of an incremental model at the in vivo configuration. Med Eng Phys 1995;17:304–13. https://doi.org/10.1016/1350-4533(95)90856-7.
[65] Flynn C, Taberner A, Nielsen P. Measurement of the force-displacement response of in vivo human skin under a rich set of deformations. Med Eng Phys 2011;33:610–9. https://doi.org/10.1016/j.medengphy.2010.12.017.
[66] Flynn C, Taberner A, Nielsen P. Mechanical characterisation of in vivo human skin using a 3D force-sensitive micro-robot and finite element analysis. Biomech Model Mechanobiol 2011;10:27–38. https://doi.org/10.1007/s10237-010-0216-8.
[67] Brown IA. A scanning electron microscope study of the effects of uniaxial tension on human skin. Br J Dermatol 1973;89:383–93. https://doi.org/10.1111/j.1365-2133.1973.tb02993.x.
[68] Edwards C, Marks R. Evaluation of biomechanical properties of human skin. Clin Dermatol 1995;13:375–80. https://doi.org/10.1016/0738-081X(95)00078-T.
[69] Ni Annaidh A, Bruyere Karine, Destrade M, Gilchrist MD, Maurini C, Ottenio M, et al. Automated estimation of collagen fibre dispersion in the dermis and its contribution to the anisotropic behaviour of skin. Ann Biomed Eng 2012;40:1666–78. https://doi.org/10.1007/s10439-012-0542-3.
[70] Delalleau A, Josse G, Lagarde J-M, Zahouani H, Bergheau J-M. Characterization of the mechanical properties of skin by inverse analysis combined with the indentation test. J Biomech 2006;39:1603–10. https://doi.org/10.1016/j.jbiomech.2005.05.001.
[71] Gerhardt L-C, Schmidt J, Sanz-Herrera JA, Baaijens FPT, Ansari T, Peters GWM, et al. A novel method for visualising and quantifying through-plane skin layer deformations. J Mech Behav Biomed Mater 2012;14. https://doi.org/10.1016/j.jmbbm.2012.05.014.
[72] Flynn C, Taberner AJ, Nielsen PMF, Fels S. Simulating the three-dimensional deformation of in vivo facial skin. J Mech Behav Biomed Mater 2013;28:484–94. https://doi.org/10.1016/j.jmbbm.2013.03.004.
[73] Pereira JM, Mansour JM, Davis BR. The effects of layer properties on shear disturbance propagation in skin. J Biomech Eng 1991;113:30–5. https://doi.org/10.1115/1.2894082.
[74] Jansen LH, Rottier PB. Some mechanical properties of human abdominal skin measured on excised strips: a study of their dependence on age and how they are influenced by the presence of striae. Dermatologica 1958;117:65–83.
[75] Stark HL. Directional variations in the extensibility of human skin. Br J Plast Surg 1977;30:105–14. https://doi.org/10.1016/0007-1226(77)90001-7.
[76] Vogel H. Age dependence of mechanical and biochemical properties of human skin. Bioeng Ski 1987;3:67–91.
[77] Diridollou S, Berson M, Vabre V, Black D, Karlsson B, Auriol F, et al. An in vivo method for measuring the mechanical properties of the skin using ultrasound. Ultrasound Med Biol 1998;24:215–24. https://doi.org/10.1016/S0301-5629(97)00237-8.
[78] Hendriks FM, Brokken D, van Eemeren JTWM, Oomens CWJ, Baaijens FPT, Horsten JBAM. A numerical-experimental method to characterize the non-linear mechanical behaviour of human skin. Ski Res Technol 2003;9:274–83. https://doi.org/10.1034/j.1600-0846.2003.00019.x.
[79] Khatyr F, Imberdis C, Vescovo P, Varchon D, Lagarde J-M. Model of the viscoelastic behaviour of skin in vivo and study of anisotropy. Ski Res Technol 2004;10:96–103. https://doi.org/10.1111/j.1600-0846.2004.00057.x.
[80] Jacquemoud C, Bruyere-Garnier K, Coret M. Methodology to determine failure characteristics of planar soft tissues using a dynamic tensile test. J Biomech 2007;40:468–75. https://doi.org/10.1016/j.jbiomech.2005.12.010.
[81] Jachowicz J, McMullen R, Prettypaul D. Indentometric analysis of in vivo skin and comparison with artificial skin models. Ski Res Technol 2007;13:299–309. https://doi.org/10.1111/j.1600-0846.2007.00229.x.
[82] Ventre M, Padovani M, Covington AD, Netti PA. Composition, structure and physical properties of foetal calf skin. Proc IULTCS-EUROCONGRESO, Istanbul. 2006. p. 1–21.
[83] Shadwick RE, Russell AP, Lauff RF. The structure and mechanical design of rhinoceros dermal armour. Philos Trans R Soc London Ser B Biol Sci 1992;337:419–28. https://doi.org/10.1098/rstb.1992.0118.
[84] Sodeman WA, Burch GE. A direct method for the estimation of skin distensibility with its application to the study of vascular states. J Clin Invest 1938;17:785–93. https://doi.org/10.1172/JCI101009.
[85] Evans JH, Siesennop WW. Controlled quasi-static testing of human skin in vivo. 7th Int Conf Med Biol Eng. 1967.
[86] Snyder RW, Lee LHN. Experimental study of biological tissue subjected to pure shear. J Biomech 1975;8:415–9. https://doi.org/10.1016/0021-9290(75)90077-9.
[87] Coutts L, Bamber J, Miller N. Multi-directional in vivo tensile skin stiffness measurement for the design of a reproducible tensile strain elastography protocol. Ski Res Technol 2013;19:37–44. https://doi.org/10.1111/j.1600-0846.2011.00604.x.
[88] Escoffier C, de Rigal J, Rochefort A, Vasselet R, Leveque J-L, Agache PG. Age-related mechanical properties of human skin: an in vivo study. J Invest Dermatol 1989;93:353–7. https://doi.org/10.1111/1523-1747.ep12280259.
[89] Sanders R. Torsional elasticity of human skin in vivo. Pflugers Arch Eur J Physiol 1973;342:255–60. https://doi.org/10.1007/BF00591373.
[90] Finlay B. The torsional characteristics of human skin in vivo. Biomed Eng (NY) 1971;6:567–73.
[91] Vlasblom DC. Skin elasticity. Netherlands: University of Utrecht; 1967.
[92] Neto P, Ferreira M, Bahia F, Costa P. Improvement of the methods for skin mechanical properties evaluation through correlation between different techniques and factor analysis. Ski Res Technol 2013;19. https://doi.org/10.1111/srt.12060.

[93] Grahame R, Holt PJ. The influence of ageing on the in vivo elasticity of human skin. Gerontologia 1969;15:121–39.
[94] Tregear RT. Physical functions of skin. London: Academic Press; 1966.
[95] Pedersen L, Hansen B, Jemec GBE. Mechanical properties of the skin: a comparison between two suction cup methods. Skin Res Technol 2003;9:111–5. https://doi.org/10.1034/j.1600-0846.2003.00021.x.
[96] Piérard GE, Piérard S, Delvenne P, Piérard-Franchimont C. In vivo evaluation of the skin tensile strength by the suction method: pilot study coping with hysteresis and creep extension. ISRN Dermatol 2013;2013:1–7. https://doi.org/10.1155/2013/841217.
[97] Dobrev H. In vivo study of skin mechanical properties in Raynaud's phenomenon. Ski Res Technol 2007;13:91–4. https://doi.org/10.1111/j.1600-0846.2007.00197.x.
[98] Schade H. Untersuchungen zur Organfunction des Bindegewebes. Zeitschrift Für Exp Pathol Und Ther 1912;11:369–99. https://doi.org/10.1007/BF02622207.
[99] Kirk E, Kvorning SA. Quantitative measurements of the elastic properties of the skin and subcutaneous tissue in young and old individuals. J Gerontol 1949;4:273–84. https://doi.org/10.1093/geronj/4.4.273.
[100] Kirk JE, Chieffi M. Variation with age in elasticity of skin and subcutaneous tissue in human individuals. J Gerontol 1962;17:373–80.
[101] Zheng Y, Crosby AJ, Cai S. Indentation of a stretched elastomer. J Mech Phys Solids 2017;107:145–59. https://doi.org/10.1016/j.jmps.2017.07.008.
[102] Zhang X, Greenleaf JF. Estimation of tissue's elasticity with surface wave speed. J Acoust Soc Am 2007;122:2522. https://doi.org/10.1121/1.2785045.
[103] Gerhardt L-C, Strassle V, Lenz A, Spencer N, Derler S. Influence of epidermal hydration on the friction of human skin against textiles. J R Soc Interface 2008;5:1317–28. https://doi.org/10.1098/rsif.2008.0034.
[104] Tosti A, Compagno G, Fazzini ML, Villardita S. A ballistometer for the study of the plasto-elastic properties of skin. J Invest Dermatol 1977;69:315–7. https://doi.org/10.1111/1523-1747.ep12507753.
[105] Fthenakis CG, Maes DH, Smith WP. In vivo assessment of skin elasticity using ballistometry. J Soc Cosmet Chem 1991;42:211–22.
[106] Jee T, Komvopoulos K. In vitro measurement of the mechanical properties of skin by nano/microindentation methods. J Biomech 2014;47:1186–92. https://doi.org/10.1016/j.jbiomech.2013.10.020.
[107] Ridge MD, Wright V. The directional effects of skin. J Invest Dermatol 1965;46:341–6. https://doi.org/10.1038/jid.1966.54.
[108] Sherman VR, Yang W, Meyers MA. The materials science of collagen. J Mech Behav Biomed Mater 2015;52:22–50. https://doi.org/10.1016/j.jmbbm.2015.05.023.
[109] Lanir Y, Fung YC. Two-dimensional mechanical properties of rabbit skin—I. Experimental system. J Biomech 1974;7:29–34. https://doi.org/10.1016/0021-9290(74)90067-0.
[110] Limbert G. A mesostructurally-based anisotropic continuum model for biological soft tissues-decoupled invariant formulation. J Mech Behav Biomed Mater 2011;4:1637–57. https://doi.org/10.1016/j.jmbbm.2011.07.016.
[111] Kuhl E, Garikipati K, Arruda EM, Grosh K. Remodeling of biological tissue: mechanically induced reorientation of a transversely isotropic chain network. J Mech Phys Solids 2005;53:1552–73. https://doi.org/10.1016/j.jmps.2005.03.002.
[112] Schneider DC, Davidson TM, Nahum AM. In vitro biaxial stress-strain response of human skin. Arch Otolaryngol - Head Neck Surg 1984;110:329–33. https://doi.org/10.1001/archotol.1984.00800310053012.
[113] Holzapfel GA, Ogden RW. On planar biaxial tests for anisotropic nonlinearly elastic solids. A continuum mechanical framework. Math Mech Solids 2009;14:474–89. https://doi.org/10.1177/1081286507084411.
[114] Holzapfel GA, Ogden RW, Sherifova S. On fibre dispersion modelling of soft biological tissues: a review. Proc R Soc A Math Phys Eng Sci 2019;475. https://doi.org/10.1098/rspa.2018.0736.
[115] Dick JC. The tension and resistance to stretching of human skin and other membranes, with results from a series of normal and oedematous cases. J Physiol 1951;112:102–13. https://doi.org/10.1113/jphysiol.1951.sp004512.
[116] Boudeau N, Malécot P. A simplified analytical model for post-processing experimental results from tube bulging test: theory, experimentations, simulations. Int J Mech Sci 2012;65:1–11. https://doi.org/10.1016/j.ijmecsci.2012.08.002.
[117] Li Y, Nemes JA, Derdouri AA. Membrane inflation of polymeric materials: experiments and finite element simulations. Polym Eng Sci 2001;41:1399–412. https://doi.org/10.1002/pen.10840.
[118] Bischoff JE, Drexler ES, Slifka AJ, McCowan CN. Quantifying nonlinear anisotropic elastic material properties of biological tissue by use of membrane inflation. Comput Meth Biomech Biomed Engin 2009;12:353–69. https://doi.org/10.1080/10255840802609420.
[119] Song WN, Mirza FA, Vlachopoulos J. Finite element analysis of inflation of an axisymmetric sheet of finite thickness. J Rheol 1991;35:93–111. https://doi.org/10.1122/1.550211.
[120] Liang Xing, Boppart SA. Biomechanical properties of in vivo human skin from dynamic optical coherence elastography. IEEE Trans Biomed Eng 2010;57:953–9. https://doi.org/10.1109/TBME.2009.2033464.
[121] Hendriks FM, Brokken D, Oomens CWJ, Baaijens FPT. Influence of hydration and experimental length scale on the mechanical response of human skin in vivo, using optical coherence tomography. Ski Res Technol 2004;10:231–41. https://doi.org/10.1111/j.1600-0846.2004.00077.x.
[122] Kearney SP, Khan A, Dai Z, Royston TJ. Dynamic viscoelastic models of human skin using optical elastography. Phys Med Biol 2015;60:6975–90. https://doi.org/10.1088/0031-9155/60/17/6975.
[123] Nesbitt S, Scott W, Macione J, Kotha S. Collagen fibrils in skin orient in the direction of applied uniaxial load in proportion to stress while exhibiting differential strains around hair follicles. Materials (Basel) 2015;8:1841–57. https://doi.org/10.3390/ma8041841.
[124] Fung YC. Elasticity of soft tissues in simple elongation. Am J Physiol 1967;213:1532–44. https://doi.org/10.1152/ajplegacy.1967.213.6.1532.
[125] Levi K, Weber RJ, Do JQ, Dauskardt RH. Drying stress and damage processes in human stratum corneum. Int J Cosmet Sci 2010;32:276–93. https://doi.org/10.1111/j.1468-2494.2009.00557.x.
[126] Papir YS, Hsu K-H, Wildnauer RH. The mechanical properties of stratum corneumI. The effect of water and ambient temperature on the tensile properties of newborn rat stratum corneum. Biochim Biophys Acta - Gen Subj 1975;399:170–80. https://doi.org/10.1016/0304-4165(75)90223-8.
[127] Christensen MS, Hargens CW, Nacht S, Gans EH. Viscoelastic properties of intact human skin: instrumentation, hydration effects, and the contribution of the stratum corneum. J Invest Dermatol 1977;69:282–6. https://doi.org/10.1111/1523-1747.ep12507500.
[128] Salter DC, McArthur HC, Crosse JE, Dickens AD. Skin mechanics measured in vivo using torsion: a new and accurate model more sensitive to age, sex and moisturizing treatment. Int J Cosmet Sci 1993;15:200–18. https://doi.org/10.1111/j.1467-2494.1993.tb00075.x.
[129] Auriol F, Vaillant L, Machet L, Diridollou S, Lorette G. Effects of short-time hydration on skin extensibility. Acta Derm Venereol 1993;73:344–7.
[130] Ottenio M, Tran D, Ní Annaidh A, Gilchrist MD, Bruyère K. Strain rate and anisotropy effects on the tensile failure characteristics of human skin. J Mech Behav Biomed Mater 2015;41:241–50. https://doi.org/10.1016/j.jmbbm.2014.10.006.
[131] Liu Z, Yeung K. The preconditioning and stress relaxation of skin tissue. J Biomed Pharm Eng 2008;1:22–8. https://doi.org/10.1007/s00238-011-0671-1.
[132] Muñoz MJ, Bea JA, Rodríguez JF, Ochoa I, Grasa J, Pérez del Palomar A, et al. An experimental study of the mouse skin behaviour: damage and inelastic aspects. J Biomech 2008;41:93–9. https://doi.org/10.1016/j.jbiomech.2007.07.013.
[133] Wahlsten A, Pensalfini M, Stracuzzi A, Restivo G, Hopf R, Mazza E. On the compressibility and poroelasticity of human and murine skin. Biomech Model Mechanobiol 2019;18:1079–93. https://doi.org/10.1007/s10237-019-01129-1.
[134] Lees C, Vincent JF, Hillerton JE. Poisson's ratio in skin. Biomed Mater Eng 1991;1:19–23.
[135] Veronda DR, Westmann RA. Mechanical characterization of skin-Finite deformations. J Biomech 1970;3. https://doi.org/10.1016/0021-9290(70)90055-2.
[136] Biniek K, Levi K, Dauskardt RH. Solar UV radiation reduces the barrier function of human skin. Proc Natl Acad Sci 2012;109:17111–6. https://doi.org/10.1073/pnas.1206851109.
[137] Martins PALS, Jorge RMN, Ferreira AJM. A comparative study of several material models for prediction of hyperelastic properties: application to silicone-rubber and soft tissues. Strain 2006;42:135–47. https://doi.org/10.1111/j.1475-1305.2006.00257.x.
[138] Ogden RW. Large deformation isotropic elasticity - on the correlation of theory and experiment for incompressible rubberlike solids. Proc R Soc A Math Phys Eng Sci 1972;326:565–84. https://doi.org/10.1098/rspa.1972.0026.

[139] Mooney M. A theory of large elastic deformation. J Appl Phys 1940;11:582–92. https://doi.org/10.1063/1.1712836.
[140] Ní Annaidh A, Bruyère K, Destrade M, Gilchrist MD, Maurini C, Otténio M, et al. Automated estimation of collagen fibre dispersion in the dermis and its contribution to the anisotropic behaviour of skin. Ann Biomed Eng 2012;40:1666–78. https://doi.org/10.1007/s10439-012-0542-3.
[141] Holzapfel GA, Gasser TC, Ogden RW. A new constitutive framework for arterial wall mechanics and a comparative study of material models. J Elast 2000;61:1–48. https://doi.org/10.1023/A:1010835316564.
[142] Holzapfel GA. Nonlinear solid mechanics: a continuum approach for engineering. John Wiley & Sons; 2000.
[143] Arruda EM, Boyce MC. A three-dimensional constitutive model for the large strech behavior for rubber elastic materials. J Mech Phys Solids 1993;41:389–412. https://doi.org/10.1016/j.commatsci.2011.10.026.
[144] Bischoff JE, Arruda EM, Grosh K. Finite element modeling of human skin using an isotropic, nonlinear elastic constitutive model. J Biomech 2000;33:645–52. https://doi.org/10.1016/S0021-9290(00)00018-X.
[145] Dunn MG, Silver FH. Viscoelastic behavior of human connective tissues: relative contribution of viscous and elastic components. Connect Tissue Res 1983;12:59–70. https://doi.org/10.3109/03008208309005612.
[146] Belkoff SM, Haut RC. A structural model used to evaluate the changing microstructure of maturing rat skin. J Biomech 1991;24:711–20. https://doi.org/10.1016/0021-9290(91)90335-K.
[147] Gunner CW, Hutton WC, Burlin TE. The mechanical properties of skin in vivo—a portable hand-held extensometer. Br J Dermatol 1979;100:161–3. https://doi.org/10.1111/j.1365-2133.1979.tb05555.x.
[148] Bischoff JE, Arruda EM, Grosh K. A rheological network model for the continuum anisotropic and viscoelastic behavior of soft tissue. Biomech Model Mechanobiol 2004;3:56–65. https://doi.org/10.1007/s10237-004-0049-4.
[149] Ma Q, Cheng H, Jang KI, Luan H, Hwang KC, Rogers JA, et al. A nonlinear mechanics model of bio-inspired hierarchical lattice materials consisting of horseshoe microstructures. J Mech Phys Solids 2016;90:179–202. https://doi.org/10.1016/j.jmps.2016.02.012.
[150] Weiss JA, Maker BN, Govindjee S. Finite element implementation of incompressible, transversely isotropic hyperelasticity. Comput Meth Appl Mech Eng 1996;135:107–28. https://doi.org/10.1016/0045-7825(96)01035-3.
[151] Szczesny SE, Elliott DM. Interfibrillar shear stress is the loading mechanism of collagen fibrils in tendon. Acta Biomater 2014;10:2582–90. https://doi.org/10.1016/j.actbio.2014.01.032.
[152] Gao Y, Waas AM, Faulkner JA, Kostrominova TY, Wineman AS. Micromechanical modeling of the epimysium of the skeletal muscles. J Biomech 2008;41:1–10. https://doi.org/10.1016/j.jbiomech.2007.08.008.
[153] Peng XQ, Guo ZY, Moran B. An anisotropic hyperelastic constitutive model with fiber-matrix shear interaction for the human annulus fibrosus. J Appl Mech 2006;73:815. https://doi.org/10.1115/1.2069987.
[154] Lu J, Zhang L. Physically motivated invariant formulation for transversely isotropic hyperelasticity. Int J Solids Struct 2005;42:6015–31. https://doi.org/10.1016/j.ijsolstr.2005.04.014.
[155] Fujita Y, Wagner DR, Biviji AA, Duncan NA, Lotz JC. Anisotropic shear behavior of the annulus fibrosus: effect of harvest site and tissue prestrain. Med Eng Phys 2000;22:349–57. https://doi.org/10.1016/S1350-4533(00)00053-9.
[156] Annaidh AN, Destrade M. Tension lines of the skin. Cham: Springer; 2019. p. 265–80. https://doi.org/10.1007/978-3-030-13279-8_9.
[157] Holzapfel GA, Niestrawska JA, Ogden RW, Reinisch AJ, Schriefl AJ. Modelling non-symmetric collagen fibre dispersion in arterial walls. J R Soc Interface 2015;12:20150188. https://doi.org/10.1098/rsif.2015.0188.
[158] Lanir Y. Constitutive equations for fibrous connective tissues. J Biomech 1983;16:1–12. https://doi.org/10.1016/0021-9290(83)90041-6.
[159] Lokshin O, Lanir Y. Viscoelasticity and preconditioning of rat skin under uniaxial stretch: microstructural constitutive characterization. J Biomech Eng 2009;131:31009. https://doi.org/10.1115/1.3049479.
[160] Jor JWY, Nash MP, Nielsen PMF, Hunter PJ. Estimating material parameters of a structurally based constitutive relation for skin mechanics. Biomech Model Mechanobiol 2011;10:767–78. https://doi.org/10.1007/s10237-010-0272-0.
[161] Meijer R, Douven LFA, Oomens CWJ. Characterisation of anisotropic and non-linear behaviour of human skin in vivo. Comput Meth Biomech Biomed Engin 1999;2:13–27. https://doi.org/10.1080/10255849908907975.
[162] Manschot JFM, Brakkee AJM. The measurement and modelling of the mechanical properties of human skin in vivo—I. The measurement. J Biomech 1986;19:511–5. https://doi.org/10.1016/0021-9290(86)90124-7.
[163] Tonge TK, Voo LM, Nguyen TD. Full-field bulge test for planar anisotropic tissues: Part II-A thin shell method for determining material parameters and comparison of two distributed fiber modeling approaches. Acta Biomater 2013;9:5926–42. https://doi.org/10.1016/j.actbio.2012.11.034.
[164] Freed AD, Einstein DR, Vesely I. Invariant formulation for dispersed transverse isotropy in aortic heart valves: an efficient means for modeling fiber splay. Biomech Model Mechanobiol 2005;4:100–17. https://doi.org/10.1007/s10237-005-0069-8.
[165] Driessen NJB, Bouten CVC, Baaijens FPT. A structural constitutive model for collagenous cardiovascular tissues incorporating the angular fiber distribution. J Biomech Eng 2005;127:494–503. https://doi.org/10.1115/1.1894373.
[166] Federico S, Gasser TC. Nonlinear elasticity of biological tissues with statistical fibre orientation. J R Soc Interface 2010;7:955–66. https://doi.org/10.1098/rsif.2009.0502.
[167] Sacks MS. Incorporation of experimentally-derived fiber orientation into a structural constitutive model for planar collagenous tissues. J Biomech Eng 2003;125:280–7. https://doi.org/10.1115/1.1544508.
[168] Melnik AV, Borja Da Rocha H, Goriely A. On the modeling of fiber dispersion in fiber-reinforced elastic materials. Int J Non Linear Mech 2015;75:92–106. https://doi.org/10.1016/j.ijnonlinmec.2014.10.006.
[169] Gasser TC, Ogden RW, Holzapfel GA. Hyperelastic modelling of arterial layers with distributed collagen fibre orientations. J R Soc Interface 2006;3:15–35. https://doi.org/10.1098/rsif.2005.0073.
[170] Buganza-Tepole A, Steinberg JP, Kuhl E, Gosain AK. Application of finite element modeling to optimize flap design with tissue expansion. Plast Reconstr Surg 2014;134:785–92. https://doi.org/10.1097/PRS.0000000000000553.
[171] Flynn C, Rubin MB, Nielsen P. A model for the anisotropic response of fibrous soft tissues using six discrete fibre bundles. Int J Numer Meth Biomed Eng 2011;27:1793–811. https://doi.org/10.1002/cnm.1440.
[172] Bischoff JE. Reduced parameter formulation for incorporating fiber level viscoelasticity into tissue level biomechanical models. Ann Biomed Eng 2006;34:1164–72. https://doi.org/10.1007/s10439-006-9124-6.
[173] Haut RC, Little RW. A constitutive equation for collagen fibers. J Biomech 1972;5:423–30. https://doi.org/10.1016/0021-9290(72)90001-2.
[174] Lanir Y. A structural theory for the homogeneous biaxial stress-strain relationships in flat collagenous tissues. J Biomech 1979;12:423–36. https://doi.org/10.1016/0021-9290(79)90027-7.
[175] Coleman BD, Noll W. Foundations of linear viscoelasticity. Rev Mod Phys 1961;33:239–49. https://doi.org/10.1103/RevModPhys. 33.239.
[176] Truesdell C, Noll W. The non-linear field theories of mechanics. Berlin, Heidelberg: Springer Berlin Heidelberg; 1992. https://doi.org/10.1007/978-3-662-13183-1.
[177] Limbert G, Middleton J. A transversely isotropic viscohyperelastic material application to the modeling of biological soft connective tissues. Int J Solids Struct 2004;41:4237–60. https://doi.org/10.1016/j.ijsolstr.2004.02.057.
[178] Puxkandl R, Zizak I, Paris O, Keckes J, Tesch W, Bernstorff S, et al. Viscoelastic properties of collagen: synchrotron radiation investigations and structural model. Philos Trans R Soc Lond B Biol Sci 2002;357:191–7. https://doi.org/10.1098/rstb.2001.1033.
[179] Bergström JS, Boyce MC. Constitutive modeling of the time-dependent and cyclic loading of elastomers and application to soft biological tissues. Mech Mater 2001;33:523–30. https://doi.org/10.1016/S0167-6636(01)00070-9.
[180] Roland CM. Network recovery from uniaxial extension: I. Elastic equilibrium. Rubber Chem Technol 1989;62:863–79. https://doi.org/10.5254/1.3536280.
[181] Fung YC. Biomechanics: mechanical properties of living tissues. New York, NY: Springer New York; 1993. https://doi.org/10.1007/978-1-4757-2257-4.
[182] Rubin MB, Bodner SR. A three-dimensional nonlinear model for dissipative response of soft tissue. Int J Solids Struct 2002;39:5081–99. https://doi.org/10.

1016/S0020-7683(02)00237-8.
[183] Mazza E, Papes O, Rubin MB, Bodner SR, Binur NS. Nonlinear elastic-viscoplastic constitutive equations for aging facial tissues. Biomech Model Mechanobiol 2005;4:178–89. https://doi.org/10.1007/s10237-005-0074-y.
[184] Rubin MB, Attia A. Calculation of hyperelastic response of finitely deformed elastic-viscoplastic materials. Int J Numer Meth Eng 1996;39:309–20. https://doi.org/10.1002/(SICI)1097-0207(19960130)39:2<309::AID-NME858>3.0.CO;2-B.
[185] Flynn C, Rubin MB. An anisotropic discrete fiber model with dissipation for soft biological tissues. Mech Mater 2014;68:217–27. https://doi.org/10.1016/j.mechmat.2013.07.009.
[186] Har-Shai Y, Bodner SR, Egozy-Golan D, Lindenbaum ES, Ben-Izhak O, Mitz V, et al. Mechanical properties and microstructure of the superficial musculoaponeurotic system. Plast Reconstr Surg 1996;98:59–70. https://doi.org/10.1097/00006534-199607000-00009.
[187] Barbarino GG, Jabareen M, Mazza E. Experimental and numerical study on the mechanical behavior of the superficial layers of the face. Ski Res Technol 2011;17:434–44. https://doi.org/10.1111/j.1600-0846.2011.00515.x.
[188] Hollenstein M, Jabareen M, Rubin MB. Modeling a smooth elastic-inelastic transition with a strongly objective numerical integrator needing no iteration. Comput Mech 2013;52:649–67. https://doi.org/10.1007/s00466-013-0838-7.
[189] Ciarletta P, Ben Amar M. A finite dissipative theory of temporary interfibrillar bridges in the extracellular matrix of ligaments and tendons. J R Soc Interface 2009;6:909–24. https://doi.org/10.1098/rsif.2008.0487.
[190] Drozdov AD. A model of cooperative relaxation in finite viscoelasticity of amorphous polymers. Int J Non Linear Mech 2000;35:897–909. https://doi.org/10.1016/S0020-7462(99)00066-9.
[191] Eyring H. Viscosity, plasticity, and diffusion as examples of absolute reaction rates. J Chem Phys 1936;4:283–91. https://doi.org/10.1063/1.1749836.
[192] Wagner MH, Schaeffer J. Constitutive equations from Gaussian slip-link network theories in polymer melt rheology. Rheol Acta 1992;31:22–31. https://doi.org/10.1007/BF00396464.
[193] Volokh KY. Modeling failure of soft anisotropic materials with application to arteries. J Mech Behav Biomed Mater 2011;4:1582–94. https://doi.org/10.1016/j.jmbbm.2011.01.002.
[194] Li W, Luo XY. An invariant-based damage model for human and animal skins. Ann Biomed Eng 2016;44:3109–22. https://doi.org/10.1007/s10439-016-1603-9.
[195] Cox HL. The elasticity and strength of paper and other fibrous materials. Br J Appl Phys 1952;3:72–9. https://doi.org/10.1088/0508-3443/3/3/302.
[196] Wu J, Yuan H, Li L, Fan K, Qian S, Li B. Viscoelastic shear lag model to predict the micromechanical behavior of tendon under dynamic tensile loading. J Theor Biol 2018;437:202–13. https://doi.org/10.1016/j.jtbi.2017.10.018.
[197] Jäger I, Fratzl P. Mineralized collagen fibrils: a mechanical model with a staggered arrangement of mineral particles. Biophys J 2000;79:1737–46. https://doi.org/10.1016/S0006-3495(00)76426-5.
[198] Pensalfini M, Duenwald-Kuehl S, Kondratko-Mittnacht J, Lakes R, Vanderby R. Evaluation of global load sharing and shear-lag models to describe mechanical behavior in partially lacerated tendons. J Biomech Eng 2014;136:91006. https://doi.org/10.1115/1.4027714.
[199] Buehler MJ. Atomistic and continuum modeling of mechanical properties of collagen: elasticity, fracture, and self-assembly. J Mater Res 2006;21:1947–61. https://doi.org/10.1557/jmr.2006.0236.
[200] Gautieri A, Russo A, Vesentini S, Redaelli A, Buehler MJ. Coarse-grained model of collagen molecules using an extended MARTINI force field. J Chem Theory Comput 2010;6:1210–8. https://doi.org/10.1021/ct100015v.
[201] Li W. Modelling methods for In Vitro biomechanical properties of the skin: a review. Biomed Eng Lett 2015;5:241–50. https://doi.org/10.1007/s13534-015-0201-3.
[202] Gibson T, Kenedi RM, Craik JE. The mobile micro-architecture of dermal collagen: a bio-engineering study. Br J Surg 1965;52:764–70. https://doi.org/10.1002/bjs.1800521017.
[203] Tregear RT. The mechanical properties of skin. J Soc Cosmet Chem 1969;20:467–77.
[204] Ribeiro JF, dos Anjos EHM, Mello MLS, de Campos Vidal B. Skin collagen fiber molecular order: a pattern of distributional fiber orientation as assessed by optical anisotropy and image analysis. PLoS ONE 2013;8:5–7. https://doi.org/10.1371/journal.pone.0054724.
[205] Ferdman AG, Yannas IV. Scattering of light from histologic sections: a new method for the analysis of connective tissue. J Invest Dermatol 1993;100:710–6. https://doi.org/10.1111/1523-1747.ep12472364.
[206] Diamant J, Keller A, Baer E, Litt M, Arridge RGC. Collagen; ultrastructure and its relation to mechanical properties as a function of ageing. Proc R Soc B Biol Sci 1972;180:293–315. https://doi.org/10.1098/rspb.1972.0019.
[207] Markenscoff X, Yannas IV. On the stress-strain relation for skin. J Biomech 1979;12:127–9. https://doi.org/10.1016/0021-9290(79)90151-9.
[208] Kastelic J, Palley I, Baer E. A structural mechanical model for tendon crimping. J Biomech 1980;13:887–93. https://doi.org/10.1016/0021-9290(80)90177-3.
[209] Comninou M, Yannas IV. Dependence of stress-strain nonlinearity of connective tissues on the geometry of collagen fibres. J Biomech 1976;9:427–33. https://doi.org/10.1016/0021-9290(76)90084-1.
[210] Lanir Y. Structure-strength relations in mammalian tendon. Biophys J 1978;24:541–54. https://doi.org/10.1016/S0006-3495(78)85400-9.
[211] Freed AD, Doehring TC. Elastic model for crimped collagen fibrils. J Biomech Eng 2005;127:587–93. https://doi.org/10.1115/1.1934145.
[212] Maceri F, Marino M, Vairo G. A unified multiscale mechanical model for soft collagenous tissues with regular fiber arrangement. J Biomech 2010;43:355–63. https://doi.org/10.1016/j.jbiomech.2009.07.040.
[213] Weinstein GD, Boucek RJ. Collagen and Elastin of Human Dermis**From the Divisions of Dermatology and Cardiology of the Department of Medicine, University of Miami School of Medicine and Howard Hughes Medical Institute, Miami, Florida. This investigation was supported in part by Gr. J Invest Dermatol 1960;35:227–9. https://doi.org/10.1038/jid.1960.109.
[214] Oxlund H, Manschot J, Viidik A. The role of elastin in the mechanical properties of skin. J Biomech 1988;21:213–8. https://doi.org/10.1016/0021-9290(88)90172-8.
[215] Nguyen DQA, Potokar TS, Price P. An objective long-term evaluation of Integra (a dermal skin substitute) and split thickness skin grafts, in acute burns and reconstructive surgery. Burns 2010;36:23–8. https://doi.org/10.1016/j.burns.2009.07.011.
[216] Chu C-S, McManus AT, Matylevich NP, Goodwin CW, Pruitt BA. Integra as a dermal replacement in a meshed composite skin graft in a rat model: a one-step operative procedure. J Trauma 2002;52:122–9. https://doi.org/10.1097/00005373-200201000-00021.
[217] Brusselaers N, Pirayesh A, Hoeksema H, Richters CD, Verbelen J, Beele H, et al. Skin replacement in burn wounds. J Trauma Inj Infect Crit Care 2010;68:490–501. https://doi.org/10.1097/TA.0b013e3181c9c074.
[218] Cadau S, Rival D, Andre-Frei V, Chavan MM, Fayol D, Salducci M, et al. New bioprinted skin, cosmetic in vitro model. J Cosmet Sci 2017;68:85–90.
[219] Retting KN, O'Neill CM, N'Guyen DLG, Presnell SC. Engineered three-dimensional skin tissues, arrays thereof, and methods of making the same; 2016.
[220] Sander EA, Lynch KA, Boyce ST. Development of the mechanical properties of engineered skin substitutes after grafting to full-thickness wounds. J Biomech Eng 2014;136:51008. https://doi.org/10.1115/1.4026290.
[221] Dias JR, Granja PL, Bártolo PJ. Advances in electrospun skin substitutes. Prog Mater Sci 2016;84:314–34. https://doi.org/10.1016/j.pmatsci.2016.09.006.
[222] Wang C, Li X, Hu H, Zhang L, Huang Z, Lin M, et al. Monitoring of the central blood pressure waveform via a conformal ultrasonic device. Nat Biomed Eng 2018;2:687–95. https://doi.org/10.1038/s41551-018-0287-x.
[223] Natali AN, Pavan PG, Carniel EL, Dorow C. Viscoelastic response of the periodontal ligament: an experimental-numerical analysis. Connect Tissue Res 2004;45:222–30. https://doi.org/10.1080/03008200490885742.

Andrei Pissarenko is a PhD Candidate in the department of Mechanical and Aerospace Engineering at the University of California, San Diego. He obtained his Bachelor's degree in Mechanical Engineering at the École Normale Supérieure de Cachan, France, in 2014, before completing a Master of Research in Bioengineering at the Imperial College of London, UK, in 2015. His research focuses on the characterization and modeling of biological and bioinspired materials, as well as potential biomedical applications.

Marc A. Meyers is a Distinguished Professor of Materials Science at the University of California, San Diego. His research is in the field of the mechanical behavior of materials. Within this field, he has focused on three areas: dynamic behavior of materials, nanocrystalline materials, and biological materials. In the dynamic behavior of materials, the unifying theme is the high rate at which events occur. He initiated this work in 1972 and has dedicated forty-five uninterrupted years to it, unifying it by emphasizing the fundamental physical and chemical phenomena. This has been defined in his now classic book, Dynamic Behavior of Materials (1994). He is the co-author of Mechanical Metallurgy, Mechanical Behavior of Materials, Biological Materials Science (2014), and approximately 450 papers. His honors include Fellow, TMS, APS, ASM, and Explorers Club as well as awards in the US (APS Duvall, ASM Albert White and Sauveur, TMS Mehl, Cohen and Educator, Acta Materialia Materials and Society, SMD/TMS Distinguished Engineer/Scientist and Service), in Europe (Humboldt, DGM Heyn, and DYMAT Rinehart), and in China (Lee Hsun). He was co-founder of the Center for Explosives Technology Research, New Mexico Tech, and of the EXPLOMET conference series (1980–2000), as well as Associate Director and Director of the UCSD Institute for Mechanics and Materials, where he co-organized four summer schools. He co-chaired the first three Pan American Materials Conferences, which he co-founded.